2007

Shear Responses of Poly(ethylene oxide)-Laponite Nanocomposite Hydrogels

Elena Loizou
Louisiana State University and Agricultural and Mechanical College, eloizo1@lsu.edu

SHEAR RESPONSES OF POLY(ETHYLENE OXIDE)-LAPONITE NANOCOMPOSITE HYDROGELS

A Dissertation

Submitted to the Graduate Faculty of the
Louisiana State University and
Agricultural and Mechanical College
in partial fulfillment of the
requirements for the degree of
Doctor of Philosophy

in

The Department of Chemistry

by
Elena Loizou
B.S., University of Cyprus, 2002
May 2007

This dissertation is dedicated to my loved ones,

who supported me through my academic endeavors

ACKNOWLEDGMENTS

First, I would like to express my gratitude to my advisor, Dr. Gudrun Schmidt for all the support, guidance, and encouragement throughout the last five years. A special thank to Dr. Paul Butler and Dr. Lionel Porcar from the NIST Center for Neutron Research for their tremendous constant encouragement, advice, and supervision especially over the last years. I consider myself lucky having all three of you as mentors that through our endless research discussions you made this work a wonderful learning experience.

I would also like to acknowledge the faculty members on my committee for taking time out of their busy schedule and accepting to be part of my committee. Thanks also to my research group for help and support with day-to-day research activities.

I am grateful to my friends at NIST, at LSU, and in Cyprus for their help, love, and support during this difficult time of my life. Vicky, Jing, Jason, Antonio, Evi, and Yianno thank you for everything; without having all of you by my side this dissertation may have never been possible.

Finally yet importantly, I would like to thank my family and particularly my parents for believing in me, and supporting my choices.

TABLE OF CONTENTS

LIST OF TABLES

LIST OF FIGURES

LIST OF ABBREVIATIONS

ESEM	Environmental Scanning Electron Microscopy
LRD	Laponite RD, synthetic silicate clay
NIST	National Institute of Standards and Technology
PEO	Poly(ethylene oxide)
SANS	Small Angle Neutron Scattering
SAXS	Small Angle X-Ray Scattering
SEM	Scanning Electron Microscopy
Shear-SANS	Small Angle Neutron Scattering under Shear
TEM	Transmission Electron Microscopy
USANS	Ultra-Small Angle Neutron Scattering

ABSTRACT

This research seeks to understand the structure and shear responses of poly(ethylene oxide)-Laponite nanocomposite hydrogels and to relate the macroscopic physical properties to the nanoscopic structural changes. Understanding that relationship is necessary, in order to tailor material properties to specific applications. Information on the structure at rest on multiple length scales was obtained by combining microscopic and neutron scattering techniques. The structural changes that occur in response to a shear field were explored using rheology and neutron scattering. These structures were examined as a function of polymer molecular weight, polymer and clay concentrations, and sample preparation method. While the sample preparation method had no significant effect on these gels, the other two parameters were found to strongly influence the shear behavior of the systems. It was found that the dynamical behavior of these gels is controlled by the ability of a polymer chain to bridge clay platelets, which is influenced both by the length of the polymer and the clay and polymer concentrations.

CHAPTER 1 INTRODUCTION AND LITERATURE REVIEW

1.1 Polymer-Nanoparticle Composites

In the last 20 years, there has been a strong emphasis on the development of nano size composite materials consisting of an organic polymer and an inorganic compound. The increased interest on such materials can be attributed to the plethora of applications these materials can find in areas such as electronics, data storage, communications, aerospace, sporting materials, health and medicine, environmental, transportation, and national defense.[1] Nanocomposite materials have attracted the interest of a number of researchers because they combine the ease of processability of a polymer with the improved mechanical,[2] electrical,[3, 4] optical,[3, 5] and thermal[2, 6] properties of an inorganic particle. Typical nanoparticles that are currently used for composites are nanotubes, nanofibers, nanorods, nanowires, nanospheres, fullerenes, clays, etc. They are generally classified by their geometries into three main categories: fibrous, spherical, and layered materials.[1]

Studies on fibrous materials have shown that their incorporation into conventional polymers can increase the electrical and thermal conductivity[7-9] and/or toughen[10-12] the polymers. Besides the extensive interest on bulk fibrous nanocomposites, there is also interest into fibers and films,[9, 13, 14] since in these forms they can easily be integrated into devices and microsystems.[15] For example, fibers of carbon nanotubes have been developed for different aerospace applications such as aircraft engine anti-icing and lightning strike protection materials, as well as fire retardant coatings.[1] Films containing

metal (i.e. silver, gold) nanorods have also been synthesized, with optical polarization properties that can find applications as filters, signal modulators and optical devices.[5] In the field of polymer-fibrous nanocomposites, two of the main challenges to date are the dispersion and alignment of the fibrous nanoparticles inside the polymer matrix. Achieving considerable dispersion and/or orientation will allow optimal property improvements, such as easier transfer of energy (electrical and/or thermal). Researchers have used a number of different techniques to disperse fibrous materials in polymer matrices, including chemical functionalization to tailor the interaction with polymers,[16, 17] ultrasonic dispersion in solution,[18] melt processing,[19] addition of surfactants,[20] and many more. Other researchers have achieved nanoparticle alignment by applying a magnetic field[21] or shear flow[22] to a nanocomposite sample.

Spherical nanoparticles can also drastically improve the properties of the polymer matrices. For example, aluminum (Al) nanoparticles are often added to increase the conductivity, whereas silicon carbide (SiC) nanoparticles are added to enhance the corrosion resistance and strength of a polymer.[1] Interest in silica spheres has also remarkably grown, due to the availability of well structured, relatively monodisperse, and cost effective nanoparticles. A study on a nylon-6 filled with silica nanoparticles has shown increased strength and moduli of the material.[23] Another study has shown that the incorporation of Al_2O_3 improved the toughness of brittle polyester resin systems.[24] The dispersion and aggregation of polymer-spherical nanoparticles have captured the interest of many researchers. For example, Ohno *et al*.[25] used a well defined polymer to coat gold nanospheres, so as to achieve optimal dispersion of the nanoparticles without the

formation of aggregates. Other researchers have used a coupling agent in a SiC/vinylester nanocomposite system to improve the dispersion quantity and strength.[26]

When the filler particle has a plate-like structure, it is classified as a layered nanomaterial. Layered composites can be divided into two main types, *intercalated*, and *delaminated* or *exfoliated* structures.[1] Intercalated structures have a single extended polymer chain intercalated between the layers, resulting in a well ordered multilayer with alternating polymer-inorganic layers. The delaminated structure has layers that are well dispersed and exfoliated in a continuous polymer matrix.[1] The most studied layered nanocomposites are those where the inorganic particles are either graphite sheets,[27, 28] or clay minerals[29] also referred to as phyllosilicates. Studies performed on graphite reinforcement nanocomposites not only have shown improved thermal and electrical properties, but also an increase of the mechanical strength and stiffness.[1, 27, 28] On the other hand, studies performed using clays have shown that when dispersed in a polymer matrix, they can greatly improve the dimensional stability and the barrier properties of the polymer.[30-32] The incorporation of a nano-clay into a biodegradable polymer (such as polylactide) has shown improved biodegradability of the material, as a result of the catalytic role of the organoclay in the biodegradation mechanism.[33] In addition, a study performed on clay nanocomposite films made of polyimide has shown a reduction in the transmission of gas and moisture through the film.[34]

1.2 Polymer-Clay Nanocomposites

Among all polymer-nanoparticle composites, polymer-clay nanocomposites have gathered increased attention lately due to their advanced physical properties. They exhibit high moduli, increased strength and heat resistance, decreased solvent and gas

permeability, decreased flammability and increased biocompatibility and biodegradability.[30, 31] Many of the improved mechanical properties have applications in the automotive and machine industries, for example as covers for mobile phones and pagers, door handles, impellers, tool housings, and stronger engine covers.[35] Recently, Toyota's research group has developed a nylon-layered silicate nanocomposite to be used as an automotive timing-belt cover. The nanocomposite contained as little as 2 vol % of clay, which was enough to double the tensile modulus and strength of the material, without much loss in impact resistance.[36, 37] Also, since clay nanocomposites exhibit increased heat resistance and reduced flammability compared to pure polymers, they can be used in high-temperature applications, such as in fire retardant coatings.[30, 31, 38, 39] Boeing has demonstrated the potential use of clay nanocomposites in aerospace applications.[1] Recently, researchers at NASA have developed transparent nanocomposites with chemically modified clay which have shown an increase in toughness and also resistance to micro cracking and heat.[1] Additionally, these colloidal systems may find use in applications such as paints, coatings,[25] cosmetics, pharmaceutical formulations, optical switches, thin films, barrier membranes,[40] and even ceramic precursor materials.

The improved properties of these nanocomposite materials are derived from: (1) the physical presence of the clay nanoparticle, (2) the interaction of the polymer with the clay nanoparticle, (3) the state of dispersion of the clay nanoparticle, and (4) the particle orientation within the polymer matrix. In order to design new materials with desired properties suitable for a specific application, it is essential to have a detailed understanding of these four issues. So far, several studies have employed microscopy and

rheology, in addition to light, x-ray, and neutron scattering to examine both the structure and polymer-clay interactions on all length scales.[41-52] However, an additional and crucial issue that needs to be explored is the influence of shear on these polymer-clay nanocomposite systems. During processing for a specific application, these polymer-clay nanocomposites may experience significant shear-flow that may cause structural changes both in the nano and micro meter length scale. An example of structural change in the nanometer length scale is the orientation of the clay nanoparticle within the polymer matrix. These structural changes might in turn change the physical properties of the system. Thus, it is imperative not only to understand the polymer-clay interactions, but also the structural changes that occur on various length scales in response to shear.

1.3 Flow Effects in Polymer-Clay Nanocomposites

Under the influence of flow (or stretch) anisotropic species like clay platelets can orient along three directions, often referred to in the literature, as 'a', 'b', and 'c' orientations. Figure 1.1 shows the three types of orientations: in the 'a'-orientation, the platelets align with their face normal parallel to the neutral direction (the direction that is perpendicular to the flow and gradient), in the 'b'-orientation the platelets align with their face normal parallel to the flow direction, and in the 'c'-orientation the platelets align with their face normal parallel to the gradient direction.[53] (Normal is called the vector which is perpendicular to the surface). The type of orientation the clay platelets achieve in a system depends on a variety of parameters, such as the clay type, the size and concentration of the particles, the interaction between the polymer and the clay, and many more. In what follows, a few examples of each of the three types of orientation are presented.

Generally when clay platelets are exposed to shear they align in the direction of flow ('c'-orientation). This has been nicely described by Krishnamoorti *et al*.[54, 55] and Kojima *et al*.,[56] who performed experiments on nylon-6-clay hybrids and on poly(ε-caprolactone)-Montmorillonite nanocomposites. In both cases, the authors have observed substantial alignment in the 'c'-orientation when the nanocomposites were subjected to prolonged large amplitude oscillatory shear. Measurements performed by Lele *et al*.[57] using *in situ* rheo-x-ray diffraction also have shown a flow induced 'c'-orientation of polypropylene-Montmorillonite nanocomposites melts.

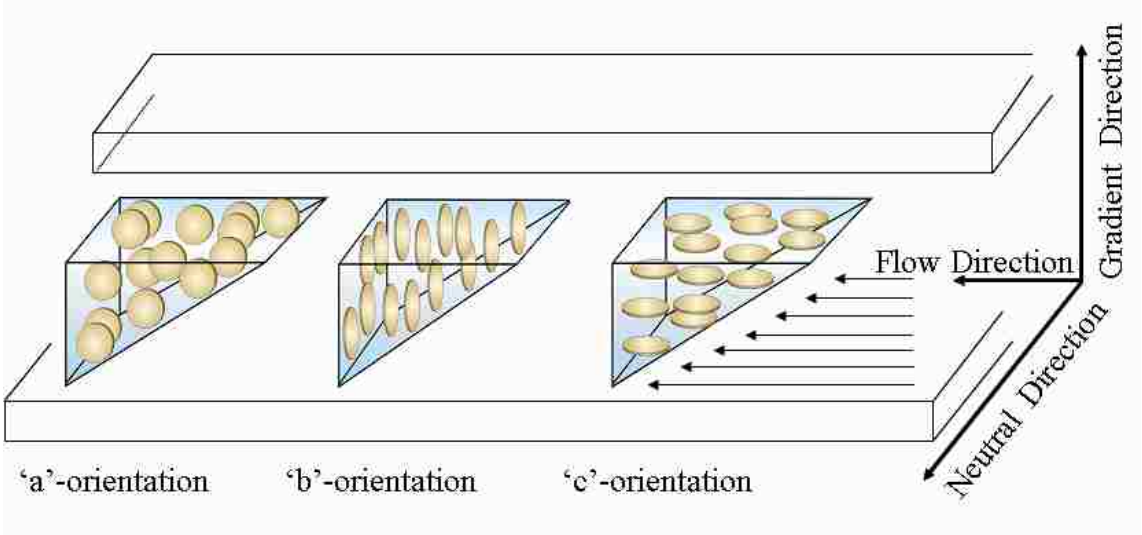

Figure 1.1: Schematic representation of the three types of orientation that clay platelets can attain under shear flow

In addition, the 'c'-orientation has also been observed in polystyrene-clay nanocomposites, where under shear flow an ordered structure developed that was attributed to the orientation of the silicate layers as well as the phenyl groups of polystyrene.[58] The influence of shear on viscoelastic solutions of poly(ethylene oxide) and Montmorillonite was investigated by Malwitz *et al*.,[59] who observed alignment of the Montmorillonite platelets in the 'c'-orientation. Cessation of shear led to partial and very

slow randomization of the Montmorillonite platelets within the polymer clay network. Studies performed on films composed of poly(ethylene oxide)-Laponite[60, 61] and poly(ethylene oxide)-Montmorillonite[61-63] also revealed the favored 'c'-orientation with the platelets aligned in the spread direction of the film. Studies performed on pure clay solutions have shown a preferential alignment of particles in the direction of flow ('c'-orientation) for Montmorillonite dispersions, but no nanoscopic orientation has been observed for Laponite dispersions (up to 6 wt %) under shear.[64]

Recent transmission electron microscopy (TEM) images obtained by Okamoto *et al*.[65] on polypropylene-Montmorillonite intercalated nanocomposite melts have revealed a strong strain-induced hardening and rheopexy features that arise from the perpendicular alignment of the silicate layers in the stretching direction ('b'-orientation). The 'b'-orientation has also been observed on nanocomposite gels made of poly(*N*-isopropylacrylamide) and Laponite clay.[66, 67] A dispersion of inorganic platelets of nickel hydroxide with polyacrylate was studied under shear by Brown *et al*.,[68] who observed that at low shear rates (below 1 s^{-1}) the platelets aligned with their normal in the flow direction ('b'-orientation), while at high shear rates (above 18 s^{-1}) the platelets were aligned with their normal in the gradient direction ('c'-orientation). At intermediate shear rates, a texture of co-existing domains of both 'b' and 'c' orientations was observed.

An 'a'-orientation has been observed by Medellin-Rodriguez *et al*.[69] on end-tethered nylon-6 nanocomposites in response to steady shear in the melt state using small angle x-ray scattering (SAXS) and TEM measurements. In their studies, the clay platelets were oriented at relatively low shear rates at temperatures slightly higher than the melting point. More recent studies by Schmidt *et al*.[43, 44] on poly(ethylene oxide)-Laponite

nanocomposites reveal that the clay platelets align in the 'a'-orientation. Flow-birefringence together with shear-SANS measurements (in deuterated and clay contrast matched solvents) suggested that with increasing shear rate the clay particles orient first, followed by the stretching of interconnected polymer chains. Studies by Lin-Gibson *et al.*[70, 71] tried to explain the orientation in these systems by suggesting that the platelets orient in response to the biaxial stress arising from the shear and the elastic forces.

From the examples presented here, it is clear that in order to obtain control of the nanoscopic structure it is essential to study and understand the parameters that affect the structural changes.

1.4 Model System: Poly(ethylene oxide)-Laponite

The model system most commonly used to study polymer-clay interactions and structural changes under shear flow are aqueous dispersions of Laponite clay nanoparticles dispersed in a poly(ethylene oxide) matrix. The macroscopic and nanoscopic behavior of these colloidal dispersions can be tuned by changing parameters like composition, pH and ionic strength. Variation of such parameters leads to colloidal systems with dramatically different and unique properties. For example, by just varying the polymer and clay compositions one may generate solutions, shake gels, or permanent gum-like gels.[43-45, 72-74] The research presented in this dissertation deals with aqueous dispersions of poly(ethylene oxide)-Laponite nanocomposites above the sol-gel transition where they form permanent gels. These hydrogels seem promising materials for biomedical applications such as drug delivery carriers and tissue growth scaffolds, due to

their low cost, low toxicity, high biocompatibility, high water content, and soft consistency.

1.5 Laponite Clay

Laponite is a synthetic clay with a well defined structure and chemical composition.[75] Laponite belongs to the family of phyllosilicates, meaning that it contains parallel layers (sheets) of silicate atoms. The unit cell of an ideal crystal is shown in Figure 1.2 where the octahedral layer of six magnesium atoms is sandwiched between the two tetrahedral layers each one composed of four silicon atoms. These groups are balanced by twenty oxygen atoms and four hydroxyl groups, so that the ideal structure has an overall neutral charge. In reality however, either some magnesium atoms are substituted by lithium atoms (isomorphous substitution) or some magnesium sites are empty, giving the empirical formula $[Na^{+}_{0.7}(Mg_{5.5}Li_{0.3})Si_8O_{20}(OH)_4]^{-0.7}$. [75] This empirical formula has a negative charge of 0.7 per unit cell. The height of the unit cell represents the thickness of the Laponite crystal. Repeating the unit cell 30, 000 to 40, 000 times in the other two directions results in a disc shaped particle like that shown in Figure 1.3.

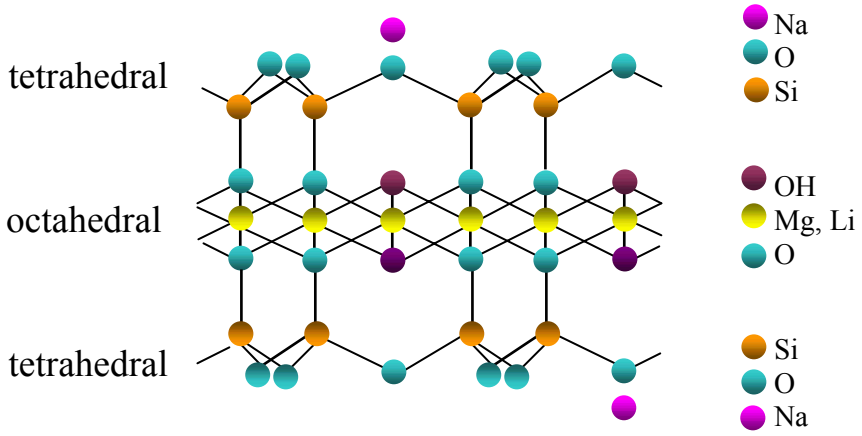

Figure 1.2: The ideal structure of Laponite

Small angle neutron[46, 76] and x-ray scattering[77, 78] studies performed on dilute suspensions of Laponite showed that the disc shaped particles have diameter between 25 nm and 30 nm and a thickness of ≈ 1 nm. However, depending on the origin of these particles, other studies have shown that the particles can be slightly polydisperse in size.[79, 80] The large aspect ratio (ratio of the diameter to the thickness) of clay platelets may lead to supramolecular organizations reminiscent of other mesoscopic systems, such as liquid crystalline polymers, surfactants, or block copolymers.[70, 81]

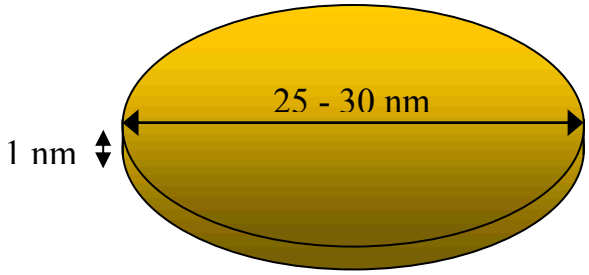

Figure 1.3: Schematic representation of a Laponite disc shaped particle that has a diameter between 25 and 30 nm and a thickness of ≈ 1 nm

In the dry powder state, the clay platelets are arranged into stacks which are held together electrostatically by sharing sodium ions in the interlayer region.[75] When dispersed in water, the sodium ions are hydrated and released into solution, creating an electrical double layer that causes the particles to repel each other and exfoliate.[75] A single dispersed disk particle has a negative charge on the face produced by isomorphous substitution, whereas the charge on the particle edge is pH-dependent, with negative edge charges favored at high pH (pH ≈ 10) and positive edge charges favored at lower pH (pH ≈ 7).[82, 83] The small localized charges at the edges are generated by ionization or protonation of the hydroxyl groups at the end of the crystal structure. Thompson *et al*.[83]

have proposed that at pH values lower than 7, Laponite platelets dissolves and releases silicate, Na^+, Li^+, Mg^{2+}, according to the following equation:

$$[Na^+_{0.7}(Mg_{5.5}Li_{0.3})Si_8O_{20}(OH)_4]^{-0.7} + 12H^+ + 8H_2O \rightarrow 0.7\ Na^+ + 8Si(OH)_4 + 5.5Mg^{2+} + 0.3Li^+$$

1.6 Interactions between Laponite Particles

With increasing particle concentration, aqueous Laponite suspensions have been observed to undergo a transition from a liquid to a gel and then to a birefringent gel.[84-86] Phase diagrams of Laponite suspensions showing the sol-gel behavior, as well as the transition to the birefringent phase have been constructed as a function of clay concentration and ionic strength.[84-86] The existence of birefringent gels has been attributed to the formation of a nematic phase,[87] where the clay particles have long-range orientational order but only short-range positional order. This means that the anisotropic particles are on average oriented in the same direction, but their centers of mass are not located on a lattice (Figure 1.4).[81]

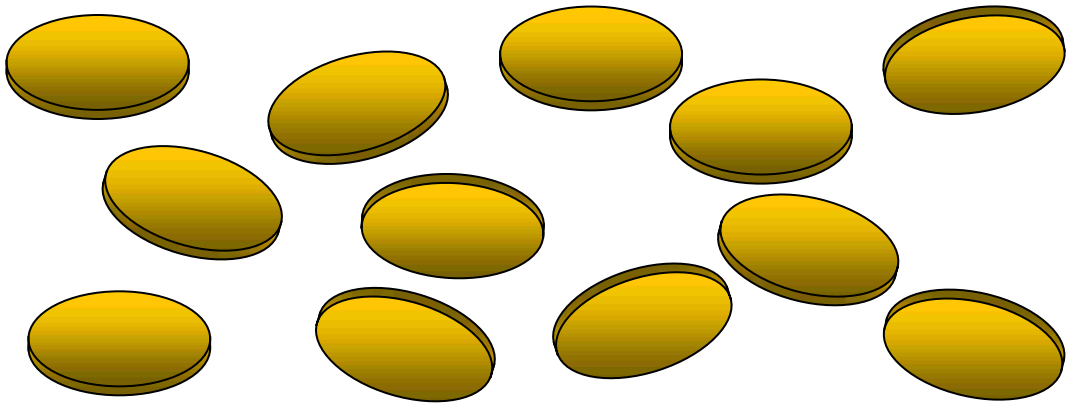

Figure 1.4: A nematic phase of particles has long range orientational order, but short range positional order

Lemaire *et al*.[87] performed SAXS experiments on birefringent Laponite samples and obtained SAXS patterns that were anisotropic. In contrast, small angle neutron scattering (SANS) measurements from Lal *et al*.[42] also on birefringent samples gave isotropic scattering patterns, suggesting that the nematic domains formed are powder averaged. Lal *et al*.[42] however, used a different grade of Laponite from the one used by Lemaire *et al*.[87] and also prepared their samples with a different procedure.

So far, experiments on these systems have given conflicting results and the structure of Laponite in solution and/or gel remains a point of debate. Static and dynamic light scattering studies performed by Nicolai *et al*.[88] on Laponite dispersions suggest that at the final stage of dispersion the system contains particles with a broad size distribution. This can be interpreted either as a size distribution of individual platelets, or as an incomplete dispersion of the clay containing monodisperse particles and some stacks. These results are in contrast to those of Rosta *et al*.,[89] who suggest the existence of tactoids, which are droplets of a nematic phase containing between two and four Laponite platelets with an average diameter of 30 ± 10 nm. Light scattering experiments by Kroon *et al*.[80, 90, 91] on Laponite solutions of 3 wt % yield a fractal-like structure with a fractal dimension that evolved from 2.8 to 2.1 during the gelation process. Investigations by Pignon *et al*.[92, 93] also suggest the existence of a fractal-like structure that was correlated with two characteristic length scales. The first length scale of the order of few μm was linked to a fractal dimension of 3, and the second one for sizes bigger than 10 μm was linked to a fractal dimension that increases from 1 to 1.8 with the particle volume fraction. These fractal dimensions have been questioned by Bonn *et al*.,[94] who show that there is no apparent fractal dimension after filtering the samples. They suggested that

filtering removes or breaks up large aggregates and that the solution structure can be described as a repulsive glass, where long-range electrostatic repulsions dominate.[94] More recently, experimental results from Bhatia *et al*.[95] prove that even after filtering the samples, the large-scale structure in Laponite gels exists, above the isotropic nematic transition. According to the authors, this transition occurs at concentrations around 3 wt % Laponite for solutions of 10^{-4} M ionic strength.[95]

The mechanism of gel formation is still under considerable debate, with two prevailing hypotheses. The first hypothesis is that the electrostatic repulsion arising from the overlapping double layers dominates particle interactions and is responsible for the gelation process.[78, 80, 84, 94, 96, 97] The second one is that attractive interactions driven either by Van der Waals forces or by electrostatic interactions between the edges and the faces of the particles are responsible for gel formation.[65, 93, 98] This view implies the formation of T-shaped units, yielding the so called "house of cards" structure that was first proposed by van Olphen.[99] Later on, Saunders *et al*.[100] suggested that both mechanisms may be valid, depending on the clay concentration, the ionic strength, and the pH of the solution. In particular, they suggested that at high pH (pH ≈ 10) and low ionic strength (I ≈ 0.005 M) electrostatic repulsion dominates the particle behavior, and face-face interaction is favored. The face-edge aggregation arises at lower pH (pH ≈ 7.5) and higher ionic strength (I ≈ 0.01 M).[100]

More recently, a phase diagram for Laponite particles at pH = 10 was published, which suggests that as the ionic strength increases, there is first a transition from a repulsive glass to an attractive glass (at I ≈ 0.0001 M), and then a second transition to an attractive gel (at I > 0.001 M).[101] The repulsive glass is stabilized by long-range Coulomb

repulsions, whereas the attractive gel is formed by van der Waals attractions. The difference between the glassy state and the gel state is that the glassy state is obtained at high volume fractions of particles where there is no network present. The gel state may be obtained for low-volume fractions and in most cases is characterized by the existence of a fractal network.[94] The kinetic phenomenon of the liquid-glass transition is called "aging", while that of the sol-gel transition is called "gelation". During aging the dynamics in Laponite dispersions slow down, the particles cannot escape from the "cages" formed by neighboring particles and the system becomes strongly nonergodic. On the other hand, during gelation the particles form clusters whose size increase with time. Finally, these clusters form a percolated network and the system becomes also nonergodic. Both processes can be characterized as an ergodic-to-nonergodic transition by the resulting appearance of elasticity.[94, 97, 101-106]

1.7 Poly(ethylene oxide) in Solution

Poly(ethylene oxide) (PEO) is one of the most researched synthetic polymers, due to its chemical simplicity and interesting solubility properties.[107-115] The presence of the oxygen atom in the repeating unit -(CH_2CH_2O)-, completely changes the nature of interactions between the individual molecules and makes it soluble in both organic and aqueous solvents.[107, 108]

When dissolved in water, PEO is characterized by hydrophilic interactions between the water molecules and the oxygen atoms of the polymer, as well as by hydrophobic interactions between the water and the CH_2CH_2 group. PEO can be dissolved in water because water molecules form a sheath around the PEO molecules, similar to the hydration layer around proteins.[108] The hydration layers around the PEO

chains have been studied[116, 117] and models have been presented that show cage-like structures, where the CH_2CH_2 groups are shielded from contacting water molecules similarly to hydrated structures.[108] The main reason PEO dissolves in water for a wide range of temperatures and concentrations is that the oxygen-oxygen interdistance (2.88 Å) on the PEO chain matches the oxygen-oxygen distance (2.85 Å) in the structure of pure water.[108] The homologues PMO [-(CH_2O)-] and PPO [-($CH(CH_3)CH_2O$)] are not soluble in water.[108]

The solubility of PEO in water decreases with increasing temperature, and phase separation occurs above a lower critical solution temperature (LCST) that depends on the polymer molecular weight. Upon continued heating, miscibility will occur again, due to the existence of an upper critical solution temperature (UCST). Thus, formation of closed loop regions of phase coexistence is one of the characteristic features of the behavior of aqueous PEO solutions.[110] Phase diagrams of PEO aqueous solutions have been constructed by several authors and theoretical models have been used to describe the PEO phase behavior.[110, 118-126]

The conformation of PEO chains in water has been investigated as well. Several studies have observed the formation of clusters when PEO dissolves in water.[107-109, 127-129] The origin of these clusters has been the subject of intense debates. The formation of the clusters has been attributed to the existence of impurities in the water, the crystallization of the PEO groups, the low temperature phase transition that produces a polymer rich phase, the hydrogen bonding between the chains, and the chain end effects. There has also been a hypothesis that PEO, which is known to form a helix in the solid crystalline state, retains some of its helicity even in dilute aqueous solution.[116]

1.8 Mechanism of Adsorption of PEO on Laponite Particles

Poly(ethylene oxide) has been successfully used as a dispersant for colloidal particles (i.e. latex)[130] and as a flocculant for some oxide particles (i.e. silica)[131, 132] due to its ability to adsorb onto the particle surfaces. The adsorption of PEO on oxide surfaces has been studied by many groups and a number of adsorption mechanisms have been proposed. From these mechanisms, one that seems most plausible to describe the adsorption of PEO on Laponite particles, is based on hydrogen bonding and comes from studies performed by Mathur *et al*.[131] and Bjelopavlic *et al*.[132] on oxide surfaces. This hydrogen bonding interaction is best described as a Bronsted acid – Lewis base interaction. The ether groups of the PEO segments can be considered Lewis bases, since they have two available electrons to be donated. In addition, groups on the oxide surfaces that have proton donor capabilities can be considered as Bronsted acids. On silica surfaces (SiO_2), the proton donor groups were found to be the isolated silanols. Based on this, the silicon oxide groups present in the tetrahedral layer are possible binding sites for PEO segments onto Laponite particles. Even though there are no isolated silanols in the perfect Laponite crystal, these can be formed due to defects (broken bonds) in the structure. It is most likely that PEO segments hydrogen bond only with the silicon oxide groups and not with the magnesium or lithium oxide groups present in the octahedral layer, since studies indicate that PEO does not adsorb to oxides that are less acidic than SiO_2.

The second idea is that adsorption occurs as a result of electrostatic interactions between PEO and Laponite. This is based on the results of theoretical calculations for the binding of water molecules to Laponite particles.[133] It was suggested that an attractive

interaction between a water oxygen lone pair and the positive zone created from the silica atoms on the Laponite surface, and/or an attractive interaction between the water hydrogen atoms and the oxygen atoms on the Laponite surface, lead to the adsorption of water molecules onto the charged Laponite surfaces. Even though a polymer will inherently adsorb in a different way to a small molecule, one can assume that PEO could interact with Laponite in a similar way. Therefore, there must be attractive interactions between the ether oxygen atoms of the PEO and the silica atoms of the Laponite and/or the hydrogen atoms of the PEO and the oxygen atoms of the Laponite.

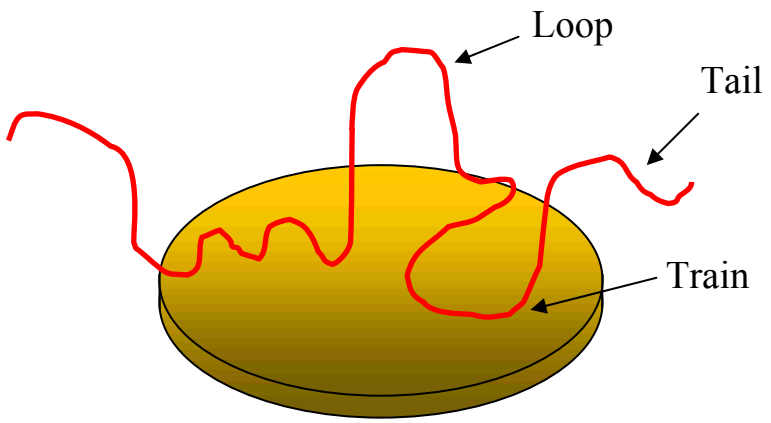

Figure 1.5: A schematic representation of polymer adsorption at an interface

Despite the mechanism by which adsorption occurs, when polymers adsorb onto solid surfaces they may adopt three possible conformations: trains, loops and tails (Figure 1.5).[134] Trains are composed of a series of neighboring segments that are physically in contact with the surface. Loops are composed of a series of neighboring segments that extend out into the solution and are not in contact with the surface, and link two sets of trains together. Tails are formed by the ends of the polymer chains extending into the bulk solution. Studies by Nelson *et al.*[46-48] suggest that when the PEO adsorbs onto

Laponite particles, it forms a compact layer of mostly trains and loops on the Laponite face, and long polymer chains are able to "wrap" around the particle extending from the top face to the bottom face, forming a loop around the edge of the particle.[46]

1.9 Laponite-PEO Systems

As mentioned above, PEO absorbs onto clay platelets. Low molecular weight polymers may inhibit aggregation of clay particles by classic steric hindrance and enable the formation of a stable fluid solution. Higher molecular weight polymers, especially at concentrations below the threshold for complete saturation of clay surface, produce "shake gels".[73, 74, 135] These gels are fluid but undergo a dramatic shear thickening behavior when subjected to vigorous shaking, in which state they can support their own weight upon inverting the vials. As a result, they are described as having the consistency of a "half-cooled gelatin dessert".[73] The shear-induced gelation is time reversible and strongly dependent on the PEO concentration and on temperature.[74] The shear deforms the large polymer-clay flocs and exposes fresh surface area for the formation of new polymer bridges, which rapidly form a network that spans the entire solution and generates a gel. When the shaking stops, thermal fluctuations are sufficient to desorb the polymer and the gel relaxes back to a fluid.[73] For these polymer clay gels no SANS anisotropy is observed in shear experiments, most probably because the applied shear is not high enough to overcome fast randomizing effects caused by the polymer and particle relaxation.

The adsorption of PEO polymer chains onto Laponite clay platelets at low polymer and clay concentrations was studied by Lal *et al*.[41, 42] using SANS. They observed that the gelation of the solution was either retarded or prevented depending on

the clay concentration, the polymer presence in the solution, and the molecular weight of the polymer. By varying the H_2O/D_2O ratio of the solvent, they managed to separate the contributions from bulk and adsorbed polymer chains. Thus, they calculated the adsorbed polymer layer thickness to be about 1.5 nm on each face, independent of the polymer's molecular weight. The authors assumed that the SANS intensity arises from the dense part of adsorbed polymer while scattering intensity coming from polymer loops and tails was neglected. Their results are not sensitive to the shape of the polymer concentration profile. More recent SANS studies performed by Nelson *et al*.[46] on the same polymer-clay system with sufficient PEO concentration for complete saturation of the clay surface showed that the polymer adsorbs flatly and coats the clay particles. A larger shell was observed on the platelet sides (2.5nm – 5 nm thick) compared to the shell parallel to the face (1.5 nm thick).[46] The authors suggested that the increased edge thickness is a result of the capability of polymer chains to wrap around the Laponite particles and form loops around the edges of the particles.[46]

At high polymer and clay concentrations, Schmidt *et al*.[43-45] reported strong gels with gum-like consistency. They suggested a dynamic adsorption-desorption equilibrium of the polymer chains onto the clay platelets, where the entangled polymer chains form a network with the clay particles as crosslinks. With increasing shear rate, these gels show a shear thinning behavior, a pronounced minimum in birefringence measurements, and an increasingly strong anisotropic scattering pattern. Taking into account their shear-SANS (in deuterated and contrast matched solvents), flow-birefringence, and rheological results, they propose that the shear flow induces orientation of the polymer and the platelets, where the clay platelets align by the flow with their face normal parallel to the neutral

direction. They also propose that the particles orient first in the flow field, followed at even higher shear rates, by the stretching of polymer chain that interconnect clay particles.[43-45]

Lin-Gibson *et al*.[70, 71] performed simultaneous light scattering and optical microscopy experiments under shear, on gels having the same polymer and clay composition as those reported by Schmidt *et al*.,[43-45] to compare flow induced structural changes on micrometer length scales. The observed features result predominantly from shear orientation of network active polymer and clay components. They suggested that on a micron length scale as visualized by light scattering and optical microscopy, the shear disrupts the transient network, and the stress leads to the formation of spatially modulated macro-domains. Weak periodicity arising from enhanced domain-domain interactions leads to a butterfly-shaped light-scattering pattern. Meanwhile the clay particles orient in response to the biaxial stress arising from the shear and elastic forces.[70, 71]

Baghdadi *et al*.[82] studied the kinetics of gel formation of Laponite-PEO dispersions of varying polymer molecular weight (M_w) using rheology. They examine solutions at both pH = 7, where interparticle attractions are present and a network gel is formed, and at pH = 10, where repulsive forces dominate and Laponite forms a colloidal glass. They found that PEO of low M_w slows down gelation and decreases the viscosity and elastic modulus of the dispersion at both pHs. At pH = 7, the adsorbed PEO forms a steric barrier and prevents the formation of an attractive gel, whereas at pH = 10, the PEO chains induce a depletion attraction between particles, preventing or slowing the formation of a colloidal glass. At higher M_w, PEO chains are long enough to create bridges between particles and form an associative network, enhancing the viscosity and

elastic modulus for both pHs. According to this study, the mechanisms and kinetics of gel formation are time dependent.

A more recent paper published by Daga *et al*.[136] presents the viscoelasticity behavior of Laponite-poly(ethylene oxide) solutions over a range of particle and polymer concentrations. They generate rheological master curves for the system by time-temperature superposition and time-concentration superposition. They observed that the addition of Laponite to a concentrated polymer solution increases the relaxation time but decreases the elastic modulus, which they attribute to the polymer adsorption and bridging.

1.10 Research Objective

Despite the extensive research on PEO-Laponite nanocomposites, these systems are still not well understood and there are many issues that still remain to be explored. Our interest is focused on nanocomposites with high enough polymer and clay concentrations, where permanent gels are formed. At these high concentrations the entangled polymer chains are in a dynamic adsorption-desorption equilibrium with the clay particles and form a network. The overall objective of the research presented here is to understand the nanoscopic and microscopic structures that exist in these poly(ethylene oxide)-Laponite nanocomposites and their shear responses. A combination of microscopic, rheological, and neutron scattering techniques is used to provide a more complete physical picture of the structures observed in these Laponite-PEO hydrogels and to explain some of the unique behaviors observed previously. For example, the reason why the low M_w hydrogels are weak and compliant and the high M_w hydrogels have a gum-like consistency will be addressed.

In **Chapter 3**, the structure at rest is explored for hydrogels with varying polymer molecular weight. Results obtained from static small and ultra-small angle neutron scattering experiments are presented that provide information on the structure of these hydrogels on length scales between 3 and 15,000 nm. Complimentary transmission and scanning electron microscopy images provide direct visualization of the nano and micro meter structures presented, respectively.

In **Chapter 4**, a comprehensive rheological characterization for the different polymer molecular weight hydrogels is presented. The flow behavior of these polymer-clay nanocomposite gels was studied through individual time dependent, constant rate experiments where the steady-state viscosities were measured as a function of shear rate. The viscoelastic properties of the gels at low deformations and low frequencies were also tested through oscillatory shear experiments. Finally, results from constant stress (creep) experiments are presented.

In **Chapter 5**, the unique flow properties exhibited by these complex fluids are correlated with their structural deformation through shear-SANS experiments. The effects of changing the molecular weight, the polymer and clay concentration, along with the preparation method on the shear-induced structures are explored. Furthermore, shear-SANS experiments in deuterated solvents were accompanied by experiments in contrast matched solvents, in order to elucidate the shear response of each nanoscopic component individually.

Finally, in **Chapter 6,** the data presented are summarized and conclusions are drawn with an outlook to future directions in this field.

CHAPTER 2 METHODS AND PRINCIPLES

2.1 Rheology

The word rheology derives from the Greek words rhei (ρέει), which means to flow, and logos (λόγος), which means to study. *Rheology* is the study of flow and deformation of bodies when they are subjected to external mechanical forces.[137] Materials will react to an applied force by exhibiting either elastic or viscous response, or more commonly, a combined response of the two, which is termed viscoelasticity.[138] *Elasticity* is the ability of a material to store deformation energy, and regain its original shape after being deformed.[138] *Viscosity* is the measurement of the material's ability to resist flow and to dissipate deformational energy.[138] The instruments that are commonly used to test the viscoelastic response of materials are called rheometers. The section that follows describes the three most commonly used shear-flow rheometric devices.

2.1.1 Rheometric Devices

The simplest rheological device is shown in Figure 2.1. The sample is placed between two parallel plates of area A that are separated by a distance Δy. When a force F is applied to the upper plate, the upper plate moves a distance Δx and establishes a velocity relative to the lower plate. The sample is forced to shear and its degree of deformation is measured.

The *shear stress*, τ, is defined as the shear force required to move the top plate in relation to the bottom plate, divided by the area over which the force acts.[137]

$$\tau = \frac{F}{A} \tag{2.1}$$

The *shear strain*, γ, is the amount of shear displacement (Δx) divided by the distance between shearing surfaces (Δy).

$$\gamma = \frac{\Delta x}{\Delta y} \tag{2.2}$$

The *shear rate*, $\dot{\gamma}$, can then be defined as the rate of the deformation ($d\gamma/dt$) for small values of Δx.

$$\dot{\gamma} = \frac{d\gamma}{dt} \tag{2.3}$$

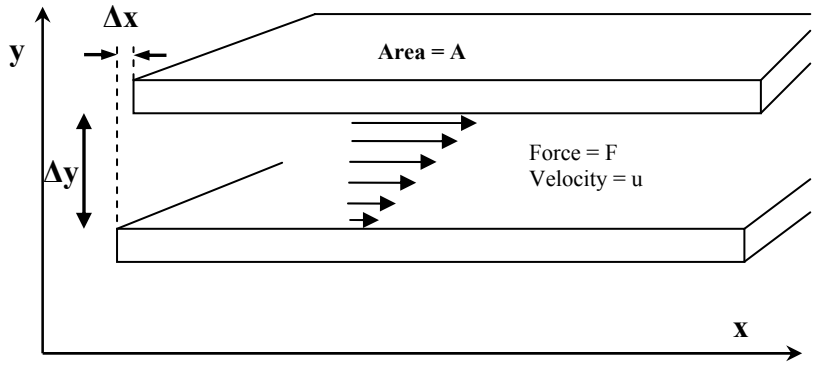

Figure 2.1: Schematic representation of a rheometer with sliding plates

A sketch of a rheometer with parallel disks (plates) of radius R and a gap h between them is shown in Figure 2.2. The sample is placed between the plates and is forced to shear when one of the plates is rotating with a constant angular velocity of Ω, while the other one is stationary. If we assume that there is no slip at these surfaces and neglecting the inertial forces, then the shear strain (γ), shear rate ($\dot{\gamma}$), and shear stress (τ) can be obtained from equations 2.4, 2.5, and 2.6 respectively:[137]

$$\gamma(r) = \frac{r\,\theta}{h} \tag{2.4}$$

$$\dot{\gamma}(r) = \frac{r\,\Omega}{h} \tag{2.5}$$

$$\tau(r) = \frac{M}{2\pi R^3}\left[3 + \frac{d\ln M}{d\ln\dot{\gamma}(r)}\right] \tag{2.6}$$

where θ is the angular displacement, r is the distance from the axis of rotation, h is the gap between the two plates, Ω is the angular velocity and M is the measured torque.

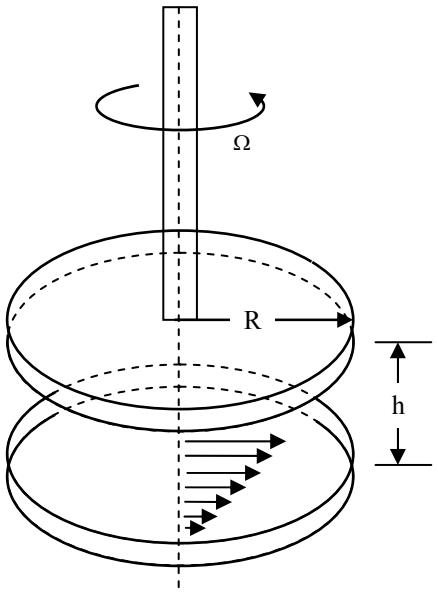

Figure 2.2: Schematic representation of a rheometer with parallel disks (plates)

The third rheological device most commonly used is the Couette Rheometer. It is composed of two concentric cylinders and is mainly used for liquid-like samples. The sample is placed between the cylinders and is forced to shear when the outer cylinder of radius R_o is driven at a constant angular velocity of Ω (usual units of rad/s) with respect to the inner cylinder of radius R_i, as illustrated in Figure 2.3. Using the assumption that there is no-slip of the fluid at the surface of the two cylinders, the velocity profiles at the boundary conditions are given by:[137]

$$\gamma(r) = \frac{r(R_o + R_i)}{2(R_o - R_i)} \tag{2.7}$$

$$\dot{\gamma}(r) = \frac{2\Omega R_i^2 R_o^2}{r^2\left(R_i^2 - R_o^2\right)} \tag{2.8}$$

$$\tau(r) = \frac{M}{2\pi r^2 L} \tag{2.9}$$

where r is the distance from the axis of rotation, L is the length of the inner cylinder, Ω is the angular velocity and M is the measured torque.

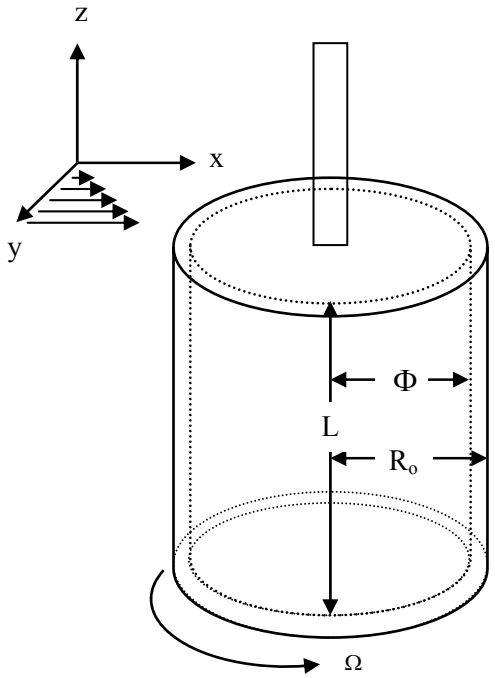

Figure 2.3: Schematic representation of a Couette rheometer with concentric cylinders

2.1.2 Elastic Solids and Viscous Liquids

For solids, the simplest relation between force and deformation is Hooke's law that says that the applied force is directly proportional to the deformation. It is expressed mathematically as:[137]

$$\tau = G_0\,\gamma \tag{2.10}$$

where τ is the applied force per unit area (stress) and γ is the deformation developed in the material (strain). The proportionality constant, G_0, is known as the modulus of the material and is a measure of its stiffness or its ability to resist deformation.[139] Materials for which Hooke's law is a useful approximation are known as *ideal elastic solids*.[137]

For liquids, the simplest equation that describes the relation between the force and the deformation is Newton's law. It states that the applied force per unit area (stress, τ) is directly proportional to the rate of deformation (shear rate, $d\gamma/dt$).[137]

$$\tau = \eta_0 \frac{d\gamma}{dt} \tag{2.11}$$

The proportionality constant, η_0, is the Newtonian viscosity.[139] Materials for which Newton's law is a useful approximation and their viscosity does not depend upon the shear rate are known as *ideal viscous fluids* or *Newtonian fluids*.[137]

In reality however, most materials deviate from Hooke's and Newton's laws in a number of ways. For example, the viscosity of a fluid may change when it is sheared. This is called a non-Newtonian fluid and its viscosity η is related to the shear rate $d\gamma/dt$ through the following power-law equation:[140]

$$\eta = K\left(\frac{d\gamma}{dt}\right)^m \tag{2.12}$$

In the above equation, K is called the consistency index and m is the power-law index. When the viscosity of a fluid increases with shear rate then the fluid is a *shear-thickening* fluid; however, if its viscosity decreases with shear rate then it is a *shear-thinning* fluid (Figure 2.4).[139] The simplest example of a shear-thinning material is ketchup. If ketchup is left untouched in the bottle it will barely move, but when sheared it flows out from the bottle.[137] A simple example of a shear-thickening material is a mixture of cornstarch and

water. When cornstarch is added to water, and the mixture is heated up and stirred, it thickens rapidly and mixing becomes more difficult.[137]

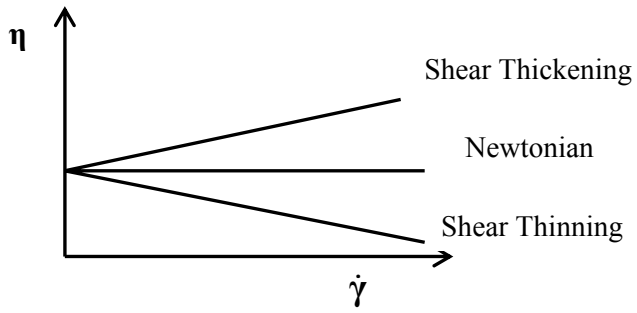

Figure 2.4: The viscosity (η) as a function of shear rates ($\dot{\gamma} = d\gamma/dt$)

Generally, when a stress is applied, viscous materials deform linearly with time. Elastic materials deform instantly and once the stress is removed, they quickly return to their original state.[137] On the other hand, viscoelastic materials like polymer-clay gels combine both of these properties and exhibit time dependent deformations. Thus, more complex equations are needed to describe their behavior such as the following:[137]

$$\tau(t) = \int_{-\infty}^{t} G(t - t')\, \dot{\gamma}(t')\, dt' \qquad (2.13)$$

In the above expression, the stress is an integral of the relaxation modulus G(t), multiplied by the rate of strain, $\dot{\gamma}(t')$.[137] Since the deformation might be changing with time, $\dot{\gamma}$ is also a function of time. The variable t' is the past time and t is the present time.[137]

2.1.3 Dynamical Experiments

The viscoelastic behavior of materials is studied using dynamical oscillatory shear experiments. In dynamical experiments, the imposed oscillatory strain, γ, on the sample

is a function of the initial strain, γ_0, the frequency, ω, and the time, t, and is described by the following equation:[137]

$$\gamma = \gamma_0 \sin(\omega t) \tag{2.14}$$

For viscoelastic samples, the responding stress will be shifted by a phase angle, δ, with respect to the strain wave. The stress, τ, can be expressed by the following equation:[137]

$$\tau = \tau_0 \sin(\omega t - \delta) \tag{2.15}$$

The response consists of two contributions. The first is the stress that is in phase with the strain and is called elastic stress (τ'). The second contribution comes from the stress that is shifted by a factor of $\pi/2$ with respect to the strain and is in phase with the rate of strain. This is called viscous stress (τ'').[137]

$$\tau = \tau_0 \sin(\omega t - \delta) = \tau_0 [\sin(\omega t)\cos\delta - \cos(\omega t)\sin\delta] = \tau' + \tau'' \tag{2.16}$$

The above equation can be written also as:

$$\tau = \tau_0' \sin(\omega t) - \tau_0'' \cos(\omega t) \tag{2.17}$$

Thus, the dynamic moduli (the ratio of stress to strain) can be given by the following two equations:[137]

$$G' = \frac{\tau_0'}{\gamma_0} = \frac{\tau_0}{\gamma_0}\cos\delta \tag{2.18}$$

$$G'' = \frac{\tau_0''}{\gamma_0} = \frac{\tau_0}{\gamma_0}\sin\delta \tag{2.19}$$

In the above expression G' is the elastic (or storage) modulus, which represents the ability of a material to store elastic energy, and G'' is the viscous (or loss) modulus, which represents the ability of a material to dissipate energy.[137]

2.2 Small Angle Neutron Scattering (SANS)

Small Angle Neutron Scattering (SANS) is a powerful technique for determination of particle shape and size in the range of 1 to 300 nm. It also can provide information about the orientation of particles and inter-particle correlations, as well as other system properties such as specific volume and surface area of a particle.[141] SANS has been used for over 30 years to study the nanostructure of alloys, ceramics, polymers, colloids, and other materials.[141, 142] The technique requires a neutron source, which can be either a nuclear reactor or a spallation source; therefore, the experiments are performed at large-scale facilities.[143]

SANS is widely used in polymer and colloidal science because it is sensitive to light elements such as hydrogen, oxygen, carbon, nitrogen etc. It is also used to study magnetic samples, since the neutron has a magnetic moment that can interact with the magnetic moments of unpaired electrons in certain atoms.[141] Additionally, since neutrons are highly penetrating, SANS can be employed to study thick samples that cannot be studied with the SAXS techique.[144] Also SANS is a non-destructive technique, which makes it ideal for biological samples, that can be sensitive to the high energies, like those from x-ray sources.[141] However, the "beauty of SANS" is that it can distinguish between isotopes. For example, hydrogen and deuterium have very different scattering lengths and for that, they are used in contrast variation measurements. In a multi-component system, the substitution of hydrogenated molecules with deuterated ones can alter the scattering from the system and enables the highlighting of scattering from different components in the system under study.[143]

2.2.1 The Scattering Vector

In a neutron scattering experiment, the neutron beam is deflected from its original direction by interaction with the nuclei in the sample. Some of the incident neutrons are scattered from the atoms and change direction without loosing energy. This is called elastic scattering.[144] Neutrons may exchange energy with the atoms in the material, giving rise to inelastic scattering.[144] In addition, a fraction of the incident beam is transmitted through the sample unimpeded. The vector diagrams in Figure 2.5 illustrate (a) the elastic and (b) the inelastic scattering processes. The neutron incident beam has a wavelength $\lambda_{i,}$ and is described by the wave vector $\vec{k}_i$, where $k_i = 2\pi/\lambda_i$.[144, 145] The incident beam when it hits the sample is scattered through an angle 2θ. The final scattered beam has a wavelength λ_f, and is described by the wave vector $\vec{k}_f$.[144, 145]

(a) elastic scattering (b) inelastic scattering

Figure 2.5: Vector diagram showing the relationship between the incident wave vector $\vec{k}_i$, the scattering wave vector $\vec{k}_f$, and the momentum transfer $\vec{q}$, which is obtained by subtracting the scattering wave vector from the incident wave vector. For (a) elastic scattering the incident and scattered beams have the same energy, whereas for (b) inelastic scattering there is an energy change

By subtracting the two wave vectors, one can obtain the momentum transfer $\vec{q}$:[144]

$$\vec{q} = \vec{k}_i - \vec{k}_f \Rightarrow |\vec{q}| = \sqrt{k_i^2 + k_f^2 - 2k_i k_f \cos 2\theta} \qquad (2.20)$$

If the scattering is elastic ($|\vec{k}_i| = |\vec{k}_f|$), then $|\vec{q}|$ is given by the following equation:[144]

$$|\vec{q}| = \left(\frac{4\pi}{\lambda}\right)\sin\theta \tag{2.21}$$

With the use of Bragg's Law ($\lambda = 2d\sin\theta$), the characteristic dimension of a material, d, which represents the period of repetition in the structure or the spacing between particles, can be calculated as follows:[144]

$$d = \frac{\lambda}{2\sin\theta} = \frac{\lambda}{2\left(\frac{q\lambda}{4\pi}\right)} = \frac{2\pi}{q} \tag{2.22}$$

The inverse relationship between the distance d, and the momentum transfer q, shown in the above equation, indicates that measurements at high q reveal nanoscale structures, whereas at low q reveal large-scale structures.

2.2.2 Scattering Lengths and Cross-Sections

The scattering theory considers a neutron beam traveling in the x-direction towards a single atom that is fixed at the origin, as it is shown in Figure 2.6. The incident neutrons are described by a plane wave function:[146]

$$\Psi_i = \exp(i\, k_i\, x) \tag{2.23}$$

Since the scattering derives from a single atom, it is assumed to be isotropic; the scattering neutron beam spreads out in spherical waves:[146]

$$\Psi_s = -\left(\frac{b}{r}\right)\exp(i\, k_f\, r) \tag{2.24}$$

The factor (1/r) in the wave function shows how a point field decays. The quantity b has the dimension of length and is called *scattering length*.[146] It measures the strength of the interaction between the neutron and the nucleus. The scattering length, b, depends on the type and spin of the nucleus and varies randomly from one nuclide to another, thus, it is

determined experimentally.[146] The unit of the scattering length, b, is the fermi (1 fermi = 10^{-15} m). The minus sign in the wave function means that b is a positive number for a repulsive interaction between neutron and nucleus.[146]

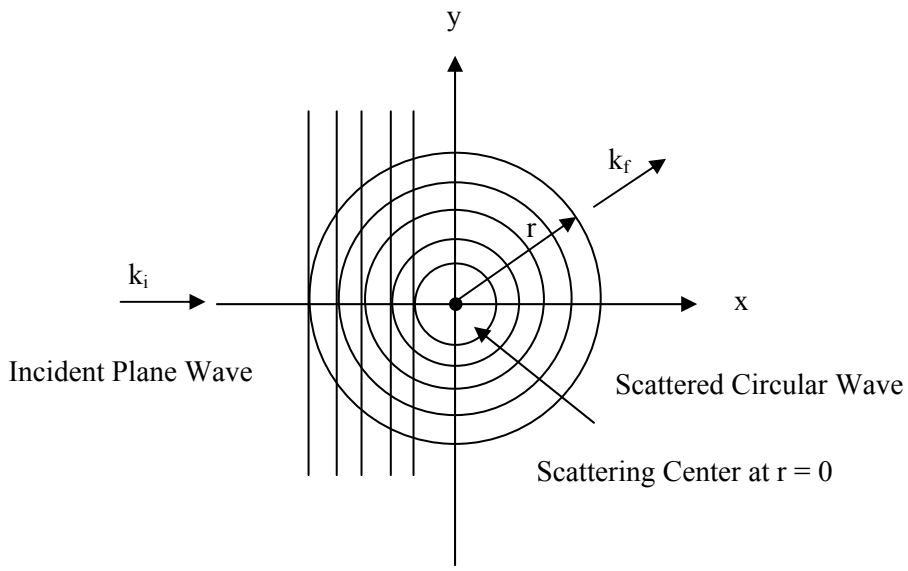

Figure 2.6: The incident neutron beam is described by plane waves; the scattering beam spreads out in spherical waves

The scattering by a single nucleus can be described in terms of *cross section*, σ, measured in barns (1 barn = 10^{-28} m^2) that is equivalent to the effective area that the nucleus presents to the passing neutron.[147]

$$\sigma = \frac{\text{number of scattered neutrons in all directions per second}}{\text{number of incident neutrons per area per second}} \qquad (2.25)$$

Both the scattering length and the cross section are a measure of the strength of the interaction between a neutron and a given nucleus. The cross section, σ, is related to the scattering length, b, by the simple relation:[146]

$$\sigma = 4\pi b^2 \qquad (2.26)$$

Since it is easier to think in terms of material properties rather than atomic properties the *scattering length density*, ρ, for a molecule with N atoms is used, which is defined as:[143]

$$\rho = \frac{d\, N_A}{M_0} \sum_k^N b_k \tag{2.27}$$

In the above expression, b_k is the scattering length of the kth of N atoms in a molecule, d is the density of the material, M_0 is the molar mass of the material, and N_A is Avogadro's number (N_A = 6.022 x 10^{23} mol^{-1}). In a subvolume of a material not all the molecules have identical scattering length densities, and the scattering length density of the material fluctuates around a mean value.[144]

The scattering cross section refers to scattering in all directions. In order to calculate the scattering into a unit solid angle Ω, the differential scattering cross section is used, also denoted as intensity, $I(\vec{q})$.[144] The angular dependence on scattering $\frac{d\sigma}{d\Omega}$, is given by:[144]

$$I(\vec{q}) = \frac{d\sigma}{d\Omega} = \frac{1}{V}\left\langle \left| \sum_k^N b_k \exp(i\,\vec{q}\,\vec{r}_k) \right|^2 \right\rangle = \left\langle \left| \int_V \rho(\vec{r}) \exp(i\,\vec{q}\,\vec{r})\, d\vec{r} \right|^2 \right\rangle \tag{2.28}$$

In the above expression, b_k is the scattering length of the kth atom located at some position vector $\vec{r}_k$, and $\rho(\vec{r})$ is the scattering length density of a subvolume of a particle located at some position vector $\vec{r}$, from the particle center of mass.[144] The bracket represents an average over all possible equilibrium configurations.[148] The neutron scattering intensity, $I(\vec{q})$, has units of reciprocal length (cm^{-1}) and is a measure of the number of neutrons of a given wavelength, scattered through a particular angle, that arrive on a small area on the detector in a unit time.[144]

2.2.3 Coherent and Incoherent Scattering

There are two types of scattering. The first is the *coherent scattering* in which the neutron wave interacts with the whole sample as a unit, and the scattered waves from different nuclei interfere with each other. This type of scattering depends on the relative distances between the atoms and gives structural information about the material.[147] Elastic coherent scattering gives information about the equilibrium structure. Inelastic coherent scattering provides information about the collective motions of the atoms (how a particle moves with respect to the other particles).[147] The second type of scattering is the *incoherent scattering*. Here the neutron wave interacts independently with each nucleus in the sample and the scattered waves from different nuclei do not interfere.[147] Incoherent scattering provides information about atomic diffusion (how a particle moves with respect to itself). The majority of isotopes and elements mostly scatter coherently, besides hydrogen that scatters very strongly incoherently.[146]

The scattered intensity that is measured in a neutron scattering experiment, which results from scattering of N atoms, is the sum of both the coherent and incoherent scattering and is given by the following formula:[146, 148]

$$I(\vec{q}) = \frac{1}{V}\left\langle \left| \sum_{k}^{N} b_k \exp(i\,\vec{q}\,\vec{r}_k) \right|^2 \right\rangle = \frac{1}{V}\left\langle \sum_{k,j}^{N} b_k b_j \exp(i\,\vec{q}\,(\vec{r}_k - \vec{r}_j)) \right\rangle = I_{coh}(\vec{q}) + I_{incoh}(\vec{q}) \quad (2.29)$$

The vectors r_k and r_j represent the positions of k and j atoms respectively.[148]

The work presented here deals mainly with elastic coherent scattering, which is q-dependent and contains structural information. The incoherent scattering contributes only to the noise level and it is treated as a flat background.

2.2.4 Structure Factor and Form Factor

For a system consisting of N identical particles dispersed in a solvent, the scattering intensity is proportional to the form factor $P(\vec{q})$ of the particles, multiplied by the structure factor, $S(\vec{q})$. The basic scattering equation is the following:[143, 147]

$$I(\vec{q}) = (\rho_p - \rho_{solv})^2 \, N_p \, V_p^2 \, P(\vec{q}) \, S(\vec{q}) + I_{back} \tag{2.30}$$

where N_p is the number density of the particles, V_p is the volume of a particle, I_{back} is the isotropic incoherent background signal, and the contrast term $(\rho_p - \rho_{solv})^2$ refers to difference in the scattering length density between the particle and the medium (solvent), respectively. In most experimental situations the volume fraction (Φ_p) is often a more convenient term to use than the number concentration ($N_p \, V_p = \Phi_p$), so the above equation can be rewritten as: [143, 147]

$$I(\vec{q}) = (\rho_p - \rho_{solv})^2 \, \Phi_p \, V_p \, P(\vec{q}) \, S(\vec{q}) + I_{back} \tag{2.31}$$

The *form factor* $P(\vec{q})$ is a function that describes how the scattering intensity is modulated by interference effects between neutrons scattered by different parts of the same particle.[147] Therefore, this function contains information about the *intraparticle* structure. For dilute suspensions where the scattering intensity depends only on this factor, information about the particle size and shape can be obtained.[147]

The *structure factor* $S(\vec{q})$ corresponds to the interference effects between the neutrons scattered by different particles in a system. Therefore, $S(\vec{q})$ is characteristic of the *interparticle* structure and gives information about the correlations between particles. One of the ways to calculate the $S(\vec{q})$ in a concentrated dispersion is dividing the

scattering intensity from the concentrated dispersion ($I_{conc}(\vec{q})$), by the scattering intensity from a dilute dispersion ($I_{dil}(\vec{q})$), and scaling by their respective volume fractions, as shown in equation 2.32.[46]

$$S(\vec{q}) = \frac{I_{conc}(\vec{q}) \cdot \Phi_{dil}}{I_{dil}(\vec{q}) \cdot \Phi_{conc}} \tag{2.32}$$

This approach assumes that for the dilute dispersion the $S(\vec{q}) = 1$ and the scattering intensity is determined only by the form factor, $P(\vec{q})$. $P(\vec{q})$ is a function of the particle dimensions, therefore for systems whose particle size and shape are independent of concentration, it must be identical for the dilute and concentrated dispersions.

2.2.5 Guinier Approximation

As stated above, when the experiment is carried out on a dilute solution, the scattering intensity is equal to the form factor. In this case, the Guinier approximation (shown in equation 2.33) can be used to obtain information about the particle size.[144, 147]

$$\ln I(q) \approx \ln I(0) - \frac{q^2 R_g^2}{3} \tag{2.33}$$

According to this approximation, which is only valid at low q values, the natural logarithm of the scattering intensity, lnI(q), is a linear function of the square of the scattering vector magnitude, q^2. From a Guinier plot (shown in Figure 2.7), the radius of gyration R_g can be calculated from the slope at low q values, through the following equation:[144]

$$R_g = \sqrt{3|\text{slope}|} \tag{2.34}$$

The radius of gyration is characteristic of the size of the particles and is explained in more detail in section 2.6.3. The Guinier approximation can be applied even if the particles are of irregular or unknown shape.[144]

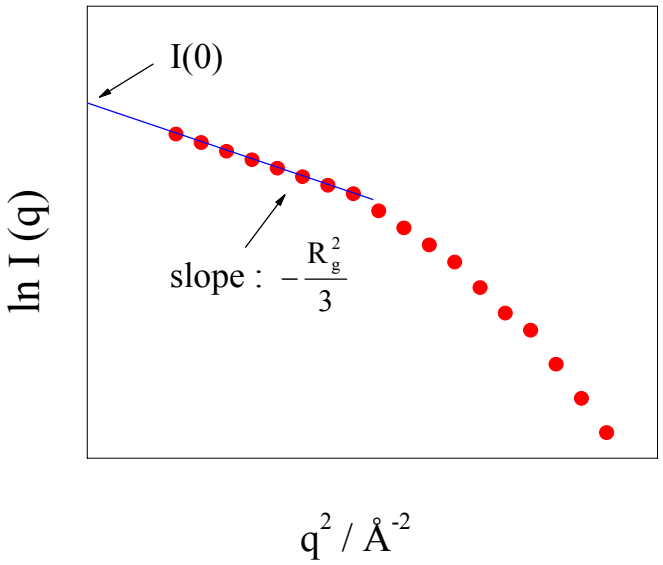

Figure 2.7: A Guinier plot, where the lnI(q) is plotted as a function of q^2 and the R_g is calculated from the slope in the low q region

2.2.6 Contrast Matching

In the case of a two-component system such as that presented in this work, a system of PEO and Laponite RD (LRD) dispersed in a solvent, the scattering intensity depends on three partial structure factors. These are related to the correlations of PEO-PEO ($S_{PEO\text{-}PEO}(\vec{q})$), LRD-LRD ($S_{LRD\text{-}LRD}(\vec{q})$), and PEO-LRD ($S_{PEO\text{-}LRD}(\vec{q})$):[41, 42]

$$I(\vec{q}) \cong (\rho_{PEO} - \rho_{solv})^2 S_{PEO\text{-}PEO}(\vec{q}) + (\rho_{LRD} - \rho_{solv})^2 S_{LRD\text{-}LRD}(\vec{q}) + 2(\rho_{PEO} - \rho_{solv})(\rho_{LRD} - \rho_{solv}) S_{PEO\text{-}LRD}(\vec{q}) + I_{back} \quad (2.35)$$

In the above expression ρ_{PEO}, ρ_{LRD} and ρ_{solv} are the scattering length densities of the PEO, LRD and solvent, respectively and I_{back} is the isotropic incoherent background.

If one wishes to highlight the scattering from individual components, the contrast matching technique is very useful. Through this technique, the scattering of only one component is observed while the scattering of the other component is neglected. This can be achieved by tuning the scattering length density of the solvent to be equal to the scattering length density of one of the components. That component then appears "invisible" to the neutron beam and is said to be "contrast matched". For example, in the above-mentioned system, if one tunes ρ_{solv} to be equal to ρ_{PEO}, then the above equation becomes:[66]

$$I(\vec{q}) \cong (\rho_{LRD} - \rho_{solv})^2 S_{LRD\text{-}LRD}(\vec{q}) + I_{back} \qquad (2.36)$$

Hence, the scattering from the polymer is neglected and only information from the clay can be evaluated.[66] Equally, one may make the clay invisible and observe the scattering from the polymer.[66]

(a) $\rho_{solv} \neq \rho_{LRD} \neq \rho_{PEO}$ (b) $\rho_{solv} = \rho_{LRD} \neq \rho_{PEO}$ (c) $\rho_{solv} = \rho_{PEO} \neq \rho_{LRD}$

Figure 2.8: Schematic showing the different contributions to the total scattering as the scattering length density of the solvent is changed. The scattering length density of the solvent is matched (b) to the Laponite and (c) to the PEO

The principle of contrast matching is shown as a cartoon in Figure 2.8. If the scattering length density of the solvent is different from the scattering length density of the polymer and the clay, then both polymer and clay contribute to the total scattering

(Figure 2.8a). If the scattering length density of the solvent is matched to the scattering length density of the Laponite particle ($\rho_{solv} = \rho_{LRD}$), then the only contribution to the scattering is from the polymer (Figure 2.8b). If the scattering length density of the solvent is matched to the polymer chain, ($\rho_{solv} = \rho_{PEO}$) then the only contribution to the scattering is from the Laponite particle (Figure 2.8c).

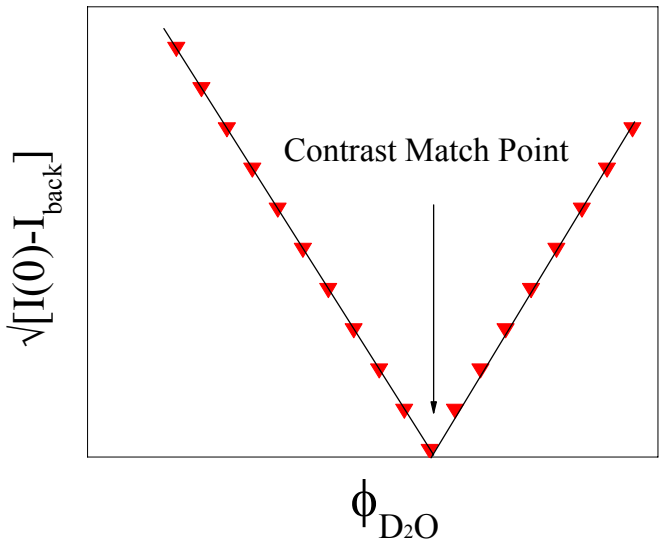

Figure 2.9: The contrast match point for a particle can be obtained from the contrast match plot, where the square of the scattering intensity (at q = 0) is plotted against the volume percentage of D_2O in the sample

The easiest way of contrast matching a particle is by mixing hydrogenated and deuterated forms of the solvent in the correct ratio. In order to calculate the correct D_2O/H_2O ratio that has the same scattering length density as the particle, a series of solutions is prepared. These have the same particle concentration but varying D_2O/H_2O composition. The scattering intensity of each of these solutions is measured and plotted as a function of q. From the scattering profiles, the I(0) is obtained by extrapolating the

scattering intensity to q = 0.[66] To create a contrast match plot (an example is shown in Figure 2.9), the square root of the I(0) minus the incoherent background is plotted against the volume percentage of D_2O (Φ_{D_2O}) in the sample. According to equation 2.31 at the contrast match point where ($\rho_p = \rho_{solv}$) this plot has a minimum. From the volume fractions of D_2O (Φ_{D_2O}) and H_2O (Φ_{H_2O}) at the contrast match point, the scattering length density of the particle, ρ_p, can be calculated as follows:

$$\rho_{D_2O}\,\Phi_{D_2O} + \rho_{H_2O}\Phi_{H_2O} = \rho_p \tag{2.37}$$

where ρ_{D_2O} ($= 6.36\times10^{-6}\,\text{Å}^{-2}$) and ρ_{H_2O} ($= -0.56\times10^{-6}\,\text{Å}^{-2}$) are the scattering length densities of the D_2O and H_2O.

2.3 SANS under Shear (Shear-SANS)

As was already mentioned in section 1.3, shear may induce structural changes in systems that contain anisotropic species. To study the structural changes with neutron scattering, a Couette geometry shear cell[149] (shown in Figure 2.10) can be used. The sample is placed in the cell and continuously sheared between the two concentric cylinders, one of which rotates while the other one is stationary. As Figure 2.10 illustrates, in order to obtain information in the three directions of space (x, y, and z direction) SANS measurements have to be carried out in two configurations. In the standard configuration called *radial beam geometry*, the incident beam is parallel to the shear gradient (y direction) and passes through the center of the annular cell. In the second configuration called *tangential beam geometry*, the incident beam is parallel to the flow direction (x direction) and passes through the side of the cell (tangential to the

cell annulus).[44] The radial beam configuration (y direction), provides information in the flow-neutral (x-z) plane, while the tangential beam configuration (x direction), provides information in the gradient-neutral (y-z) plane. From the 2D SANS patterns obtained in the two beam configurations, the intensity as a function of q can be calculated in the three directions of space (x, y, and z direction).[53]

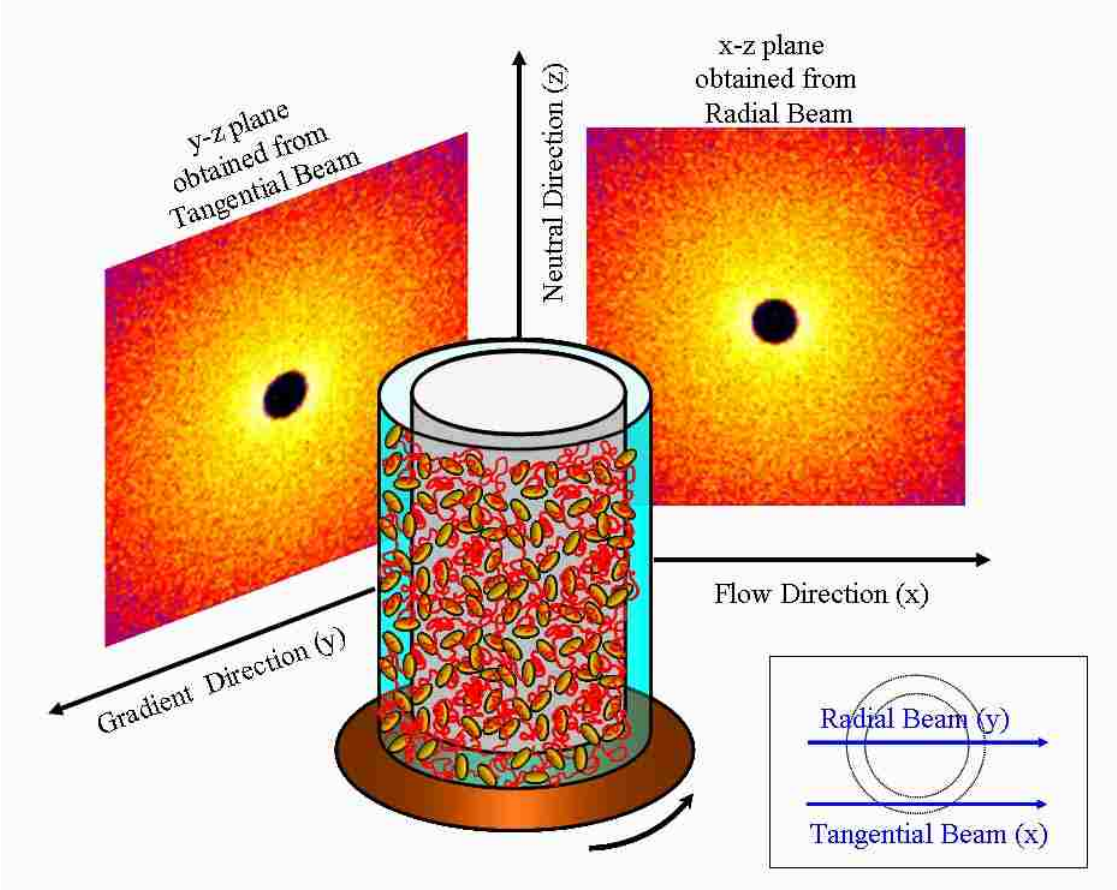

Figure 2.10: Schematic of a Couette type shear cell illustrating how the two beam configurations provide information in the three directions of space. Information in the flow-neutral (x-z) plane is obtained from the radial beam, while information in the gradient-neutral (y-z) plane is obtained from the tangential beam. Within the cell, a model shows the isotropic polymer-clay system. **Insert:** The radial and tangential beam geometries pass through the center and the side of the annular cell, respectively

By combining both radial and tangential 2D data, the 3D space orientation of the clay platelets can be determined as shown in Figure 2.11. If the platelets align with their

face normal parallel to the neutral (z) direction ('a'-orientation), then both the radial and the tangential patterns will be anisotropic along the z-direction. If the platelets align with their face normal parallel to the flow (x) direction ('b'-orientation), then anisotropy is developed along the x-direction in the radial pattern and the tangential pattern is isotropic. If the platelets align with their face normal parallel to the gradient (y) direction ('c'-orientation), then the radial pattern is isotropic and anisotropy is developed along the y-direction in the tangential pattern.[53]

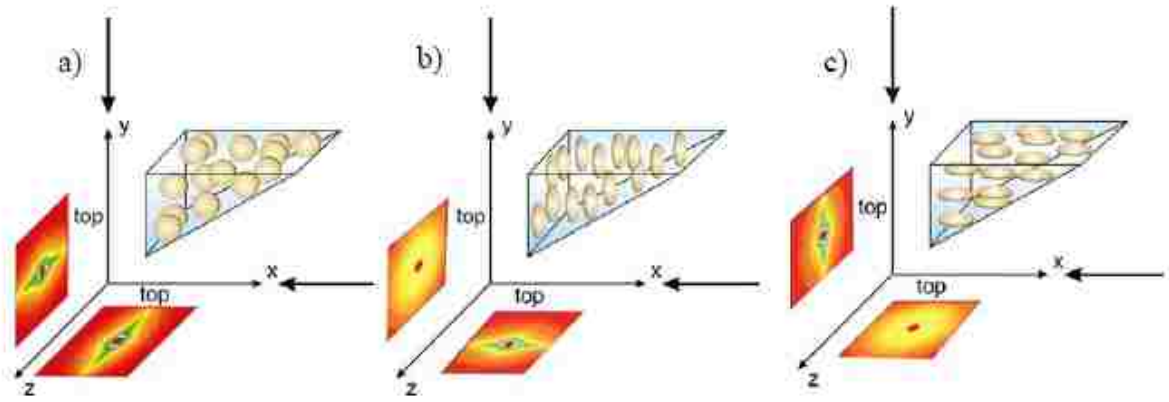

Figure 2.11: SANS patterns revealing the orientation of clay platelets. The x-z plane is obtained from measurements in the radial beam and the y-z plane is obtained from measurements in the tangential beam. Platelets align with their face normal parallel to the (a) neutral – z, (b) flow – x, and (c) gradient - y direction. (Reprinted with permission from *Current Opinion in Colloid & Interface Science*, Schmidt, G.; Malwitz, M. M, Properties of polymer-nanoparticle composites, **2003**, 8, 103-108. Copyright 2003 Elsevier.)

2.4 Ultra-Small Angle Neutron Scattering (USANS)

When a material contains structures with larger length scales than those probed with SANS, then Ultra Small Angle Neutron Scattering (USANS)[150] technique is used. The typical measurement range of the instrument extends from 3 x 10^{-5} $Å^{-1}$ to 5 x 10^{-3} $Å^{-1}$ in scattering wave vector (q), providing information on material structure over the size

range from 0.1 μm to 20 μm.[151] There are several complimentary techniques to study the structure of micron-sized particles, such as scanning electron microscopy, light scattering, and atomic force microscopy.[152] However, these techniques cannot be applied to all types of materials, such as opaque materials (for light scattering), or materials with magnetic structures (for microscopy).[152] In such cases, where contrast enrichment is necessary, neutron scattering can provide all the structural information. Furthermore, the ability to selectively deuterated molecules, gives unique information not available from other techniques. Of course, USANS, like any scattering technique gives a quantitative average value while microscopy only gives individual values. Systems that are mostly studied by USANS are mixtures of micro-particles, colloids, liquid crystals, silicon macropore arrays, filled polymers, cements, microporous media, and micro-emulsions, among others.[153]

The USANS instrument consists of a double crystal diffractometer that uses multi reflections from large silicon perfect single crystals, to produce both high beam intensity and low instrument background.[151] The diffraction from perfect crystals provides very high angular resolution and extends the q range to much smaller values than feasible (with pinhole collimation) SANS instruments.[151] The sample is placed between the two crystals and the analyzer is rotated by a small angle from the aligned condition and reflects the scattered neutrons into the detector.[151] The detector is placed such that it collects only neutrons coming from the diffracted beam from the analyzer.[151] The setup provides excellent angular collimation in one direction only (horizontal), so that the obtained angular resolution in only good in that direction. The measured slit-smeared scattering intensity can be desmeared by several different inversion methods.[151]

2.5 Electron Microscopy

Electron microscopy can provide higher magnification and a better resolution than optical microscopy, because electrons travel at shorter wavelengths than light. However, since electrons, and not photons, are used to enlarge the views of the specimens, the resulting images are black and white. Usually the sample is coated with a replica, to provide a path for the negatively charged electrons.[154] Once the electrons encounter the specimen, they can scatter without losing energy (elastic scattering), or they can be absorbed by the specimen and produce secondary electrons (inelastic scattering), current, light, or any combination of the previous. They can also pass through the sample unimpeded. The two types of microscopy used in this work are: (a) scanning electron microscopy (SEM) and (b) transmission electron microscopy (TEM).

2.5.1 Scanning Electron Microscopy (SEM)

Scanning electron microscopy uses a focused beam of electrons to scan the surface of a specimen (that is placed at the end of beam) and to generate secondary electrons from the surface. Secondary electrons (or backscattered electrons) are collected by a detector and converted into an image on a screen.[154] Thus, a three-dimensional image of the surface of the specimen is produced. The specimen should be electrically conductive, thus, it is coated with osmium, gold, palladium, iridium, or any combination of the previous.[154] SEM yields information mostly about micrometer-scale structures. Environmental scanning electron microscopy is used to examine hydrated specimens at a reduced air pressure. Humid environmental conditions are retained by adjusting the temperature and the pressure in the chamber, to avoid solvent evaporation. ESEM is

particularly useful for hydrated samples such as plants, fruits, hydrogels, and many others.

2.5.2 Transmission Electron Microscopy (TEM)

In transmission electron microscopy, the specimens are examined by passing the electron beam through them and revealing more information about the internal structure of the specimens. The 2-D image is produced in the form of a shadow on a fluorescent screen.[155] The samples are frozen or placed in a resin and sliced into ultra thin sections. The specimens are then treated with heavy metals to obtain better contrast. TEM yields information about structures on the nanometer and micrometer length scale.

2.6 Physicochemical Principles

2.6.1 Polymers in Solution

Polymers are macromolecular materials built up of a large number of repeating units of identical structure called monomers, which are linked together by covalent bonds. The number of the repeat units in the polymer chain is called the degree of polymerization. Multiplying the degree of polymerization with the molecular weight of a single monomer, one can derive the polymer molecular weight. Most synthetic polymers contain chains with a wide molecular weight distribution.[140] The exact breadth of this distribution depends on the specific conditions of the polymerization process. For example, the polymerization of some polyolefins results in an extremely broad molecular-weight distribution, while protein synthesis delivers near monodispersed distributions.[140] In order to characterize an individual polymer sample, it is necessary to define an average molecular weight.

The number average molecular weight, M_n, is defined as:[140]

$$M_n = \frac{\sum_i^{\infty} N_i M_i}{\sum_i^{\infty} N_i} \tag{2.38}$$

where N_i is the number of molecules with molecular weight M_i.

The weight average molecular weight, M_w, is defined as:[140]

$$M_w = \frac{\sum_i^{\infty} N_i M_i^2}{\sum_i^{\infty} N_i M_i} \tag{2.39}$$

The ratio M_w/M_n is a measure of the polydispersity of the sample. Samples which posses a narrow molecular weight distribution normally have values of $M_w/M_n < 1.1$, where samples with $M_w/M_n > 1.1$, is usually considered polydisperse.[140]

Another type of average that is z-average that is defined as:

$$M_z = \frac{\sum_i^{\infty} N_i M_i^3}{\sum_i^{\infty} N_i M_i^2} \tag{2.40}$$

2.6.2 An Ideal Chain in Dilute Solution

A long polymer chain in solution has many degrees of freedom. For example, it is free to rotate around individual bonds and obtain almost a limitless number of conformations in three-dimensional space. The simplest way to describe the conformation of a polymer chain in a dilute solution is with the *freely jointed model*, otherwise known as the *random walk model*.[156, 157] In this model, a polymer chain has n

segments, each one represented by a vector of equal length l_i, in a linear sequence with no restrictions on the angles between successive bonds (Figure 2.12).[156, 157]

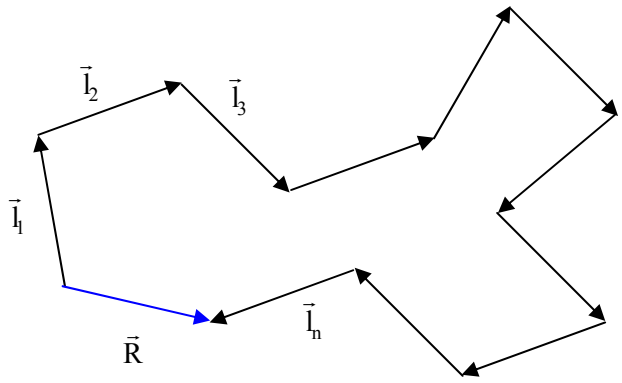

Figure 2.12: Schematic representation of a polymer chain with n segments of l length. The end-to-end distance, $\vec{R}$, is the vector sum of the bonds

The *end-to-end distance*, $\vec{R}$, joining one end of the polymer to the other end is given by the vector sum of the bonds:[156, 157]

$$\vec{R} = \vec{l}_1 + \vec{l}_2 + \vec{l}_3 + ... + \vec{l}_n = \sum_{i=1}^{n} \vec{l}_i \qquad (2.41)$$

The average value of $\vec{R}$ is zero, since the end-to-end vector has the same probability of being $\vec{R}$ as of being $-\vec{R}$, and the two contributions cancel out.[156] Therefore, in order to compute the average of all possible conformations of a polymer chain, the average of the square of $\vec{R}$ is used. It is referred to as the *mean-square end-to-end distance* and is calculated as:[156]

$$\left\langle \vec{R}^2 \right\rangle = n \vec{l}^2 \qquad (2.42)$$

Real polymer chains differ from the above idealized, freely jointed model, since they have fixed angles between bonds and rotation is sometimes restricted due to steric

hindrance. Additionally real chains contain atoms that have a finite volume and therefore some volume is excluded. This means that a real atom cannot occupy the same space as any other atom. In order to include the effects of fixed bond angles, restricted rotation and excluded volume, we can modify the freely jointed model and obtain the mean-square end-to-end distance using the following equation:[140, 158]

$$\left\langle \vec{R}^{\,2} \right\rangle = n\, \vec{l}^{\,2}\, C_n\, \alpha^2 \tag{2.43}$$

In the above expression, α is called the *chain expansion factor*, which is a measure of the excluded volume effect, and C_n is called the *characteristic ratio*, which contains the contribution from both fixed angles and restricted chain rotation.[140] For long polymer chains C_n is a constant characteristic for each polymer with typical values ranging from 5 to 10.[140]

2.6.3 Radius of Gyration and Hydrodynamic Radius

In section 2.6.2, a polymer chain was described as a series of bond vectors. If beads representing mass elements are added to the previous model, as shown in Figure 2.13, then a new parameter called the *radius of gyration*, R_g, can be defined.[158] This parameter is a more convenient way of expressing the size of a polymer than the mean-square end-to-end distance and in addition, can be directly measured in experiments.[156] The R_g is defined as the root-mean-square of mass-weighted-distances of each bead on the chain from the center of mass:[158]

$$R_g^2 = \left\langle \frac{\sum_i m_i r_i^2}{\sum_i m_i} \right\rangle \tag{2.44}$$

In the above expression, m_i is the mass of each bead that is located at a vector position r_i from the polymer center of mass (CM).

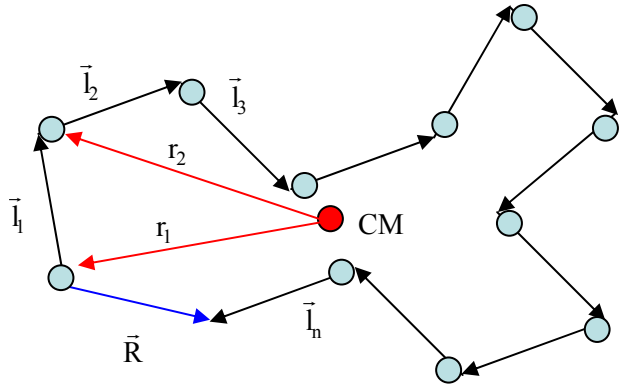

Figure 2.13: Schematic representation of a polymer chain. The vectors represent the bonds and the beads represent the mass elements, located at a vector position r from the polymer's center of mass

For an ideal chain, the radius of gyration is related to the mean-square end-to-end distance by the following equation:[159]

$$R_g^2 = \frac{\langle \vec{R}^2 \rangle}{6} \tag{2.45}$$

Generally, the radius of gyration, R_g, is a mathematical concept that describes the distribution of the value of a parameter around its central value. Besides polymer coils, the R_g applies to solid particles as well. For a solid object, R_g is given by:[144, 158]

$$R_g^2 = \frac{\int p(\vec{r})\, r^2 d\vec{r}}{\int p(\vec{r}) d\vec{r}} \tag{2.46}$$

In the above equation, $p(\vec{r})$ is the local density of a subvolume of a particle located at some position vector $(\vec{r})$ from the particle center of mass. The radius of gyration is obtained mainly from scattering experiments, as was shown in section 2.2.5. The R_g for

most shapes can easily be derived as a function of the main parameters of the shape. For example, the radius of gyration for a sphere of radius R is given as:[144]

$$R_g = \sqrt{\frac{3}{5}}R \tag{2.47}$$

The radius of gyration for a disc of radius R and thickness H is given as:[144]

$$R_g = \sqrt{\frac{R^2}{2} + \frac{H^2}{12}} \tag{2.48}$$

Another commonly used parameter for describing the size of a particle is the *hydrodynamic radius*, R_h, which is a measure of size of the solvated particle. The R_h is derived through the diffusional properties of the particle, and obtained mainly from sedimentation equilibrium and dynamic light scattering experiments. The hydrodynamic radius can be calculated from the Stokes-Einstein relationship:[160, 161]

$$R_h = \frac{K_B T}{6 \pi \eta_0 D_0} \tag{2.49}$$

In the above expression K_B is the Boltzmann constant, T is the absolute temperature, η_0 is the solvent viscosity and D_0 is the diffusion coefficient of the particle.

2.6.4 Overlap Threshold Concentration

As mentioned in section 2.6.2, the freely jointed model ignores any influence arising from the finite volume of the segments and from the interactions between the chain segments and the molecules of the solvent. However, in reality the size of the polymer chain will greatly depend on the type of solvent that surrounds the polymer.[156] In a *good solvent* the repulsions between polymer segments (since they tend to be in contact with solvent molecules rather than with other polymer segments) lead to an expansion the polymer dimensions.[156] In a *poor solvent*, the attractions between the segments dominate

and thus, the polymer chain collapses and the size of the chain is dramatically reduced.[156] When the attractions between segments cancel out the repulsions among the segments then the chains behave ideally and this is called a *theta system* (*theta solvent*), in which the dimensions of the chain are undisturbed.[162]

A schematic of the conformations of polymer chains in a good solvent as a function of concentration is shown in Figure 2.14. As the concentration of a polymer increases from a dilute regime, where the coils are separated, to a more concentrated regime, where the coils overlap, the coils pass through a region where they begin to overlap.[160]. This critical concentration between the dilute and the more concentrated (also called semi-dilute regime) is known as the *overlap threshold concentration*, c*, and can be calculated from the following equation:[135, 157]

$$c^* \approx \frac{3\,M_w}{4\,\pi\,N_A\,R_g^3} \tag{2.50}$$

where M_w is the molecular weight of the polymer, N_A is Avogadro number, and R_g is the radius of gyration of the polymer.

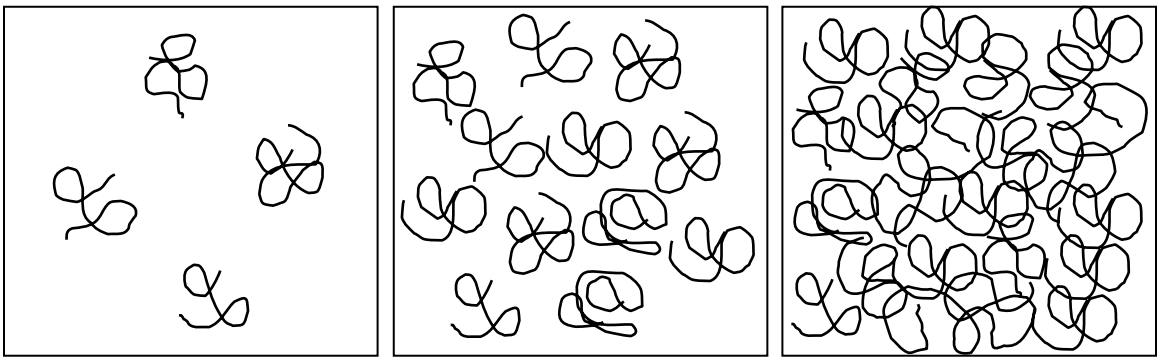

(a) C < C* (b) C = C* (c) C > C*

Figure 2.14: Schematic representation of (a) dilute, (b) overlap threshold, and (c) semi-dilute solutions

CHAPTER 3 LAPONITE-PEO HYDROGELS AT REST*

In this chapter the structure at rest of Laponite-PEO hydrogels with varying polymer molecular weight, is explored. Results obtained from static SANS and static USANS experiments that provide information on the structure of these hydrogels on multiple length scales are presented. Complimentary TEM and SEM images that provide direct visualization of the nano and micrometer structures, respectively, are also included.

3.1 Experimental Procedures

3.1.1 Sample Preparation

Laponite RD (LRD) was obtained from Southern Clay Products, Inc. Poly(ethylene oxide) (PEO) of molecular weights of 100, 300, 600 and 1000 kg/mol and a polydispersity (M_w/M_n) of ≈ 1.5, were purchased from Polysciences Inc. The solvent used was D_2O, which is preferred to H_2O in neutron scattering experiments. D_2O was also used for the rheological and microscopic experiments, to obtain results comparable to the neutron scattering experiments. Mixtures of D_2O and H_2O were only used for neutron scattering contrast matched experiments described in Chapter 5. To ensure chemical stability of the particles, the pH of the solutions was adjusted to be ≈ 10 by adding NaOH.[83, 101] At this pH value, the particles are negatively charged. To screen the electrostatic interactions between the negatively charged particles, the ionic strength of

* Reproduced in part with permission from *Macromolecules*, Loizou, E.; Butler, P.D.; Porcar, L.; Talmon, Y.; Kesselman, E.; Dundigalla, A.; Schmidt, G., Large-scale Structures in Nanocomposite Hydrogels, **2005**, 38, 2047-2049. Copyright 2005 American Chemical Society.

the solutions was adjusted by adding 10^{-3} mol/L NaCl.[96, 101] Unfortunately, a decrease of the pH of the samples was observed with time, most probably due to dissolution of CO_2 from the air. Gels whose pH dropped below 8 were discarded. Highly reproducible measurements were possible within a window of 3 months after sample preparation. The majority of the results reported in this work were obtained from gels containing mass fractions of 3 % LRD and 2 % PEO (abbreviated as LRD3-PEO2-Mw (in kg/mol)) at room temperature. The hydrogels were prepared by mixing the PEO and the Laponite powders together first, and then adding the solvent. During the initial stages of mixing, large clumps are formed. However, with extensive mixing and centrifuging for a period of 3 weeks, one can achieve complete dissolution of the polymer and Laponite clusters and obtain macroscopically homogeneous transparent hydrogels.

3.1.2 Neutron Scattering Measurements

Small angle neutron scattering measurements (SANS) were performed at the National Institute of Standards and Technology (NIST) Center for Neutron Research in Gaithersburg, MD using the 30 m SANS instrument (NG7).[163] Although a range of incident wavelengths, from 5 Å to 8 Å, was used, the majority of measurements were made with a wavelength of 8 Å. For each sample, data were gathered from either two or three sample-to-detector distances to provide information over the wide q range. The majority of measurements cover a q range of 0.0027 $Å^{-1}$ to 0.24 $Å^{-1}$. The scattering data from each sample were corrected for background noise, detector efficiency, empty cell scattering, and sample transmission using SANS-IGOR Pro Software provided by NIST.[164] Intensities were calculated to be on an absolute scale (cm^{-1}). The scattering

intensity I(q) as a function of the wave vector q was obtained by circularly averaging the isotropic SANS patterns.

Ultra small angle neutron scattering (USANS) measurements were also performed at the Center for Neutron Research at NIST, using the thermal neutron double-crystal diffractometer (BT5).[151] The neutron wavelength was 2.38 Å and the q-range covered was between 4×10^{-5} $Å^{-1}$ and 2.7×10^{-3} $Å^{-1}$. Scattering data were converted to absolute units, cm^{-1}, by subtracting the empty cell scattering and normalizing by the sample thickness. The slit-smeared intensity was numerically desmeared using the SANS-IGOR Pro Software provided by NIST.[164]

3.1.3 Electron Microscopy Measurements

Transmission Electron Microscopy (TEM) images were obtained for a representative polymer-clay gel that contains PEO of M_w = 1000 kg/mol. For such measurements the sample was prepared by the freeze fracture (FF) technique, and then coated with a carbon-platinum replica. TEM images were also obtained for a pure Laponite clay solution containing less than 0.1 wt % of clay. This solution was vitrified and imaged in the frozen state using Cryo-TEM. All the TEM images were obtained by Dr. Kesselman and Dr. Talmon at the Technion-Israel Institute of Technology.

Environmental Scanning Electron Microscopy (ESEM) images were also obtained for the representative LRD3-PEO2-Mw1000 sample. Images were taken with a FEI Quanta 200 Environmental SEM instrument that provides a controlled humidity sample environment. Careful attention was paid to minimize effects from solvent evaporation and condensation. All SEM samples were frozen in Freon (freezing point of -158 °C) to avoid ice crystal formation. The freeze fractured surfaces were imaged directly without

the use of replicas. The images were obtained 5 minutes after the sample was placed into the chamber. The ESEM images were obtained by Avinash Dundigalla.

3.2 Results and Discussion

3.2.1 Characteristics of Poly(ethylene oxide) in Solution

Characteristic parameters of the poly(ethylene oxide) samples used in this work are given in Table 3.1. These include the molecular weight, M_w, the radius of gyration, R_g, the hydrodynamic radius, R_h, and the overlap threshold concentration, c*, of each PEO sample dissolved in water at 25 ºC. The overlap threshold concentration (c*) was calculated according to equation 2.50 (section 2.6.4). The radius of gyration and the hydrodynamic radius were calculated from the empirical equations 3.1 and 3.2 suggested by Devanand *et al*.,[115] who performed dynamic light scattering experiments on aqueous solutions of PEO of different molecular weights.

$$R_g\,(\text{Å}) = 0.215 \times (M_w)^{0.583} \tag{3.1}$$

$$R_h\,(\text{Å}) = 0.145 \times (M_w)^{0.571} \tag{3.2}$$

Table 3.1: Characteristic parameters of PEO samples dissolved in water

Molecular Weight M_w (kg/mol)	Radius of Gyration R_g (Å)	Hydrodynamic Radius R_h (Å)	Threshold Concentration c* (w/v, %)
100	177	104	0.72
300	335	194	0.32
600	502	289	0.19
1000	677	387	0.13

The mass density of PEO was measured with the DMA 5000 density meter to be 0.84 g/cm^3. Taking into account its density, the neutron scattering length density of PEO (ρ_{PEO}) was calculated, using equation 2.27 as follows:

$$\rho_{PEO} = \frac{d\,N_A}{M_0}\sum_k^N b_k = \frac{d\,N_A}{M_w}\left(2b_C + 4b_H + b_O\right)$$

$$\rho_{PEO} = \frac{(0.84\times10^6\,g\cdot m^{-3})(6.022\times10^{23}\ mol^{-1})}{(44\,g\cdot mol^{-1})}\left[(2(6.646)+4(-3.741)+(5.803))\times10^{-15}\ m\right]$$

$$\rho_{PEO} = 4.75\times10^{13}\ m^{-2} = 0.475\times10^{-6}\ Å^{-2}$$

The contrast match point for PEO (which is the ratio of D_2O to H_2O where the average scattering length density of the mixed solvent exactly matched that of the PEO), can be calculated through its scattering length density according to equation 2.37 as follows:

$$\rho_{D_2O}\,\Phi_{D_2O} + \rho_{H_2O}\Phi_{H_2O} = \rho_{PEO}$$

$$(6.36\times10^{-6}\,Å^{-2})\,\Phi_{D_2O} + (-0.56\times10^{-6}\,Å^{-2})(1-\Phi_{D_2O}) = (0.475\times10^{-6}\ Å^{-2})$$

$$\Phi_{D_2O} = 15\ \text{vol}\%\ D_2O$$

To calculate the contrast match point for PEO experimentally, the contrast matched technique described in the section 2.2.6 was followed. The measurement gave a value for the contrast match point of 40 vol % D_2O, which is much larger than predicted. After contacting the supplier we found out that the batch of polymer had a very small amount of large-size impurities and this was the reason for the larger contrast match point observed. To remove the impurities, the PEO was dissolved and centrifuged for a few days. The impurities fell to the bottom of the vial and the supernatant was freeze-dried to

obtain a pure polymer powder. The measurement for the contrast match point was repeated and this result was ≈ 20 vol % D_2O. This value is a little bit higher that the theoretical one, implying that we may still have some impurities in the sample. To be safe, we prepared our PEO contrast matched samples with 17 vol % D_2O, a value in between the theoretical and the experimental one. At this match point, the sample is well contrast matched.

3.2.2 Characteristics of Laponite in Solution

Laponite RD has a chemical composition of $Na_{0.7}Mg_{5.5}Li_{0.3}Si_8O_{24}H_4$ and a density[134] of 2.65 g/cm^3. The theoretical neutron scattering length density of LRD (ρ_{LRD}) was calculated using equation 2.27 as follows:

$$\rho_{LRD} = \frac{d\,N_A}{M_0}\sum_k^N b_k = \frac{d\,N_A}{M_0}\left(0.7b_{Na} + 5.5b_{Mg} + 0.3b_{Li} + 8b_{Si} + 24b_O + 4b_H\right)$$

$$\rho_{LRD} = \frac{(2.65\times10^6\,g\cdot m^{-3})(6.022\times10^{23}\ mol^{-1})}{(762\,g\cdot mol^{-1})}\left[\begin{array}{l}(0.7(3.63)+5.5(5.375)+0.3(-1.9)\\+8(4.1491)+24(5.803)+4(-3.741))\times10^{-15}\ m\end{array}\right]$$

$$\rho_{LRD} = 3.96\times10^{14}\ m^{-2} = 3.96\times10^{-6}\ Å^{-2}$$

Through the theoretical scattering length density of Laponite, its contrast match point was calculated according to equation 2.37 and it was found to be around 65 vol % D_2O. The contrast match point of Laponite was also determined experimentally as described in section 2.2.6 and was found to be ≈ 70 vol % D_2O. From the experimental value of the contrast match point, the experimental neutron scattering length density of Laponite, (ρ'_{LRD}), was calculated using equation 2.37 as follows:

$$\rho_{D_2O}\,\Phi'_{D_2O} + \rho_{H_2O}\Phi'_{H_2O} = \rho'_{LRD}$$

$$(6.36\times10^{-6}\,\text{Å}^{-2})\,(69.8\,\text{vol}\,\%\,D_2O)+(-0.56\times10^{-6}\,\text{Å}^{-2})(31.1\,\text{vol}\,\%\,H_2O)=\rho'_{LRD}$$

$$\rho'_{LRD}=4.265\times10^{-6}\ \text{Å}^{-2}$$

A difference in the two values of the scattering length densities of Laponite is not surprising. The theoretical value was calculated based on an empirical molecular formula for Laponite reported by the supplier and not on a precise atomic composition measurement, of our batch. To prepare the Laponite contrast matched samples, the experimental value of ≈ 70 vol % D_2O was used as the contrast matched point.

To obtain information about the dimensions of the Laponite particles, SANS measurements were performed on a dilute Laponite dispersion, such that the intensity depends mainly on the form factor of the particle. The scattering profile from a dilute Laponite solution with concentration 0.7 wt % ($\Phi = 0.0029$) is shown in Figure 3.1. The data has been corrected for incoherent background (subtraction) to magnify the q dependence of the scattering intensity. In the q range 0.02 $Å^{-1} < q < 0.2$ $Å^{-1}$, the data show a clear q^{-2} dependency, which is indicative of a disc shape object. At q values lower than 0.01 $Å^{-1}$, a q independent plateau is observed, which is predicted from the form factor.

In this q regime that shows a plateau, the Guinier approximation (section 2.2.5) was used to determine the radius of gyration of the particle, and therefore the radius of the particle. The Guinier plot of ln(I) vs. q^2 for values of $qR_g < 1$ is shown in Figure 3.2. The radius of gyration was calculated from the slope of the Guinier plot (equation 2.34) and was found to be 100.40 ± 0.66 Å. The radius of thin discs is approximately equal to $\sqrt{2}$ times the radius of gyration (equation 2.48). Therefore, the radius of the Laponite particle is calculated through the Guinier plot to be around 142 Å.

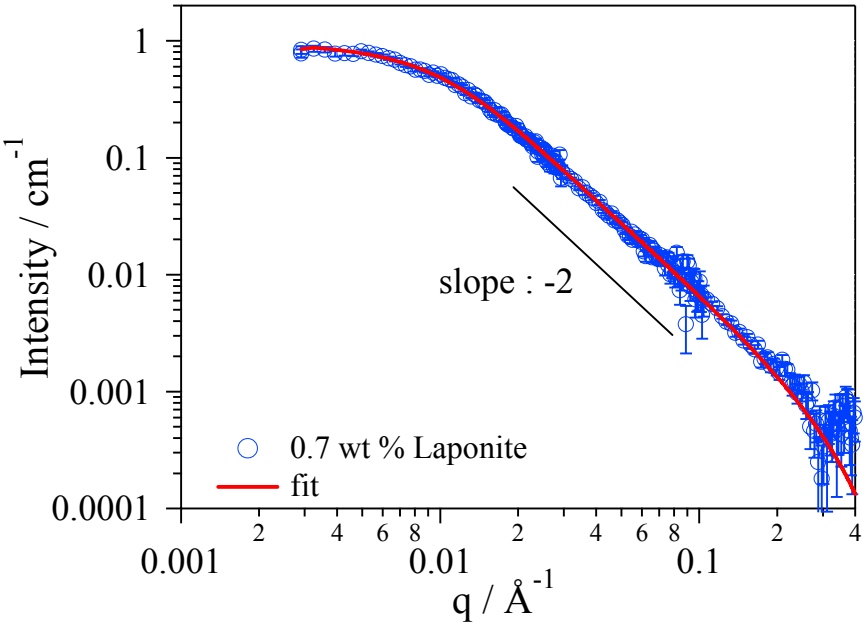

Figure 3.1: The scattering profile from a dilute Laponite dispersion with concentration 0.7 wt %, in D_2O. The data is fitted to a form factor for a disc with polydisperse radius

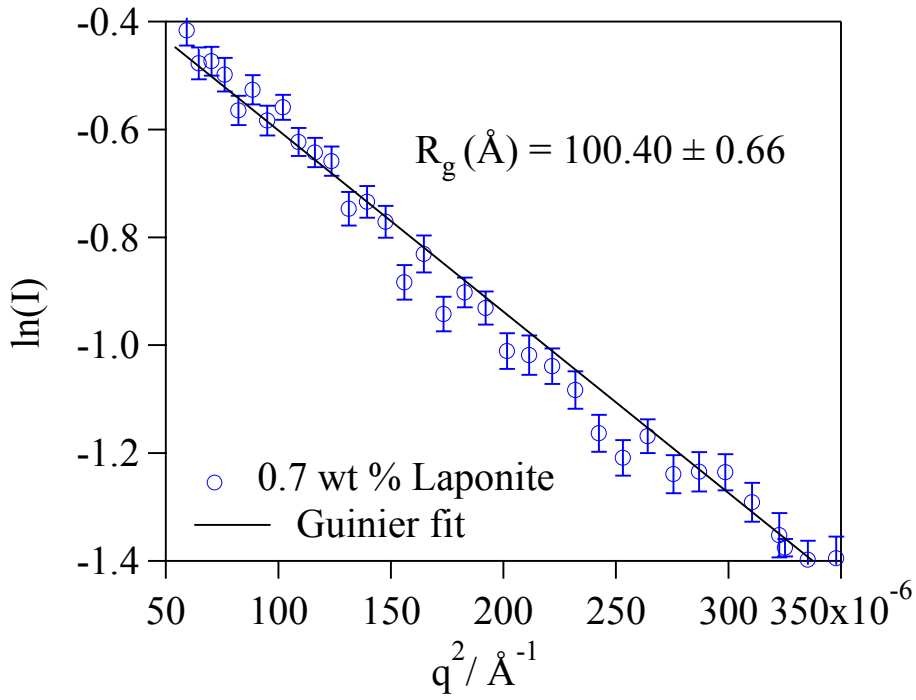

Figure 3.2: A Guinier plot for the 0.7 wt % Laponite dispersion in D_2O

In order to obtain further information about the particle dimensions, the scattering data were fitted to a model that is based on the form factor for a disc-shaped particle, which is given by the following equation:[46]

$$P(\vec{q}) = \int_0^{\pi/2} \left[\frac{\sin\left(\frac{1}{2} qH\cos\theta\right)}{\frac{1}{2} qH\cos\theta} \frac{2J_1(qR\sin\theta)}{qR\sin\theta} \right]^2 \sin\theta \, d\theta \qquad (3.3)$$

where H and R are the thickness and the radius of the disc, respectively. $J_1(x)$ is the first-order Bessel function, and θ is the angle between the normal to the face and the scattering wave vector q.

The fit is shown in Figure 3.1 and it seems to follow the data well over the entire q-range studied. The fit parameters are presented in Table 3.2. The values for the volume fraction and the scattering length density difference were known and were kept fixed during the fitting procedure. The mean radius of the particles was found to be 93.78 ± 3.52 Å, with a radial polydispersity of 0.56 ± 0.03 and a thickness of 9.01 ± 0.05 Å. The particle dimensions are similar to those presented in other studies.[41, 42, 74, 134]

Table 3.2: Fit parameters derived from the scattering of Laponite dispersion in D_2O

Parameter	**0.7 wt% Laponite**
Volume Fraction	0.0029
Particle Radius (Å)	93.78 ± 3.52
Particle Height (Å)	9.01 ± 0.05
Polydispersity of Radius	0.56 ± 0.03
Scattering Length Density Difference ($Å^{-2}$)	2.05×10^{-6}

The slight difference in the value of the radius obtained from the two methods, most probably is due to the type of average used in the calculations. The radius obtained

from the Guinier fit is a z-average, whereas the radius obtained from the form factor fit is a number average. Usually in a monodisperse sample the number, weight, and z-averages are fairly close. However, in a relatively polydisperse sample like this one, a difference in the number and z-averages is expected.

The dimensions of the clay platelets were also verified through cryo-TEM images from a very dilute pure clay solution embedded in vitreous ice. The cryo-TEM image is presented in Figure 3.3. The dark lines are clay platelets observed from the side, since diffraction contrast is strong enough only when the platelets are arranged with their normal surface parallel to the electron beam.[165] Platelets that have their basal plane perpendicular to the electron beam are not so obvious, because the contrast is not strong enough. Even though interpreting an image like this that averages over depth one should be careful, the clay particles are confirmed to have an average diameter of approximately 300 Å and an average thickness of approximately 10 Å.

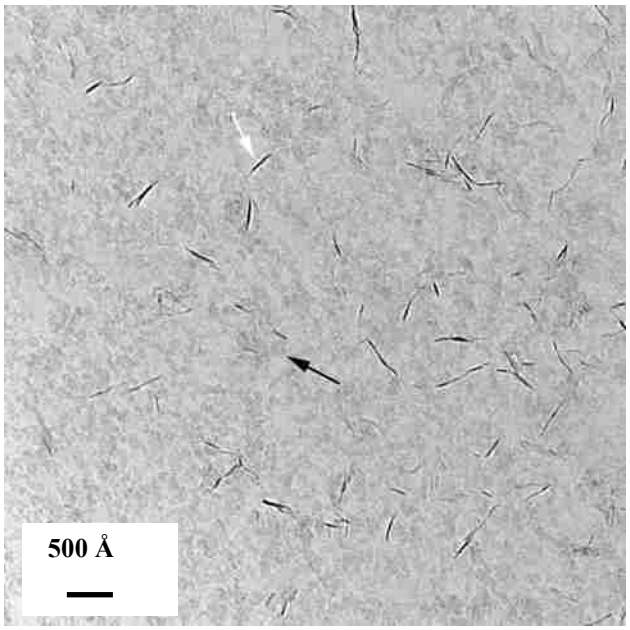

Figure 3.3: Cryo-TEM from a pure Laponite clay solution showing the thickness of single clay platelets visualized from the side. Arrows indicate single platelets

Based on the dimensions of the disc Laponite particle, (assuming an average diameter of 30 nm and an average thickness of 1 nm) and the bulk density of Laponite (2.65 g/cm^3), the specific surface area of Laponite was calculated to be around 800 m^2/g.

3.2.3 Interparticle Distance

In addition to the clay size, the average clay-clay interparticle distance is an important system parameter for understanding the structure and behavior of these LRD3-PEO2-Mw gels. A number of methods were proposed to calculate this distance. These are based on the on the assumption that the interparticle distance is the same in a pure Laponite gel and in a Laponite-PEO gel that have the same clay concentration. Some of these methods are presented below and applied to our system of 3 wt % clay.

Callaghan *et al.*[166] calculated the particle separation distance, d, using the expression below:

$$d = \frac{2V_s}{m_{clay}A_s} \tag{3.4}$$

where A_s is the specific surface area of the Laponite clay (A_s = 800 m^2/g), m_{clay} is the total mass of the clay, and V_s is the total volume of the solvent. This method assumes that the particles are arranged in continuous parallel sheets with no lateral separation between them, and that d is the distance between the parallel sheets. By applying the above equation to a 3 wt % clay sample (0.3 g of clay dissolved in 9.7 cm^3 solvent), a particle separation distance of d ≈ 80 nm can be calculated. This number will be an overestimation due to the assumptions of this expression. This method is usually applied to dispersions that have concentrations above 20 wt %, where small interparticle separations are observed.

An alternative method to determine the particle separation in a Laponite gel, is the one suggested by Kroon *et al*.,[80] in which the particles are considered equivalent spheres, such that the interparticle distance can be calculated from the number density of colloidal particles (N_d) as follows:

$$d = \left(\frac{1}{N_d} \right)^{1/3} \tag{3.5}$$

For the 3 wt % clay sample and assuming the particles have 30 nm diameter and 10 nm thickness, the number density is $N_d \approx 1.65 \times 10^{22}$ m^{-3}. This yields a particle separation distance of $d \approx 40$ nm. However, it should be noted that this number is extremely sensitive to the exact dimensions of the particles.

Schmidt *et al*.[43] calculated the clay-clay distance from SANS experiments performed on Laponite-polymer gels (where the clay concentration was kept constant at 3 wt % and the polymer concentration was varied). They found that the scattering profiles of the samples exhibit a shoulder at $q \approx 0.008$ $Å^{-1}$ that was attributed to the structure factor due to ordering between adjacent platelets. From this shoulder and using the equation $d = 2\pi/q$, a rough estimate of the average spacing between platelets can be made to be around $d \approx 80$ nm. This is probably an overestimation of the interparticle distance, since the contribution of the form factor was not removed.

Since all the methods presented contain a number of assumptions and as a result yield a value of the interparticle distance that might not be so accurate, we made a direct measurement using the SANS technique. SANS measurements were performed on a pure Laponite gel of 3 wt % concentration. This data is shown in Figure 3.4 and compared to the data from a non-interacting dilute Laponite solution of 0.5 wt %. Both curves show

that the scattering intensity follows a q^{-2} power-law decay at high q values, which is characteristic for randomly oriented thin discs.[80, 90, 167] The main difference between the two data sets is that the curve for the 3 wt % Laponite solution (where the structure factor is a significant contributor to the overall scattering at low q) exhibits a shoulder at $q \approx 0.013$ Å^{-1}. Using the equation $d = 2\pi/q$, we roughly estimate an interparticle-distance of 480 Å ($d \approx 48$ nm).

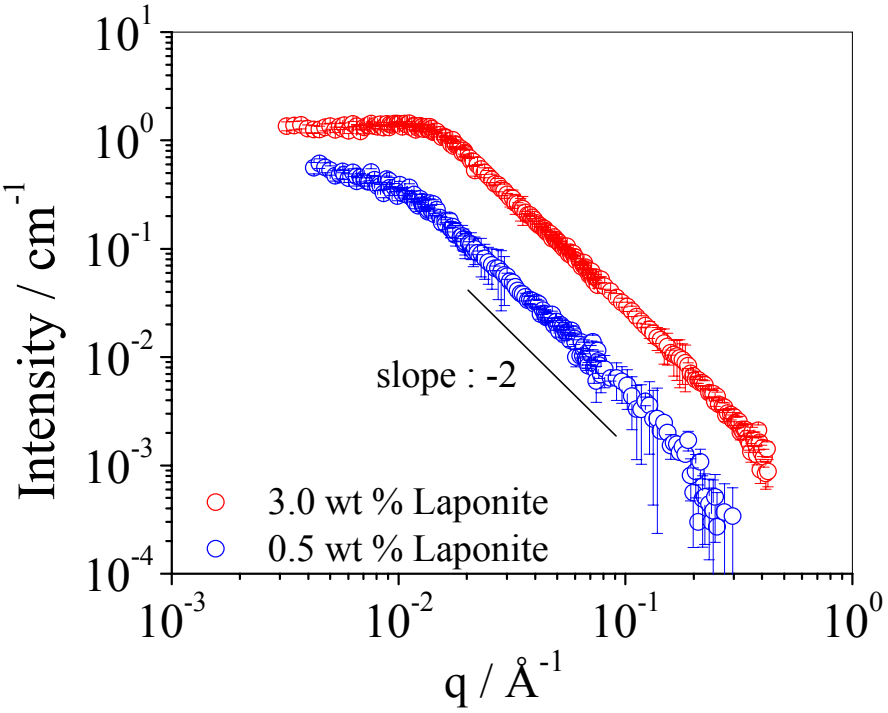

Figure 3.4: Scattering intensity as a function of q for 0.5 wt % and 3 wt % pure Laponite dispersions

A more exact value for the interparticle distance can be calculated from the peak position of the structure factor. The structure factor can be determined as described in section 2.2.4, where the scattering intensity from a concentrated dispersion ($I_{conc}(\vec{q})$), is divided by the scattering intensity from a dilute dispersion ($I_{dil}(\vec{q})$), and scaled by their

respective volume fractions (equation 2.32).[100] Figure 3.5 shows the experimental structure factor calculated from the ratio of the scattering curves of the concentrated 3 wt % ($\Phi_{conc} = 0.0127$) Laponite dispersion, to the dilute 0.5 wt % ($\Phi_{dil} = 0.0021$) Laponite dispersion. The structure factor curve shows a correlation peak. Despite the breadth of the peak and the relatively poor statistics, the peak position can be situated at $q \approx 0.018$ Å^{-1}. This corresponds to a clay-clay distance, ($d = 2\pi/q$), of $d \approx 350$ Å ($d \approx 35$ nm). This number is in good agreement with the averaged interparticle distance of 39 nm obtained by Kroon *et al*.[80] from SAXS data.

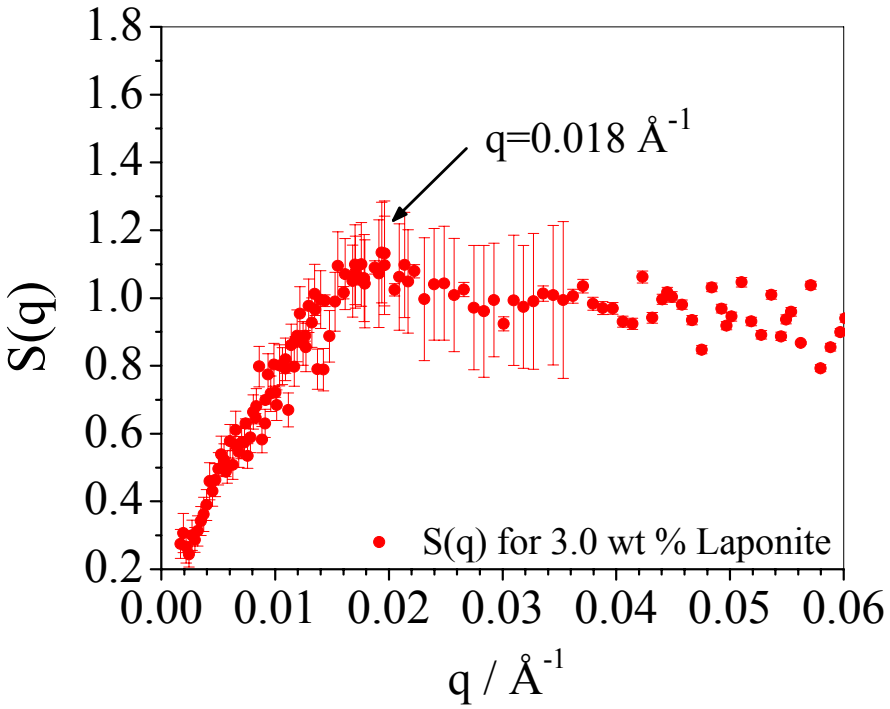

Figure 3.5: The structure factor, S(q) for a 3 wt % pure Laponite dispersion, calculated according to equation 2.32

In conclusion, it is clear that the assignment of the clay-clay interparticle distance is strongly dependant on the model used and the assumptions made for the calculations.

A range of values can be obtained. From our point of view, the method that uses the peak position of the structure factor has the fewer assumptions, and also gives a direct measurement. Therefore, for the purpose of this thesis we will accept the value of ≈ 35 nm as being the average clay-clay distance in a 3 wt % clay solution.

3.2.4 Saturation of Laponite Surface with PEO

Another important parameter for understanding the structure of Laponite-PEO gels is the amount of PEO absorbed onto the Laponite surface. Lal *et al*.[41, 42] and Nelson *et al*.[46-48] calculated this from data obtained by contrast variation SANS measurements. Lal *et al*.[41, 42] found values in the range of 0.59 mg/m^2 to 0.87 mg/m^2 with no systematic dependence on the polymer molecular weight. Nelson *et al*.[46-48] found similar values, between 0.53 mg/m^2 and 0.67 mg/m^2, but their data suggested a slight molecular weight dependence. The adsorption amount for each of the molecular weights used in this work was obtained from the paper of Nelson *et al*.[46-48]. This amount was found to be within errors at 0.65 ± 0.05 mg/m^2 for all the M_w studied. Based on the absorbed amount (0.65 mg/m^2) and the specific surface area of Laponite (800 m^2/g), the fraction of PEO that is bound on the Laponite platelets can be calculated. Thus, for a Laponite-PEO system that contains 3 wt % clay, the bound fraction of PEO segments on the clay platelets is estimated to be ≈ 1.56 wt %. Since our systems contain 2 wt % PEO, it is expected that at equilibrium the clay surface is completely covered by the PEO segments and that there is also approximately 0.44 wt % free PEO that is not adsorbed onto the clay surface.

It should be noted once again here that the value reported for the surface area is not based on any direct measurement, but is calculated from the dimensions of the particle, and as a result this value is extremely sensitive to the exact dimensions and

polydispersity of the particles. Nonetheless, even for the highest reported values of the surface area, the amount of adsorbed polymer is still less than 2 wt %, leaving some excess polymer that is not bound to the clay. The presence of excess PEO is expected to influence the "at rest" structure, as well as to stabilize the structure under shear. As an example, in the absence of excess polymer, poly(ethylene oxide)-Laponite samples have been found to phase separate under shear.[43]

3.2.5 Laponite-PEO Hydrogels

Our current understanding of previous results reported by Schmidt *et al*.[43-45] from a representative LRD3-PEO2-Mw1000 sample is that the polymer chains are in a dynamic adsorption-desorption equilibrium with the clay particles. Since there is more than enough polymer available to cover all the clay platelets, we expect the diffuse polymer chains to bridge neighboring clay particles and influence the structure, if they are long enough. In order to explore the effects of polymer length on the structure, gels with the same polymer and clay concentration but different molecular weights of PEO were prepared. To study the structure at rest on multiple length scales, small and ultra-small angle neutron scattering experiments were performed. In addition, complimentary environmental-scanning and transmission electron microscopy images, which were obtained to provide a direct visualization of the structures, are presented here.

SANS data obtained from gels containing 3 wt % LRD and 2 wt % PEO (LRD3-PEO2-Mw) of several different molecular weights (M_w) are shown in Figure 3.6. In the q regime between 0.0027 $Å^{-1}$ and 0.24 $Å^{-1}$, which probes length-scales up to slightly larger than the size of an individual disc, the data clearly show a complete lack of M_w dependence. This is consistent with (i) the findings of Lal *et al*.[41, 42] and Nelson *et al*.,[46]

who found that the adsorbed polymer layer thickness is independent of molecular weight, and (ii) the fact that the scattering intensity from a polymer network above c* is also independent of molecular weight. At high q values, the scattering intensity drops with a slope of -2.2 (i.e. a $q^{-2.2}$ dependence). The slight deviation from -2 slope that was expected for disc-like structures, is not surprising given that the free polymer coils must also contribute to the scattering in this regime.[80, 90, 167] From a Guinier fit to the low q data, an "apparent" R_g of ≈ 10 nm can be obtained. This R_g is consistent with the R_g of 10 nm obtained in section 3.2.2 for thin discs with 30 nm diameter and 1 nm thickness. However, attempts to fit the full curve to a core-shell model similar to what Nelson *et al*.[46] did for dilute systems (0.5 w/v % LRD and 0.35 w/v % PEO) failed, probably due to the higher concentrations used here and the excess free polymer in the solution.

In order to cover a wide range of length scales and elucidate the macroscopic structures within the system, SANS measurements were accompanied by USANS measurements that probe structural information at length scales up to several microns. Smeared USANS data in the q range from 4 x 10^{-5} $Å^{-1}$ to 2.7 x 10^{-3} $Å^{-1}$, obtained from the same polymer-clay gels which contain polymer of different molecular weights, are shown in Figure 3.7. At the very low values of q observed with USANS, the scattering intensity decreases with a slope of -1.5 ± 0.2 confirming the existence of a network-type large structure. The existence of these larger scale structures in the polymer-clay hydrogels is not surprising given that we have a polymer-coated clay network. Furthermore, the USANS profiles for all the samples overlap, revealing that the size of this network is not dependent on the polymer molecular weight.

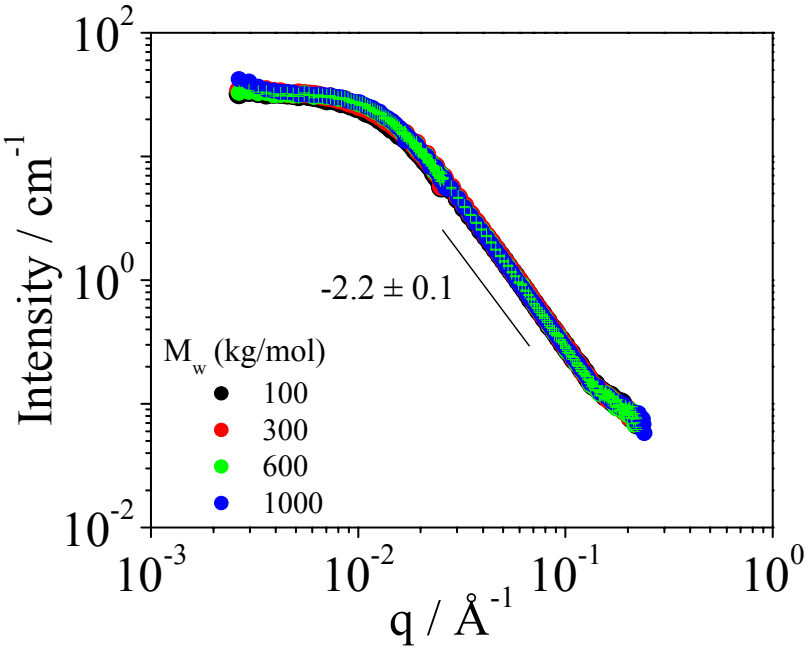

Figure 3.6: SANS scattering intensity as a function of q from the LRD3-PEO2-Mw hydrogels for several different molecular weights

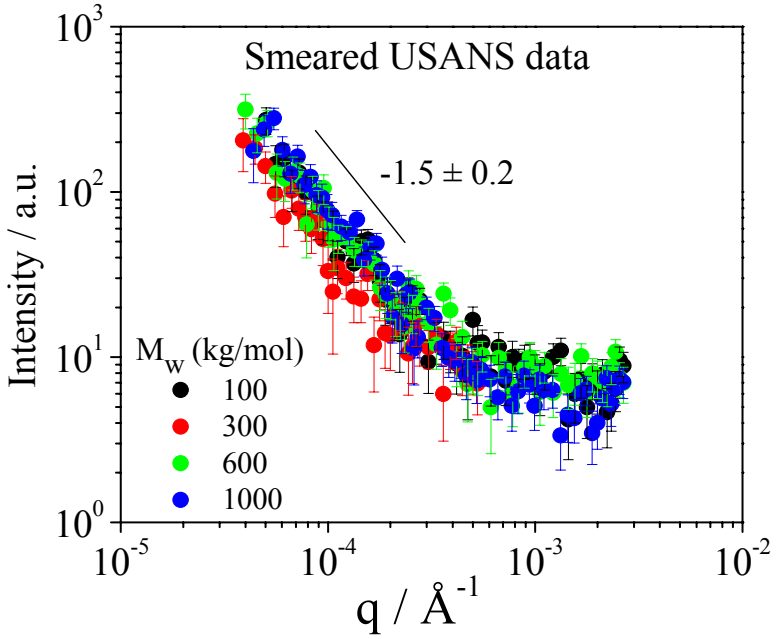

Figure 3.7: Measured smeared USANS data from the LRD3-PEO2-Mw hydrogels

The slit-smeared USANS data can be directly compared to the SANS data obtained from a pin-hole collimation. This is done by desmearing the USANS data to obtain scattering intensities on an absolute scale (cm^{-1}). The combined SANS and (desmeared) USANS intensity profiles cover four orders of magnitude in q from 4×10^{-5} $Å^{-1}$ to 0.24 $Å^{-1}$. The data is shown in Figure 3.8 for all the molecular weight polymer-clay hydrogels. The intermediate q region where the USANS and SANS data merge, shows a plateau of the scattering intensity. A similar behavior was seen in pure Laponite dispersions[46, 80, 167] at concentrations above the gel transition (see also section 3.2.3). For these systems, it was demonstrated that the plateau region (slope of zero) includes a structure factor due to ordering between adjacent platelets. Here the plateau region is likely a convolution of the disc form factor (or network form factor) with the structure factor of the polymer-clay network. In order to obtain the structure factor, it is necessary to divide out the form factor similar to what was done in section 3.2.3 for the pure Laponite solution. However, this is not trivial for the hydrogels due to the presence of excess polymer.

The scattering observed at very low q (in Figure 3.8) arises from large-scale inhomogeneities in the system, most likely caused by spatial variations in the concentration of polymer-coated platelets. For example, the existence of clay-rich areas separated by less dense (clay-poor) regions.[92] In this q region, the intensity scales with $q^{-2.5}$ (note the desmearing changed the slope). Even though the scaling covers only 2 orders of magnitude of q, an interpretation in terms of a "fractal" structure with a fractal dimension of 2.5 could possibly be made. This value of the fractal dimension suggests that the polymer-clay system forms a relatively dense network. This is similar to what

was proposed for pure Laponite systems. Light scattering experiments by Kroon *et al.*[80, 90, 91] on such pure clay systems also yielded a fractal-like structure with a fractal dimension that evolved from 2.8 to 2.1 during the gelation process. Investigations by Pignon *et al.*[92, 93] also suggested the existence of a fractal-like structure with a fractal dimension of 3 that was correlated to length scale of the order of few μm in size.

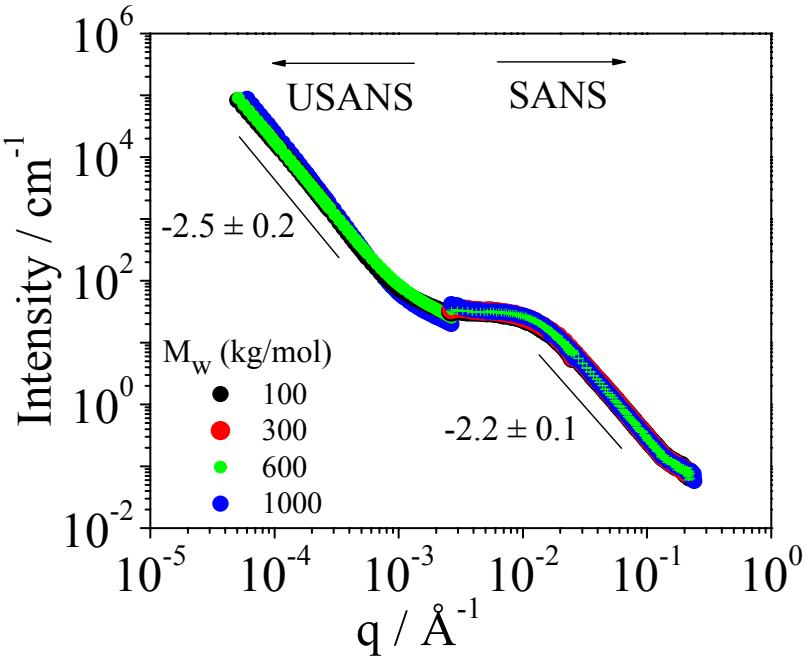

Figure 3.8: Combined together SANS and desmeared-USANS profiles from the LRD3-PEO2-Mw hydrogels at rest

To directly visualize of the nano and micro length-scale structures transmission and scanning electron microscopy were used. Figure 3.9 shows Freeze Fracture TEM images from a polymer-clay hydrogel with M_w = 1000 kg/mol, at two different scales. The images reveal a network-like structure that is characterized by an extremely fine texture of interconnected thin strings. The mesh size of the network is between 35 nm and

50 nm. This is in good agreement with the results obtained for the clay-clay interparticle distance from SANS measurements. The thickness of these strings is ≈ 4 nm while the thickness of a single clay platelet is ≈ 1 nm. Interpreting the lines in Figure 3.9 as polymer coated platelets viewed from the side leads to an adsorbed layer thickness of ≈ 1.5 nm on each side, which is in perfect agreement with the values obtained from dilute solutions below the gel transition.[41, 42, 46]

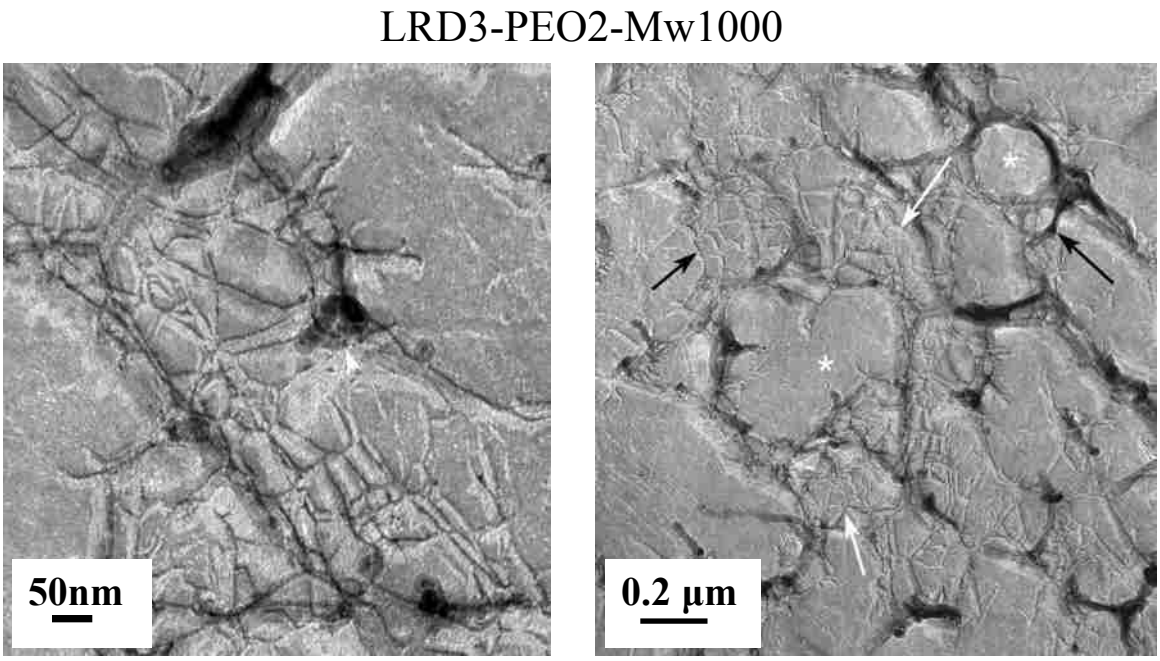

Figure 3.9: Freeze fracture TEM images from the polymer-clay hydrogel with polymer $M_w = 1000$ kg/mol, showing a network like structure on a nanometer length scale. Arrows point to areas with network-like structure and white asterisks indicate smooth areas.

One should take care to overcome the natural tendency to over interpret real space images. For example in these freeze fracture images we cannot see any platelets which do not happen to be sitting normal to the fracture plane, nor can we easily tell at what depth the observed platelets are. However, we may cautiously note that the platelets seem to lie within a network area (area with interconnected lines) adjacent to areas with no platelets

(smooth areas). An interpretation of this would be that at these length scales the polymer coated platelets form a relatively tight network with hundreds of nanometer pockets of solution. Figure 3.9 also provides evidence that the clay platelets can interconnect by network-active polymer through their edges, with many strings being much longer than the 30 nm nominal platelet diameter.

Although all samples are completely transparent to the eye and to optical microscopy, as are multilayered nanocomposite films made from the same polymer and clay components,[60] structures can be observed on a micron length scale using Environmental Scanning Electron Microscopy (ESEM). Optical transparency of samples with micron size texture is usually possible when refractive index matching of the large-scale structures with the surrounding solution is present. SEM, on the other hand, "sees" by reflection from the electron density and thus will clearly show areas of high electron density form the clay as bright areas, while the low, and nearly equal electron density (H_2O and H_2C are fairly similar in density), will show up as darker regions (LRD contains many electron rich atoms).

A representative SEM image from a freeze fractured surface of a polymer-clay hydrogel with polymer M_w = 1000 kg/mol is shown in Figure 3.10. The SEM image reveals an exquisite, lacey, sponge like texture on a micron length scale with on average 5 μm large clay-poor regions (dark areas) and ≈ 1.5 μm thick interconnected membranes of clay-rich areas (bright lines). Several areas show fine network structures within the 5 μm size pores. Assuming the TEM interpretation is correct, this network like structure on the micron length scale, is self similar to that on the nanometer length scale observed by TEM (Figure 3.9). Data obtained from a Fourier transformation of the real-space SEM

image, reveal a fractal dimension of 1.5, suggesting that at these length scales the polymer-clay network forms a much more open fractal-like structure. Therefore, the micrometer-sized relatively dense network observed with USANS, must be more loosely aggregated to form a much more open fractal-like structure at larger length scales (as those observed with SEM). This is in good agreement with the two characteristic length scales observed by Pignon *et al*.[92, 93] on pure Laponite dispersions. The authors suggested the existence of a fractal-like structure that was correlated with two characteristic length scales. The first length scale of the order of few μm was linked to a fractal dimension of 3, and the second one for sizes bigger than 10 μm was linked to a fractal dimension that increases from 1 to 1.8 with the particle volume fraction.

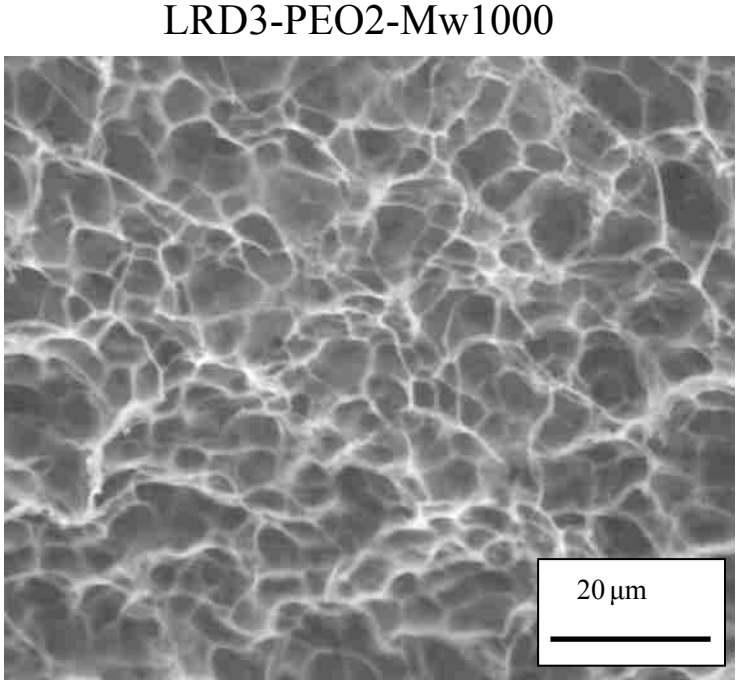

Figure 3.10: A representative SEM image from a freeze fractured surface of a polymer-clay hydrogel with polymer M_w = 1000 kg/mol, showing the network-like structure on a micron length scale

3.3 Conclusions

A combination of small and ultra-small angle neutron scattering, as well as microscopic techniques was used to describe and correlate microscopic and nanoscopic structures present in Laponite-PEO hydrogels. In these gels, the polymer and clay concentrations were kept constant, but the molecular weight of PEO was varied, in order to explore the effects of polymer length on the structure. The picture that begins to emerge for these gels is one in which clay platelets covered by a polymer coating of 1.5 nm thickness, are tethered together in fibrous bundles that form a fractal-like network structure from the nano up to the micron regime. This network structure is completely independent of the polymer molecular weight. This is not surprising for these gels that are above the overlap concentration and the only two differences between the samples are the mesh nodes per molecule and whether one molecule bridges all the way between two platelets. Those differences are not expected to influence the structure at rest, however, are expected to have an effect on the dynamics and therefore the structure under shear.

CHAPTER 4 RHEOLOGY OF LAPONITE-PEO HYDROGELS[†]

In this chapter, a comprehensive rheological characterization of the different polymer molecular weight hydrogels is presented. The flow behavior of these polymer-clay nanocomposite gels was studied by measuring the steady-state viscosities as a function of shear rate. The viscoelastic properties of the gels at low deformations and low frequencies were also tested through oscillatory shear experiments. Finally, results from constant stress (creep) experiments are presented.

4.1 Experimental Procedures

4.1.1 Sample Preparation

Samples for the rheological experiments containing 3 wt % Laponite and 2 wt % PEO, were also prepared in D_2O. The solutions had a pH ≈ 10 and a sodium chloride concentration of 10^{-3} mol/L. The samples were prepared in the same way as described in section 3.1.1.

4.1.2 Flow Experiments

Rheological flow measurements were performed on a Rheometric Scientific ARES strain-controlled rheometer (TA Instruments Ltd). Measurements were obtained using a parallel plate configuration with 38 mm diameter plates and 1mm gap. The steady state viscosity for each shear rate was obtained by performing individual, time-

[†] Reproduced in part with permission from *Macromolecules*, Loizou, E.; Butler, P. D.; Porcar, L.; Schmidt, G., Dynamic Responses in Nanocomposite Hydrogels, **2006**, 39, 1614-1619. Copyright 2006 American Chemical Society.

dependent, constant-shear rate experiments. Once the samples equilibrated to a steady state viscosity, the viscosity was recorded, and another time-dependent constant-shear rate experiment was performed. In order to achieve steady-state, constant shear rates had to be applied for times ranging from ≈ 5000 s at the lowest shear rates down to ≈ 20 s at the highest shear rates. Solvent evaporation was prevented by coating the sample with a thin layer of silicon oil. The effect of the silicon oil on the overall rheological behavior was measured and was found to be negligible. To check for reproducibility of results, duplicate measurements were taken with a new sample. Steady state values were reproduced within a relative uncertainty of < 9 %.

4.1.3 Oscillatory Experiments

Oscillatory experiments were also performed on the ARES strain-controlled rheometer using the parallel plate geometry. For these experiments, a sinusoidal strain was applied to the sample and the response stress was computed from a torque transducer connected to the stator. The elastic (G') and viscous (G'') moduli were measured as a function of frequency and as a function of strain. Frequency sweep tests were performed by keeping the amplitude of applied strain constant at γ = 1 %. Strain sweep tests were performed by keeping the frequency of oscillations constant at ω = 1 Hz. Duplicate measurements with a new sample showed reproducibility of moduli values within a relative uncertainty of 15 % for the low M_w gel and less than 7 % for all other gels.

4.1.4 Creep Experiments

Creep experiments were performed on the Advanced 1000 stress-controlled rheometer (TA Instruments Ltd). Measurements were obtained using a parallel plate configuration with 40 mm diameter plates and 1 mm gap. A constant stress of τ = 2 Pa

was applied on the samples for 5000 s and the response deformation (strain) was recorded. To record the recovery of the samples, a stress of 0 Pa was programmed for an additional 5000 s. For two representatives polymer-clay gels, with M_w = 300 kg/mol and M_w = 1000 kg/mol, a series of constant stress experiments was performed with applied stresses of τ = 1, 2, 5, 20, 500, and 1500 Pa. When the applied stress was changed, a new sample was employed in order to avoid remnant shear effects. To minimize the effects of any shear associated with loading the samples, experiments were performed 15 min after loading. To prevent solvent evaporation, a solvent trap was used.

4.2 Results and Discussions

4.2.1 Flow Experiments

The steady state viscosity (η) as a function of shear rate ($d\gamma/dt$) for the LRD3-PEO2-Mw100, 300, 600, and 1000 gels are shown in Figure 4.1. All the gels show a shear thinning behavior over a large range of applied shear rates. The double logarithmic plot, exhibits a near power law behavior. The data was fitted to the power law $\eta = K(d\gamma/dt)^m$ and the power law exponents (m) were calculated form the slope. Values vary between m = 0.6 for the high molecular weight sample to m = 0.9 for the low molecular weight sample. Deviations from linearity are observed at the highest shear rates and are a result of normal forces that push the sample out of the shear cell.

At low shear rates (0.01 s^{-1} - 0.5 s^{-1}), the viscosity shows a weak dependence on the M_w, with all the gels having approximately the same viscosity at the lowest measured shear rate. Therefore, these polymer-clay gels cannot be compared with simple polymer solutions, where a distinct M_w dependence of the viscosity is observed at the lowest

measured shear rates.[168] At higher shear rates (10 s^{-1} - 500 s^{-1}), there is a strong dependence of the viscosity on the polymer M_w, the higher the M_w of the sample the higher the viscosity. These results are consistent with our earlier hypothesis that the polymer chains are in a dynamic absorption-desorption equilibrium with the clay particles. At low shear rates, the mechanical coupling between clay platelets and long polymer chains has only marginal consequences on the flow properties. As the shear rate increases, any polymer-clay interactions become increasingly important. This is reflected first in the steady state viscosity, which increases for a given shear rate in the series LRD3-PEO2-Mw100, 300, 600, and 1000 and second in the microstructural orientation which will be discussed later in section 5.2.

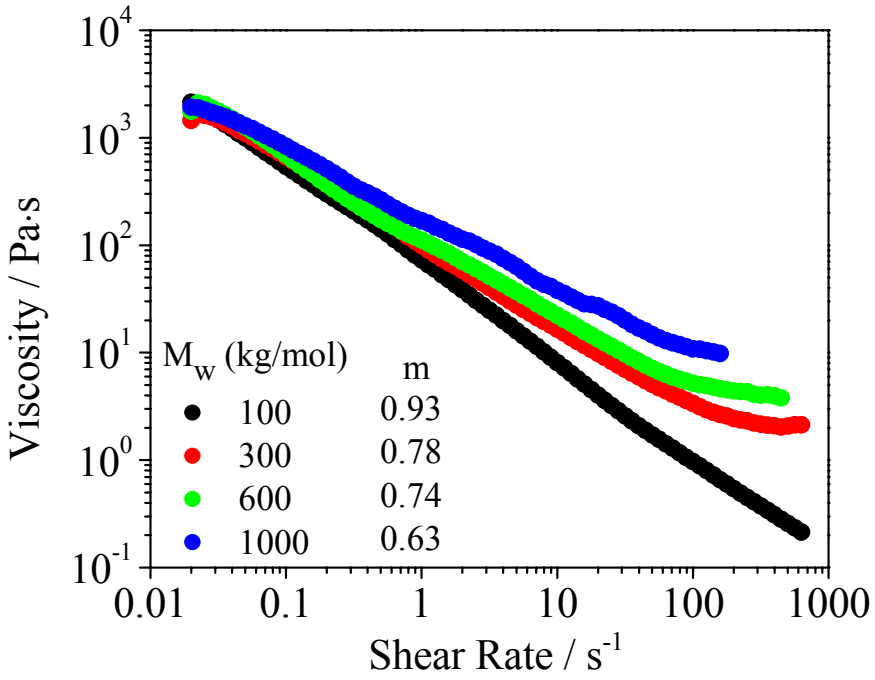

Figure 4.1: Steady state viscosity (η) as a function of shear rate (dγ/dt), for the LRD3-PEO2-Mw series. Power law exponents (m) obtained via $\eta = K(d\gamma/dt)^m$ are shown. Experiments can be reproduced with a new sample with a relative uncertainty of < 9 %

Usually, solutions containing anisotropic particles shear thin by alignment of the particles with the flow, allowing them to slide past each other more easily. However, in connected gels, like those studied here, breaking the connectivity would also lead to shear thinning. The fact that at high shear rates, the high M_w samples are more viscous, suggests the presence of more interactions between the network active long polymer chains and the clay particles. Many interconnecting polymer chains (such as for the LRD3-PEO2-Mw1000 sample) will immobilize the micro-structure more than a few interconnecting chains or no connecting chains (such as for the LRD3-PEO2-Mw100 sample). Therefore, the high M_w samples will produce a more rigid network that will exhibit higher resistance to flow.

4.2.2 Oscillatory Experiments

In order to test the viscoelastic properties at low deformations, frequency dependent oscillatory shear experiments were performed. Results for the LRD3-PEO2-Mw series are shown in Figure 4.2. At a constant strain of 1 % the data are well within a relatively broad linear viscoelastic range. For all the gels the storage modulus, G', is always larger than the loss modulus, G", indicating that the gels behave mostly like elastic solids within the frequency range studied. The LRD3-PEO2-Mw100 exhibits similar rheological characteristics to that of a pure 3 wt % LRD gel, with a storage modulus that is frequency independent.[70, 71] For all other (higher) M_w samples, the storage modulus displays some dependence on frequency, with the storage modulus increasing with frequency and polymer molecular weight. This may be related to the formation of a transient network in which the clay platelets are "bridged" by the PEO. At the lower frequencies, the LRD3-PEO2-Mw100 sample appears to have a slightly higher

elastic modulus than the other gels; however, the relative uncertainty on the moduli of the LRD3-PEO2-Mw100 sample is ≈ 15 % while that of the moduli for the other gels is less than 7 %.

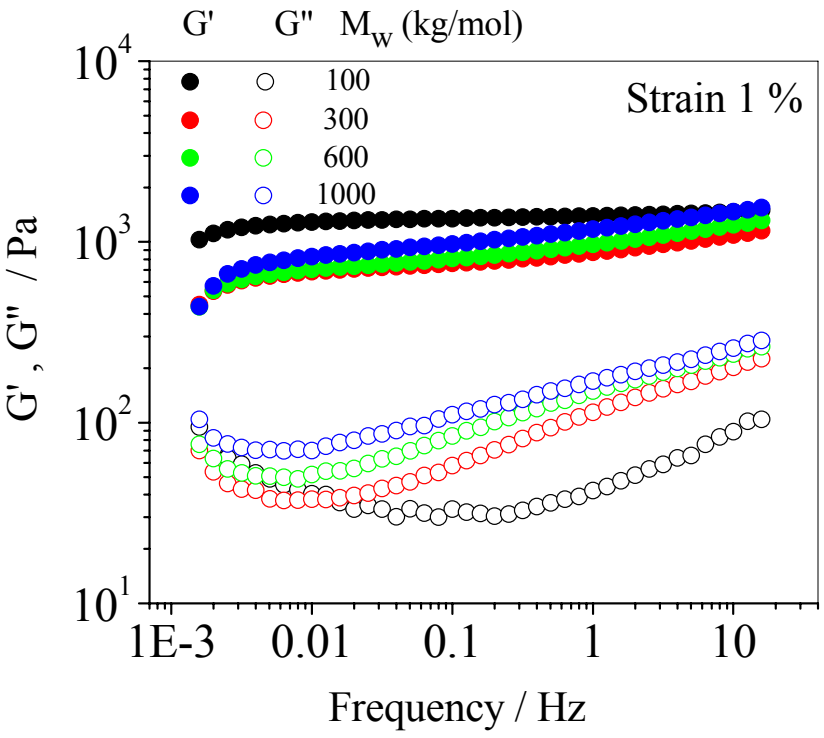

Figure 4.2: Frequency dependence of G' (full symbols) and G" (open symbols) for the polymer-clay gels

The loss moduli, G", for all samples exhibit a minimum, G''_{min}, resulting from the increase in G" at both low and high frequencies. This rise of G" at low frequencies implies the existence of a relaxation process resulting from very slow structural rearrangements of the micro-domains within the gels. The increase of G" at high frequencies reflects the domination of the viscous relaxation of the fluid phase, at frequencies higher than those measured.[169] When the molecular weight of PEO in the gels

is increased from 100 kg/mol to 300 kg/mol, the minimum in G" shifts to a significantly lower frequency. As the molecular weight of PEO is further increased, the frequency at which the G''_{min} is found slowly shifts to lower values. This shift most likely is due to an increase of the high frequency mode of G", indicating that viscous relaxation becomes increasingly dominant at the higher frequencies as the polymer molecular weight increases. At these low deformations of 1 %, the flow history does not change the equilibrium structure of the gel at rest and all experiments were reproducible.

In order to test the viscoelastic properties of these polymer-clay gels at a series of deformations, strain dependent oscillatory shear experiments were performed. Results for the LRD3-PEO2-Mw series are shown Figure 4.3. The frequency of oscillation was kept constant for all experiments at ω = 1 Hz. At low deformations (strain < 10 %), the elastic modulus, G', for all the gels is constant and its values are always larger than values for the loss modulus, G". Thus, at sufficiently small strains, the gels behave like elastic solids. The samples with M_w = 300, 600, and 1000 kg/mol display elastic moduli, which increase with M_w. In contrast, the LRD3-PEO2-Mw100 sample does not follow that trend. Thus, the elasticity of the high M_w samples arises most probably from the ability of the sample to form a network in which the clay platelets are "bridged" by the polymer chains. The elasticity of the low M_w sample, which is not expected to be able to bridge, could be arising from the clay network itself.

As the deformations increases above 10 %, the elastic modulus decreases dramatically for all gels. The gels start to flow with the LRD3-PEO2-Mw100 gel flowing first and the LRD3-PEO2-Mw1000 flowing last. At really high deformations (~ 100 %), the viscous modulus, G", initially rises and then quickly falls. In all the cases however,

the value of G" crosses over that of G', making the samples behave more like viscous fluids than elastic solids at these high deformations. The fact that the G" dominates at high deformations, reflects the increased loss due to large-scale rearrangements or flow of the micro-domains as the strain increases above the yield value.[169] These micro-domain rearrangements will occur more easily in a non-connecting gel like the LRD3-PEO2-Mw100 gel, rather than in a gel that has more interconnections and can display more resistance to flow.

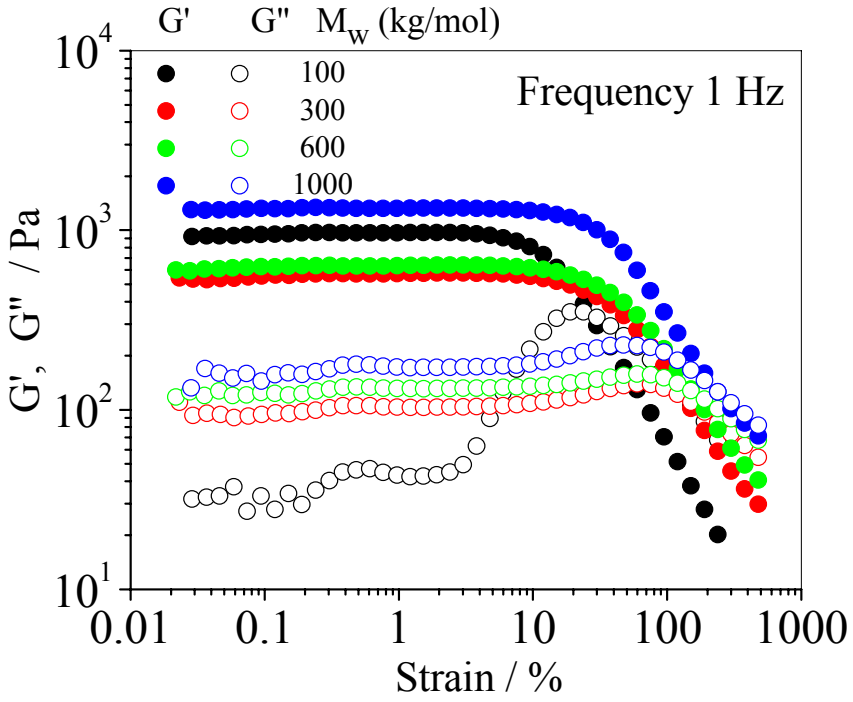

Figure 4.3: Strain dependence of G' (full symbols) and G" (open symbols) for the polymer-clay gels

4.2.3 Creep Experiments

In order to complete the rheological characterization of these polymer-clay gels and probe the mechanical properties of the system, constant stress (creep) experiments

were performed. A constant stress of 2 Pa was applied to the samples for 5000 s and the resulting deformation (= strain) was recorded as a function of time. After cessation of shear, the strain recovery was recorded for an additional 5000 s (Figure 4.4).

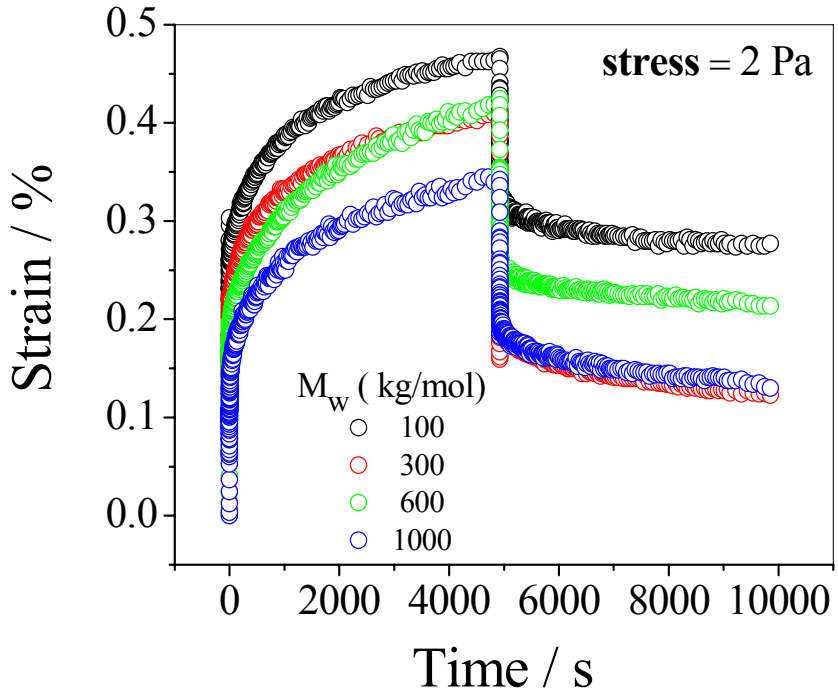

Figure 4.4: Time dependence of the resulting strain of creep experiments performed at a constant stress of 2 Pa on different M_w samples. Shear was applied for 5000 s, then stopped and data collected for an additional 5000s

As can be seen from Figure 4.4, the data shows that at this low stress of 2 Pa, all the polymer-clay gels continue to deform with time. The sample with the lowest M_w exhibits the highest deformation. This can be attributed to the existence of non-connecting micro-domains that can slide past each other and easily rearrange in the low M_w gel, compared to the interconnected micro-domains that exist in the higher M_w gels. In fact, the gel with M_w = 1000 kg/mol exhibits less deformation than the other gels,

since in that gel the number of interconnections is higher and therefore the micro-domains display more resistance to flow.

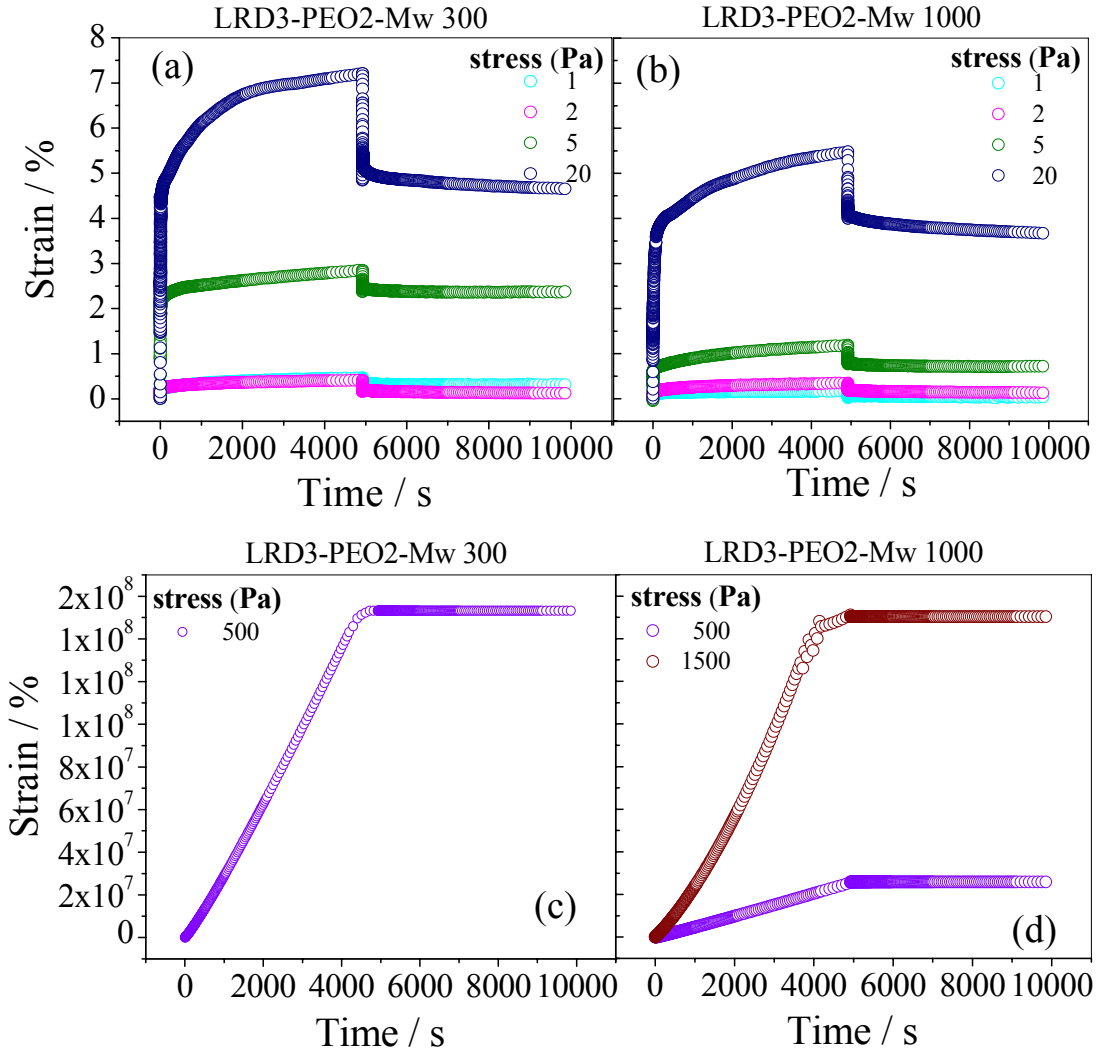

Figure 4.5: Results from creep experiments of a series of low (a and b) and high (c and d) stresses for the LRD3-PEO2-Mw300 (a and c) and the LRD3-PEO2-Mw1000 (b and d) hydrogels

After cessation of shear (Figure 4.4), all the samples show only partial recovery of the strain. There is no evidence of complete recovery, even after 5000 s. Moreover, at the recovery part there is no visible asymptotic plateau at long times. This behavior was also

observed in pure Laponite dispersions of 3 wt % and is indicative of a viscoelastic behavior having slow or very slow relaxation mechanisms.[84]

The effect of stress was studied by performing a series of constant stress experiments at values of τ 1, 2, 5, 20, 500, and 1500 Pa, for two representative molecular weights, 300 kg/mol and 1000 kg/mol, gels. The results are shown in Figure 4.5. At low applied stresses, up to 20 Pa (Figures 4.5 a and b), the hydrogels behave like viscoelastic materials since there is a partial recovery of the strain after cessation of shear. As the applied stress increases (Figures 4.5 c and d), the hydrogels behave more like a viscous fluid, where a steady rate of strain is observed with no recovery of the strain after cessation of shear. Comparing the data from the two hydrogels it is clear that at a given stress the deformation of the LRD3-PEO2-Mw1000 sample is always lower than that of the LRD3-PEO2-Mw300 sample. This most probably is due to the higher interconnectivity between long polymer chains and Laponite cross-links that exist in the high M_w samples, making them more elastic and thus more resistant to deformation.

4.3 Conclusions

At a constant composition by mass and only changing polymer M_w the total contour length of the linear chains in solution stays constant. What is changing is the interconnectivity between the polymer and the clay. One long string versus hundreds of shorter ones means the number of points with relatively infinite degrees of freedom increases. This increased freedom does not significantly influence the viscoelastic range observed at small deformations (Figure 4.2) and small frequencies (Figure 4.3) but changes the dynamics at high deformations where interconnectedness or cross-linking becomes important (Figure 4.1).

Based on the similarities of the structures of all the samples at rest (Chapter 3), and also of the identical viscosities at very low shear-rates, it seems that all the gels contain micron-size polymer-clay domains that look alike when at rest and do not depend on the M_w of the polymer. Under shear though, the polymer length becomes important as these micro-domains are interconnected and cannot easily rearrange.

CHAPTER 5 LAPONITE-PEO HYDROGELS MONITORED BY SHEAR-SANS[‡]

In this chapter, the unique flow properties exhibited by these complex fluids are correlated with their structural deformation through SANS experiments performed under shear. The effect of molecular weight, polymer and clay concentrations, as well as preparation method on the shear-induced structures, were explored. Some of these were complemented by experiments in contrast matched solvents, to elucidate the shear response of individual components.

5.1 Experimental Procedures

In order to study the behavior of these systems in the three directions in space, scattering measurements are typically carried out in the two geometries discussed in section 2.3. Tangential geometry data require much longer counting times because the sample area is much reduced, and the effective thickness is much increased which leads to significant transmission losses. Furthermore, the tangential geometry data has complicated contributions from reflections of the scattering beam on the cell curvature, which make quantitative analysis very difficult. However, important qualitative information is easily extracted. For these reasons, most of our measurements were carried out in the radial beam geometry that provides information in the flow and neutral direction. Data in the tangential beam geometry (not shown here) were only obtained for

[‡] Reproduced in part with permission from *Macromolecules*, Loizou, E.; Butler, P. D.; Porcar, L.; Schmidt, G., Dynamic Responses in Nanocomposite Hydrogels, **2006**, 39, 1614-1619. Copyright 2006 American Chemical Society.

selected samples and shear rates, in order to verify the type of orientation suggested by radial measurements.

Small angle neutron scattering measurements were performed at the NIST Center for Neutron Research using both NG3 and NG7 SANS instruments.[163] The typical q-range used for these measurements is from 0.003 $Å^{-1}$ to 0.25 $Å^{-1}$, corresponding to a characteristic distance ($d = 2\pi/q$) probed of ≈ 2000 Å to 25 Å. The incident neutron beam had a wavelength of either 6 Å or 8 Å. Couette cells with gaps of 0.5 mm and 1mm were used giving a total path length through the sample of 1 mm and 2 mm, respectively. The temperature of the samples was set at 23 ºC and was controlled by a thermostating fluid that circulated around the Couette cell. A solvent trap was used to prevent solvent evaporation. The scattering data from each sample were corrected for background noise, detector efficiency, empty cell scattering, sample transmission, and intensities were placed on an absolute scale (cm^{-1}) using beam flux measurements.[164]

5.2 Structural Dependence on the Molecular Weight (M_w)

The influence of shear flow on Laponite-PEO suspensions has been investigated by Schmidt *et al*.[43-45] using the shear-SANS technique. Their measurements showed that sufficient shearing induces nanoscale orientation to a sample containing 3 wt % Laponite and 2 wt % PEO (M_w = 1000 kg/mol). In contrast, a pure 2 wt % PEO solution and a pure 3 wt % Laponite solution, showed no nanoscale orientation. The orientation was attributed to interconnected clay platelets being forced to align along the flow direction and to the bridged polymer chains being stretched under shear. The authors suggested that the observed orientation arises from the dynamic coupling of the polymer chains with the clay platelets. While long polymer chains may indeed be able to bridge clay

platelets, sufficiently short ones might not be able to do so. While in Chapter 3 the structure at rest was found to be independent of molecular weight, one would expect the dynamics to be dramatically different once the chains are too small to bridge the clay platelets. To test the validity of the above picture and investigate the influence of polymer length on the shear-induced structures, shear-SANS measurements were performed on a series of polymer-clay gels with varying polymer molecular weight. These measurements allow us to explore the effect of bridging on the shear responses of the gels.

5.2.1 Sample Preparation

Samples containing 3 wt % Laponite and 2 wt % PEO of varying molecular weight (LRD3-PEO2-Mw) were prepared in D_2O. The solutions had a pH value of ≈ 10 and a sodium chloride concentration of 10^{-3} mol/L and were prepared as was described in section 3.1.1.

5.2.2 Results and Discussion

The two dimensional SANS patterns for the different M_w hydrogels, at rest and for selected shear rates, are shown in Figure 5.1. As was shown in Chapter 3, at rest ($0\ s^{-1}$), the isotropic 2D-SANS patterns suggest that all the gels exhibit a random orientation of their nanometer structure. At low shear rates, the scattering patterns are characterized by an increase of the intensity in the direction parallel to the flow field (x-direction). These scattering patterns are usually referred to in the literature as "butterfly patterns" (see for example the scattering pattern of LRD3-PEO2-Mw300 at $30\ s^{-1}$). This increase in the intensity occurs at small q values (close to the beam-stop) and reveals that the low-shear induces the formation of large-scale structures (of sizes > 2000 Å) that orient along the neutral direction. The range of shear rates at which butterfly patterns are

observed is different for each sample; it decreases and shifts to lower values with increasing polymer molecular weight.

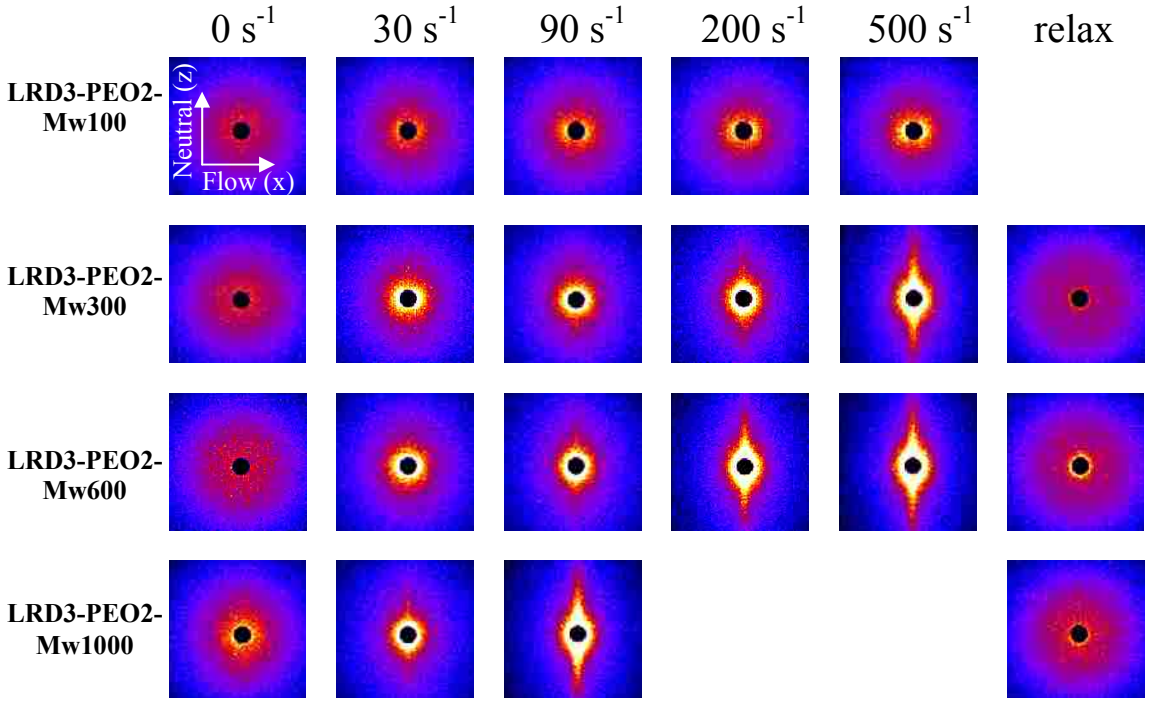

Figure 5.1: Two dimensional SANS patterns for the four LRD3-PEO2-Mw hydrogels at rest, at different shear rates, and upon cessation of shear. Data obtained in the radial beam geometry. Measurements for the LRD3-PEO2-Mw1000 sample were difficult to obtain at shear rates higher than 120 s^{-1}, due to high forces pushing the sample out of the shear cell

At higher shear rates (Figure 5.1), and only for the higher M_w samples, an anisotropic scattering pattern (vertical streak) develops in the neutral (z) direction (see for example the scattering pattern of LRD3-PEO2-Mw300 at 500 s^{-1}). This type of anisotropy suggests that on average, the orientation of nanoscopic structures is along the flow direction. The amount of oriented nanoscale structures increases with both shear rate and polymer molecular weight. The anisotropic scattering patterns become isotropic again, upon cessation of shear (scattering patterns in the last column of Figure 5.1). This suggests that the oriented nanostructures relax very fast. The relaxation time of the

nanoscale structures has been reported to be ≈ 0.05 s for these systems.[43] While SANS studies on these polymer-clay solutions reveal very fast relaxation of anisotropy, stress-relaxation measurements (section 4.2.3) show that full relaxation of the samples requires very long times. These two results imply the presence of two relaxation processes, a fast relaxation of nanoscopic structures, and a much slower stress relaxation mode of the macroscopic structures.

To quantitatively analyze the scattering data and obtain the scattered intensity as a function of the scattering vector, q, in each direction, all SANS patterns were averaged in 10° sectors parallel to the flow (x) and neutral (z) directions. Figures 5.2, 5.3, and 5.4 show the averaged scattering profiles from the LRD3-PEO2-Mw100, 300 and 600 gels respectively, at rest and at different shear rates.

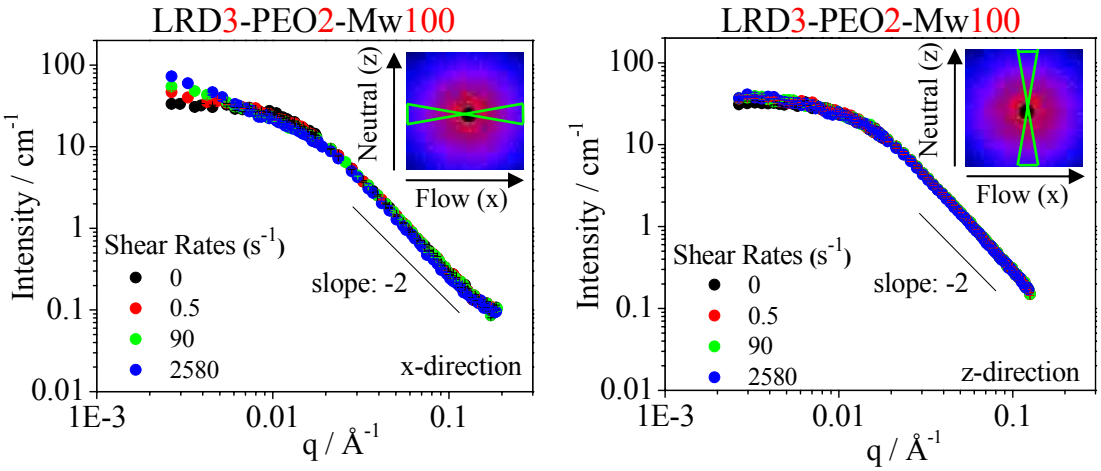

Figure 5.2: Intensity vs. q for the LRD3-PEO2-Mw100 gel at rest (0 s^{-1}) and at different shear rates. The data were averaged parallel to the flow (x) and neutral (z) directions. Relative error is smaller than the symbols. **Inserts:** 2D SANS patters showing the sectors used for averaging the intensity

The data at rest were explained in detail in Chapter 3. As a reminder, the scattering profiles of all the gels exhibit a slope slightly greater than the -2 expected for

disc-like structures at high q values. This value is not surprising given that the free polymer must also contribute to the scattering in this regime. At low q values all the gels exhibit a strong rollover (plateau). From a Guinier fit to that region, an "apparent" R_g of ≈ 10 nm was calculated. This R_g is consistent with the R_g obtained for thin discs of 25-30 nm in diameter (section 3.2.2).

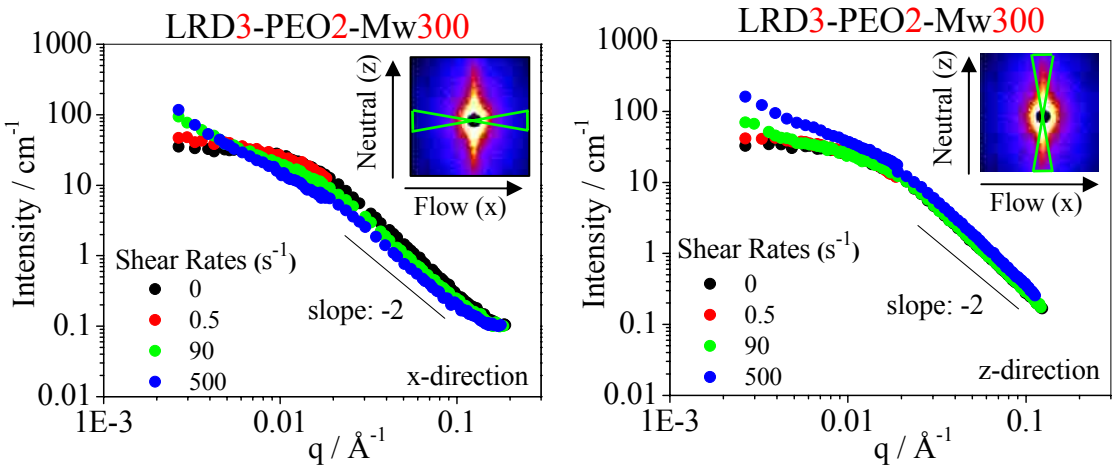

Figure 5.3: Intensity vs. q for the LRD3-PEO2-Mw300 gel at rest (0 s^{-1}) and at different shear rates. The data were averaged parallel to the flow (x) and neutral (z) directions. Relative error is smaller than the symbols. **Inserts:** 2D SANS patters showing the sectors used for averaging the intensity

For the LRD3-PEO2-Mw100 sample (Figure 5.2) the intensity in the neutral (z) direction is more or less the same for all shear rates. In the flow (x) direction, a slight upturn, at low q, is observed only at the higher shear rates. This contrasts with the higher molecular weights such as LRD3-PEO2-Mw300 and 600 (Figures 5.3 and 5.4) where anisotropy is evident over the entire q regime at the higher shear rates. In these figures, the intensity curves parallel to the flow (x) and neutral (z) directions, split above and below the data at rest. The curves parallel to the flow (x) direction decrease relative to the

"at rest" curve indicating they are probing more of the longer dimension. The curves parallel to the neutral (z) direction, which are increasing in intensity, are probing more of the shorter dimension. Thus, a nanoscopic orientation occurs only within the high M_w samples.

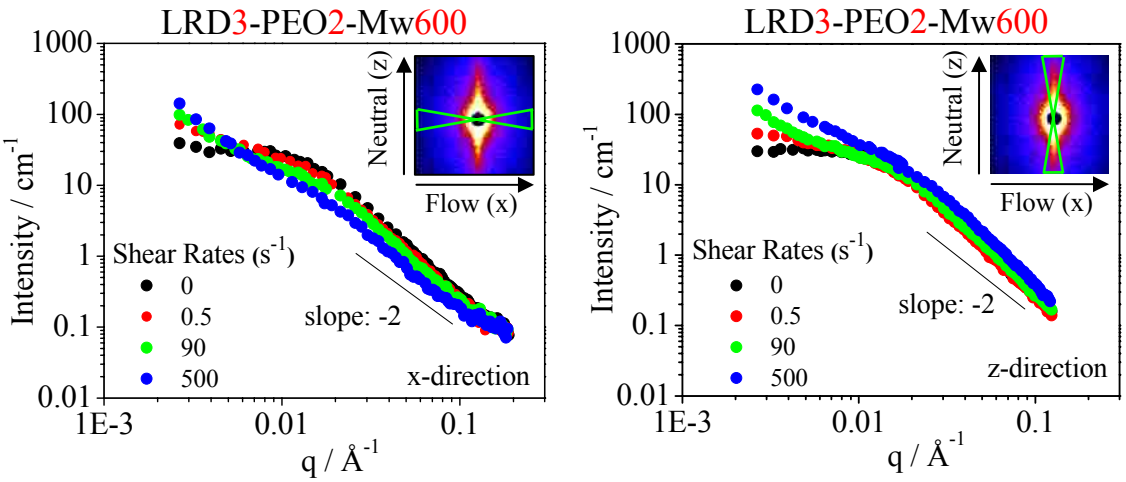

Figure 5.4: Intensity vs. q for the LRD3-PEO2-Mw600 gel at rest (0 s^{-1}) and at different shear rates. The data were averaged parallel to the flow (x) and neutral (z) directions. Relative error is smaller than the symbols. **Inserts:** 2D SANS patters showing the sectors used for averaging the intensity

Figure 5.5 shows a comparison of the scattering profiles at rest (0 s^{-1}) for one of the hydrogels (the LRD3-PEO2-Mw600 hydrogel), with the scattering profiles at shear rates of 10 s^{-1} and 500 s^{-1}. At high q and low shear rates (such as 10 s^{-1}) the curves overlap, suggesting that no nanoscopic alignment occurs at these shear rates. At high q and high shear rates (such as 500 s^{-1}) the intensity parallel to the flow direction (x) is decreasing, while the intensity parallel to the neutral direction (z) is increasing, suggesting nanoscopic alignment in the flow direction. At low q, both the low and high shear rate data show intensity profiles that increase relative to the "at rest curve", for both

directions studied. The main difference though is that at low shear rates (such as 10 s^{-1}) the intensity parallel to the flow (x) direction is higher, while at high shear rates (such as 500 s^{-1}) the intensity parallel to the neutral (z) direction is higher. This indicates that besides the nanoscale alignment, shear induces the formation of a large-scale structure, which is also anisotropic and aligns at low shear rates in the neutral (z) direction, while orientation in the flow (x) direction appears to dominate at high shears. However, it should be noted that for some of these samples, the literature[70, 71] indicates that the large-scale structure retains its neutral (z) direction orientation. It is likely that at the very low q presented here, the nanoscopic orientation in the flow direction dominates the scattering and overwhelms the tail of the signal arising from the large-scale structure. This would of course also imply that the large-scale structure forms prior to significant local alignment.

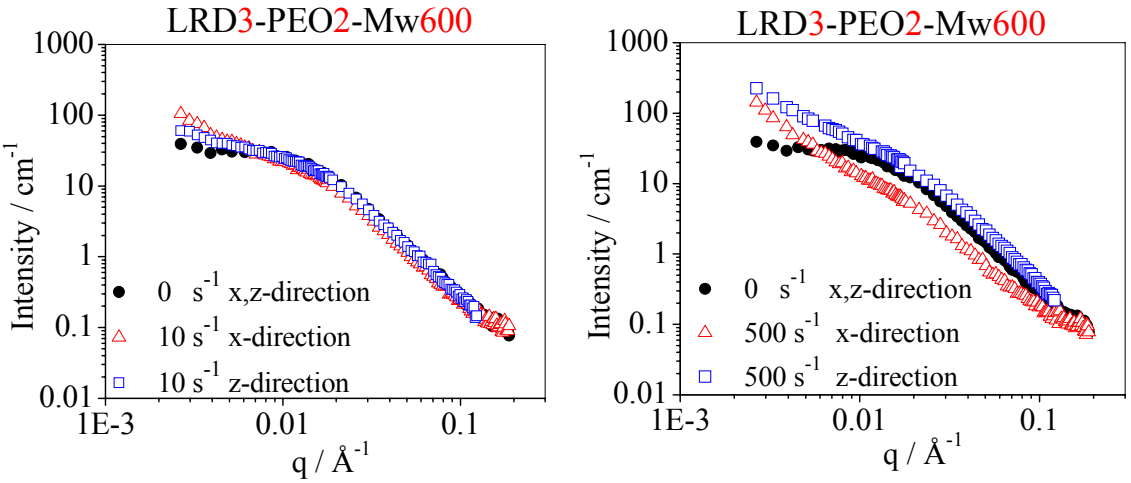

Figure 5.5: Intensity vs. q for the LRD3-PEO2-Mw600 gel at rest (0 s^{-1}) and at shear rates of 10 s^{-1} (left) and 500 s^{-1} (right). The data were averaged parallel to the flow (x) and neutral (z) directions. Relative error is smaller than the symbols

To observe the dependence of the anisotropy on the molecular weight, data for a fixed shear rate of 90 s^{-1} were gathered. The data are presented in Figure 5.6. All but the

lowest molecular weight (M_w = 100 kg/mol) show high q anisotropy. This anisotropy increases as a function of molecular weight, suggesting a higher degree of oriented nanostructures in these gels. This then supports the original hypothesis that the higher the M_w of the polymer in the gel, the more interconnections can be supported and the stronger the resulting network, which in turn leads to an increased ability to orient the platelets under shear. Even though the shear flow is expected to disrupt the network and break some of the connectivity, if the number of polymer bridges is high enough, some bridges will remain. Furthermore, long polymer chains will have a higher probability to bridge to another clay platelet located nearby after desorbing from a particular clay platelet. Therefore, the coupling of clay platelets with longer polymer chains will restrict the mobility of higher amounts of coated-clay platelets and lead to their shear orientation.

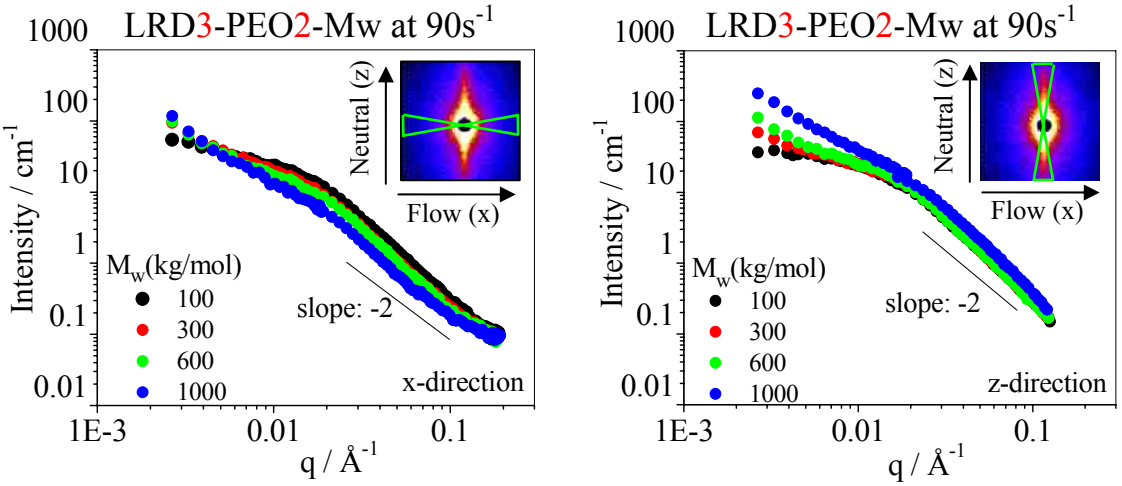

Figure 5.6: Intensity vs. q for the LRD3-PEO2-Mw samples, at a shear rate of 90 s^{-1}. The data were averaged parallel to the flow (x) and neutral (z) directions. Relative error is smaller than the symbols. **Inserts:** 2D SANS anisotropic scattering patterns showing the sectors used for averaging the intensity

A common method for quantifying the degree of orientation in oriented samples involves calculating an annular average of the scattering intensity. This is an average of the intensity over the area between two concentric rings that have the beam-stop as their centers. From this type of average the scattering intensity at a specific q value ($\pm \Delta q$) is obtained as a function of the annular angle. For all the scattering data, the annular intensity was calculated at two different q values. At q = 0.0040 ± 0.0008 $Å^{-1}$ so as to obtain information about the large-scale structures (of sizes ~ 1570 Å), and at q = 0.0100 ± 0.0008 $Å^{-1}$ so as to obtain information about structures slightly larger than an individual disk (of sizes ~ 628 Å). As an example Figure 5.7 shows the annular averages at the two different q values for the 2D SANS pattern of the LRD3-PEO2-Mw300 sample at 30 s^{-1}.

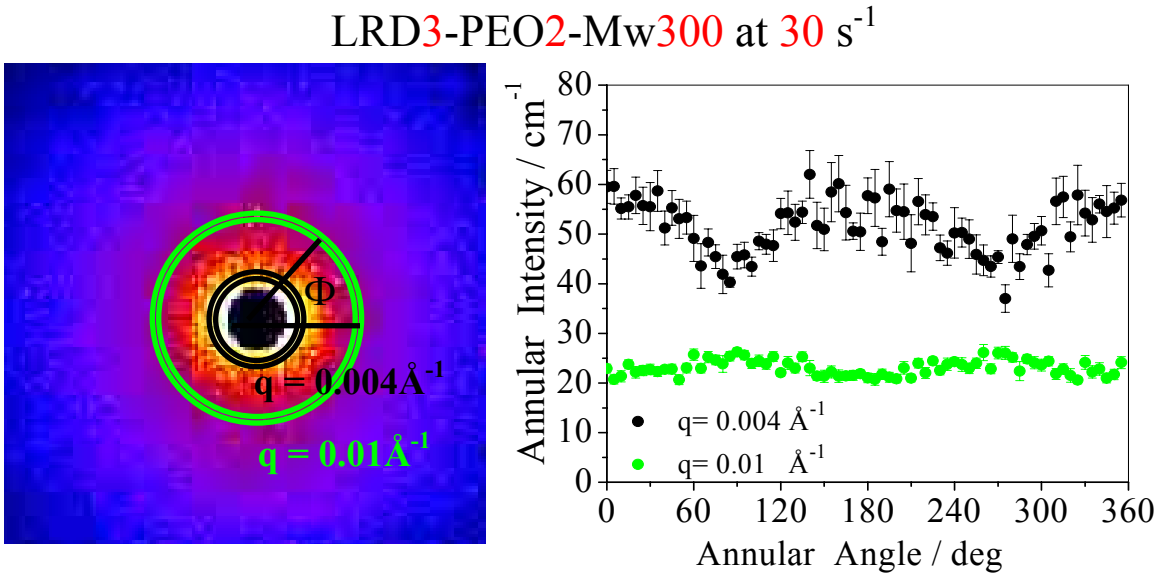

Figure 5.7: 2D SANS pattern (of the LRD3-PEO2-Mw300 sample at 30 s^{-1}) showing annular average (left) of the intensity at two different q values, at q = 0.004 $Å^{-1}$ and at q = 0.01 $Å^{-1}$. From this type of average, the annular scattering intensity $I_q(\Phi)$ is obtained as a function of the annular angle Φ (right). Reference direction is the flow direction

The annular scattered intensity, $I_q(\Phi)$, and the annular angle, Φ, were used to calculated the Herman's orientation function (also called Herman parameter) using the following equation:[144, 170]

$$f_q = \frac{3\left\langle \cos^2\Phi \right\rangle - 1}{2} \tag{5.1}$$

where

$$\left\langle \cos^2\Phi \right\rangle = \frac{\int_0^{2\pi} I_q(\Phi)\cos^2\Phi \sin\Phi \, d\Phi}{\int_0^{2\pi} I_q(\Phi)\sin\Phi \, d\Phi} \tag{5.2}$$

The Herman parameter has a value of -0.5 when the components in the system are perfectly oriented parallel to the flow direction, a value of 1 when the components are perfectly oriented perpendicular to the flow direction (parallel to the neutral direction) and a value of 0 when the orientation is random (see Table 5.1).[144, 170]

Table 5.1: Values of Herman parameter and their interpretation on structure orientation

Values for Herman parameter	**Interpretation of Structure Orientation**
$f_q = -0.5$	perfect orientation in the flow direction
$-0.5 < f_q < 0$	average orientation in the flow direction
$f_q = 0$	random orientation
$0 < f_q < 1$	average orientation in the neutral direction
$f_q = 1$	perfect orientation in the neutral direction

Figure 5.8 summarizes the shear-SANS results by plotting the Herman parameter, as a function of shear rate for each of the gels in the series (LRD3-PEO2-Mw100, 300,

600, 1000). The Herman parameter was calculated at two different q values of 0.004 $Å^{-1}$ and 0.01 $Å^{-1}$. At q = 0.01 $Å^{-1}$, the LRD3-PEO2-Mw100 sample exhibits similar behavior to a pure 3 wt % Laponite gel with the Herman parameter fluctuating around zero, indicating that in these gels the nano structures maintain their random orientation up to shear rates of 2580 s^{-1}. However, the LRD3-PEO2-Mw300, 600 and 1000 samples display mostly negative values of the Herman parameter, revealing nanoscopic orientation along the flow direction, which increases with increasing M_w and shear rate. This verifies our earlier suggestion that the observed alignment in the hydrogels arises from the coupling between the clay platelets and the polymer chains. Sufficiently long polymer chains bridge the platelets, but short polymer chains like those of M_w = 100 kg/mol cannot tie the clay platelets together. The low q data at 0.004 $Å^{-1}$ reveal the presence of shear induced large-scale structures in all the hydrogels. These large-scale structures orient at low shear rates along the neutral direction (positive Herman parameter).

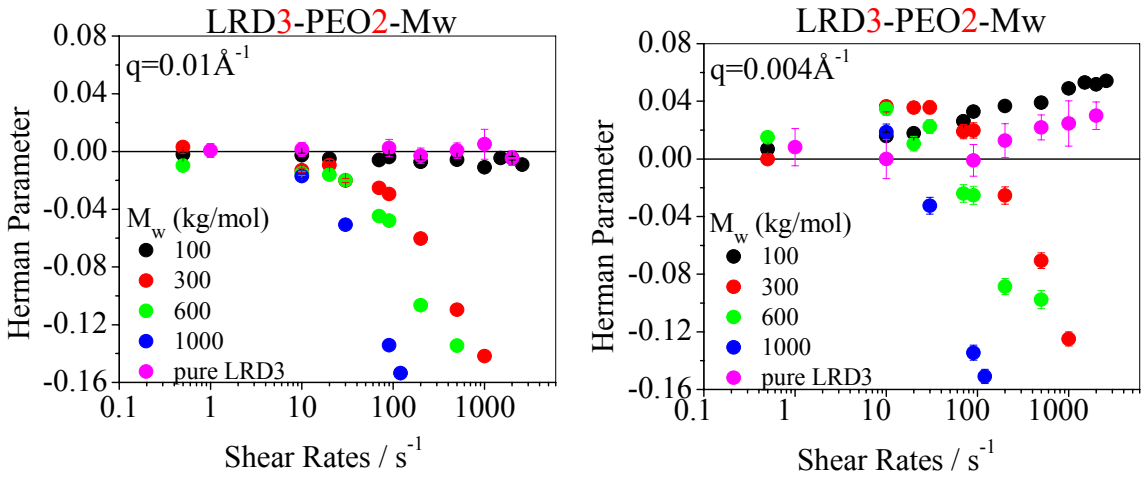

Figure 5.8: Herman parameter calculated at q values of 0.01 $Å^{-1}$ (left) and 0.004 $Å^{-1}$ (right) as a function of shear rate, for the different M_w hydrogels. For comparison, data from a pure 3 wt % Laponite solution are also plotted

Combining our previous results with the present measurements for these Laponite-PEO systems, the picture that emerges is that the clay platelets are completely covered by adsorbed PEO segments, with some additional excess PEO that is not bound to the clay. If long enough, the adsorbed polymer chains can bridge neighboring clay particles and form a network. At rest, the system is free of stress, so that the coated-clay particles and the diffuse polymer chains are randomly oriented giving rise to isotropic scattering patterns. When a shear field is applied, the SANS patterns develop an anisotropy along the neutral direction for the gels with higher polymer M_w. This would be due to the long polymer chains bridging several coated clay platelets, restricting their ability to move freely and causing them to orient along the flow direction (with their face normal parallel to the neutral direction, 'a'-orientation). On the other hand, the systems containing very short polymer chains (for example M_w = 100 kg/mol) do not exhibit this anisotropic pattern under shear, indicating that there is no platelet alignment. At these shorter lengths, the polymer is unable to interconnect several platelets and thus the clay is not restricted in its response to the flow, behaving much like a simple clay suspension without added polymer. Upon cessation of shear, the nanoscopic structure recovers immediately. The recovery from the anisotropic SANS patterns is faster than expected from simple Brownian dynamics of clay particles in a viscous medium.[43, 44] Thus it is likely that as the chains retract on cessation of shear, the dynamic coupling between the polymer chains and the clay platelets, no doubt, contributes strongly to the randomization of the clay orientation.

Oriented large-scale structures induced by flow have been observed in various systems, for example in: networks swollen by short polymer chains,[171] mixtures of short

and long homopolymers,[172] cross-linked networks,[171, 173, 174] worm-like micelles,[175, 176] mixtures of polymer with latex particles,[177] clay suspensions,[167] silica-filled polydimethylsiloxane composites,[178] entangled polymer melts,[172] and many more. Although the origin of the induced large-scale structures may be different for each of the above systems, their scattering patterns have similar features. They are characterized by an increase of the intensity in the direction parallel to the flow and are known as "butterfly patterns".[179] According to Vermant,[180] large-scale structures can develop colloidal dispersions that are intrinsically inhomogeneous (for example in the case of aggregated or flocculated suspensions) or materials that can become inhomogeneous during flow. In our case, as it was shown in Chapter 3 from the USANS data together with ESEM images, large-scale sponge-like structures exist at rest. When these polymer-clay gels are subjected to flow, the existing large-scale inhomogeneities become much more pronounced and in fact extend to higher q than the at rest structures. Therefore under shear they become detectable at the lowest q values of the SANS regime. A possible explanation for this is that under the effect of hydrodynamic forces, the structures within the fractal-like network contract and roll-up on themselves.[167] Thus, along the neutral direction, cigar-like banded structures may develop, giving rise to butterfly scattering patterns along the flow direction.[180] These shear induced structures are consistent with findings by Gibson *et al*.,[70, 71] who concluded that transient micron-scale heterogeneities develop during shear.

5.3 Contrast Matched Data

In order to explore the contributions of the individual components of the system (clay and polymer) to the structural rearrangements under flow, measurements were made

in two mixed solvents: contrasting out the polymer and the clay, respectively. Thus, in this section shear-SANS data obtained from samples in contrast matched solvents are presented and are compared with data obtained in D_2O.

5.3.1 Sample Preparation

The samples consisted of 3 wt % Laponite clay and 2 wt % PEO of different molecular weights and were prepared in contrast matched solvents. The solvent used to contrast match the Laponite clay particles contained 70 vol % D_2O and 30 vol %. To contrast match the PEO chains, a solvent with 17 vol % D_2O and 83 vol % H_2O was used. All solutions had a pH value ≈ 10 and a sodium chloride concentration of 10^{-3} mol/L. The samples were prepared as described in section 3.1.1.

5.3.2 Results and Discussion

Figures 5.9 and 5.10 summarize the shear-SANS data obtained from samples in contrast matched solvents. The Herman parameters calculated at q values of 0.01 $Å^{-1}$ and 0.004 $Å^{-1}$, are plotted as a function of shear rates for each sample. Figure 5.9 shows data from samples where the solvent is contrast matched to the PEO polymer chains, abbreviated as PEOcm. In this case, the scattering comes only from the clay particles. From the high q data (q = 0.01 $Å^{-1}$), it is obvious that shear induces orientation of the clay platelets only for the high M_w samples. The degree of orientation in these samples increases with increasing polymer M_w and shear rates, as noted previously. Figure 5.10 shows data from samples where the solvent is contrast matched to the Laponite particles, abbreviated as LRDcm. In this case, the clay platelets appear invisible even though they are present and contribute to the structure, and the scattering arises from the polymer-polymer correlations. The polymer contribution to the scattering however comes from the

polymer network bridging the platelets, the free polymer chains, and the polymer coating the clay. The latter will behave structurally exactly like the clay, making it difficult to separate out signals coming from the bridging polymer alone.

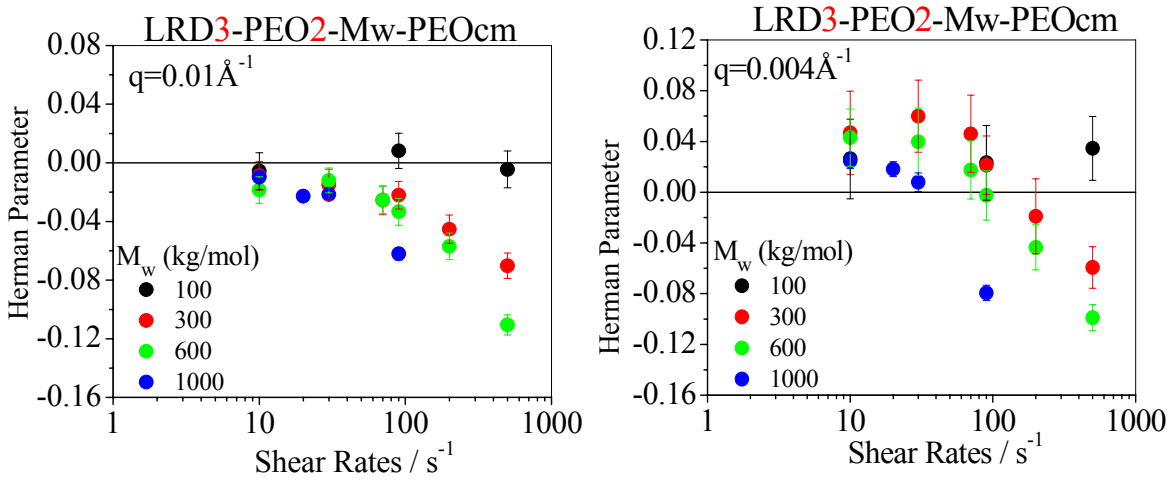

Figure 5.9: Herman parameter calculated at q values of 0.01 Å^{-1} (left) and 0.004 Å^{-1} (right) as a function of shear rate, for all the M_w samples. Solvent is contrast matched to the PEO polymer chains

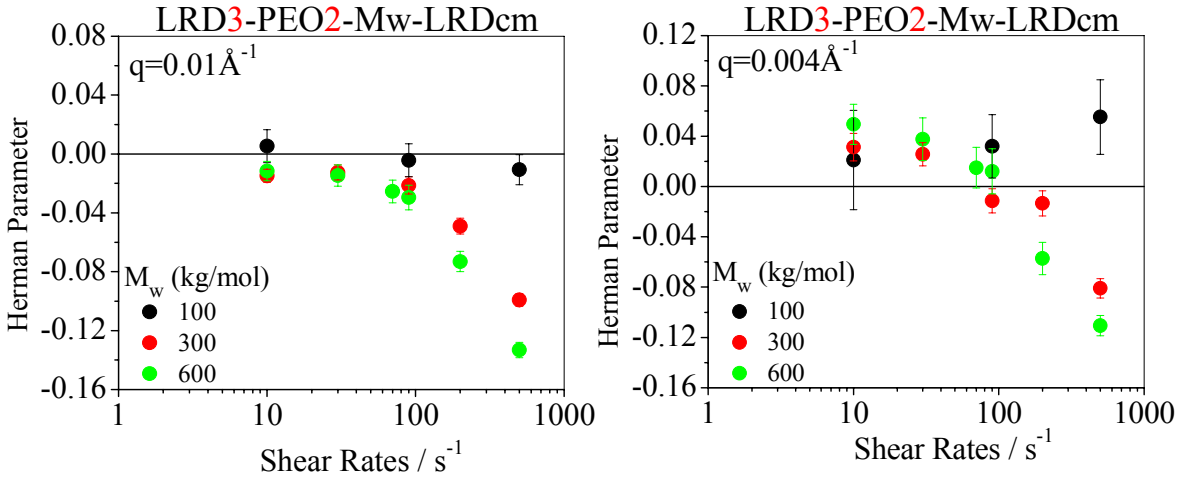

Figure 5.10: Herman parameter calculated at q values of 0.01 Å^{-1} (left) and 0.004 Å^{-1} (right) as a function of shear rate, for all the M_w samples. Solvent is contrast matched to the Laponite clay particles

At low q (q = 0.004 $Å^{-1}$) it can be seen from the data presented in Figures 5.9 and 5.10, that both the clay platelets and the polymer chains contribute to the existence of large-scale structures. Here as well, it is nearly impossible to separate the contributions from the polymer chains coating the clay platelets and from the bridged polymer chains. However, it is clear that these elongated columns of material that orient along the neutral direction, include clay density fluctuations, and are not solely due to the polymer.

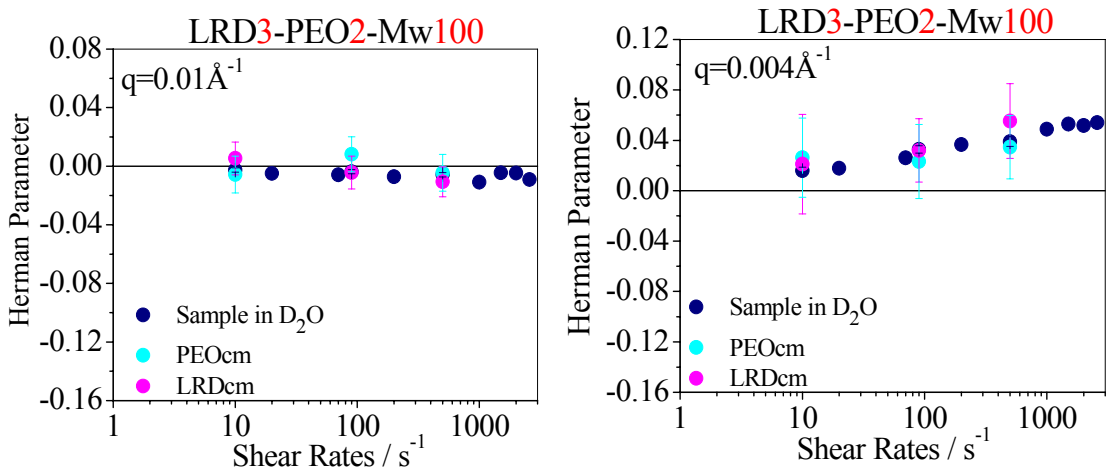

Figure 5.11: Herman parameter calculated at q values of 0.01 $Å^{-1}$ (left) and 0.004 $Å^{-1}$ (right) as a function of shear rate. The data are form LRD3-PEO2-Mw100 samples in D_2O and in contrast match solvents

The calculated Herman parameter (at q values of 0.004 $Å^{-1}$ and 0.01 $Å^{-1}$) as a function of shear rate for the LRD3-PEO2-Mw100 sample in D_2O and in contrast matched solvents is presented in Figure 5.11. For this hydrogel, at high q (q = 0.01 $Å^{-1}$), the Herman parameter in the three solvent conditions fluctuates around zero, for all measured shear rates. This indicates that both the clay nanoparticles and the polymer chains maintain their random orientation under shear. At low q (q = 0.004 $Å^{-1}$), both the

clay platelets and the polymer chains contribute to the development of large-scale structures under shear that orient along the neutral direction for the entire range of shear rates, as it was suggested they do in the case of the larger M_w polymers.[70, 71]

The Herman parameter (at q values of 0.01 $Å^{-1}$ and 0.004 $Å^{-1}$) as a function of shear rate for the LRD3-PEO2-Mw300 and the LRD3-PEO2-Mw600 samples is shown in Figures 5.12 and 5.13, respectively. The data are from samples prepared in D_2O and in contrast matched solvents. The q = 0.01 $Å^{-1}$ data shows that the contrast matched samples show the same signature as those in D_2O, with the orientation coming from both components as mentioned previously. At low shear rates, the degree of orientation of the polymer and the clay platelets is similar. At high shear rates, however the LRDcm sample (in which the Laponite is contrast matched to the solvent), displays larger values of the Herman parameter compared to the PEOcm sample (the PEO is contrast matched to the solvent). This suggests that at these high shear rates the polymer exhibits a higher degree of orientation compared to the clay platelets, while the sample in D_2O has an even higher value of the Herman parameter compared to the contrast matched samples. One hypothesis consistent with these data is that the clay platelets align at lower shear than the polymer. This could be due to the lack of internal flexibility of the rigid clay particles, as well as the lack of external flexibility due to coupling with the polymer chains, which makes it easier for the clay platelets to align under the flow compared to the flexible polymer chains. As the shear rate increases, the polymer chains that are coupled to the clay platelets start to stretch and to orient along the flow direction as well. In this scenario, any polymer contributions to the alignment at low shear would come from the polymer coating the clay, explaining why both clay and polymer chains seem to have the

same degree of orientation at these shear rates. At higher shear rates, the bridging polymer chains begin to stretch and start to contribute to the alignment. As the shear continues to increase, these stretched chains exhibit a higher degree of alignment than the clay leading to the observed increase in the Herman parameter. The sample in D_2O has an even higher value of the Herman parameter compared to the contrast matched samples, most probably because this sample has contributions to the orientation from both the clay platelets and the polymer chains. This scenario is in excellent agreement with the findings from Schmidt *et al.*,[44] who proposed that for a sample with M_w = 1000 kg/mol the clay platelets align first, followed by the stretching of interconnected polymer chains, based on their flow-birefringence data.

At q=0.004, the error bars are too large to distinguish any subtle differences between the contributions of each component to the large-scale structure. The fact that both contribute to that structure as mentioned earlier remains the only thing that can be unambiguously stated from these data.

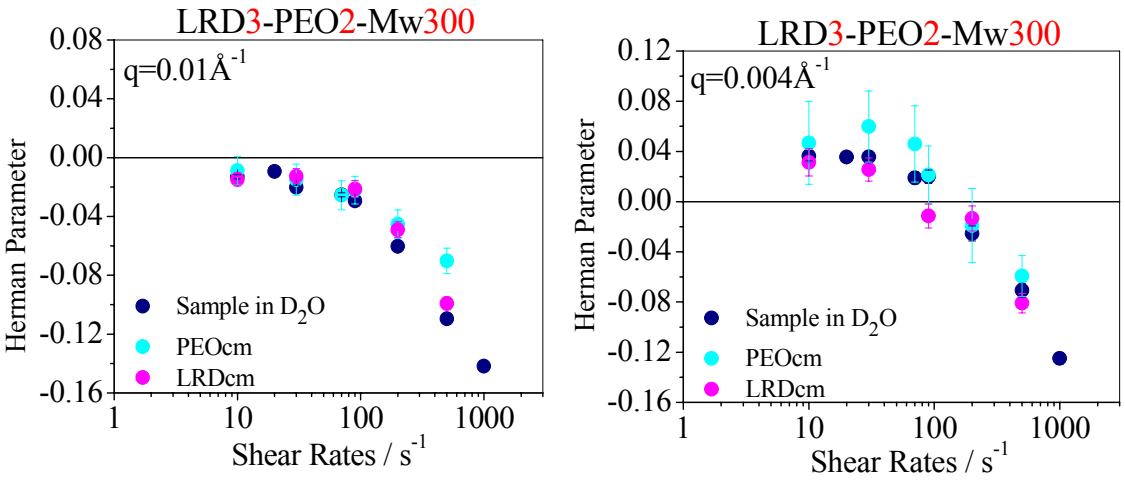

Figure 5.12: Herman parameter calculated at q values of 0.01 $Å^{-1}$ (left) and 0.004 $Å^{-1}$ (right) as a function of shear rate. The data are form LRD3-PEO2-Mw300 samples in D_2O and in contrast matched solvents

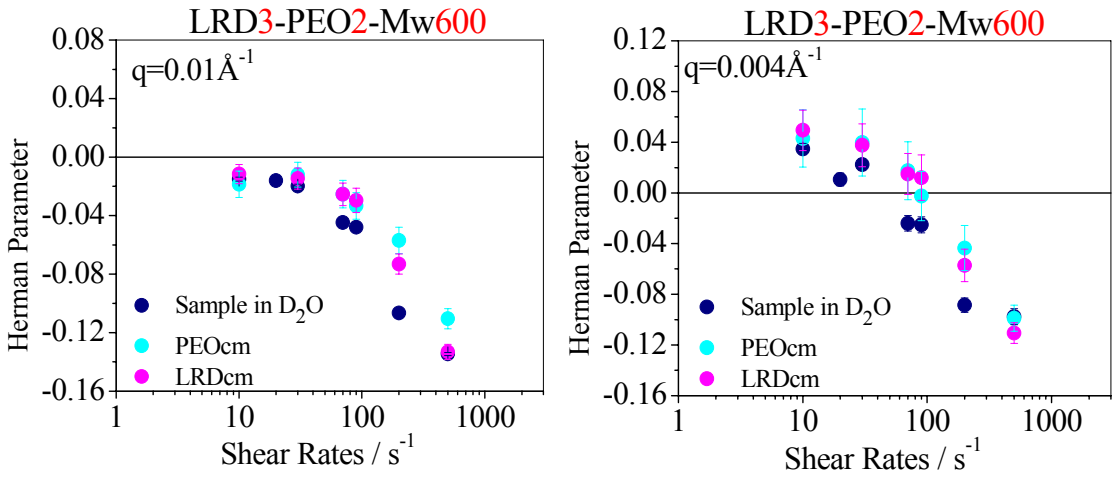

Figure 5.13: Herman parameter calculated at q values of 0.01 $Å^{-1}$ (left) and 0.004 $Å^{-1}$ (right) as a function of shear rate. The data are from LRD3-PEO2-Mw600 samples in D_2O and in contrast matched solvents

5.4 Structural Dependence on the Concentration

In this section, shear-SANS data are presented from samples where either the clay or the polymer concentration are varied and are compared with the data obtained from the LRD3-PEO2-Mw samples presented earlier. By varying the clay and the polymer concentration, the number of free polymer chains (those not adsorbed on the clay surfaces) is also changed. It is expected that the amount of free polymer influences the orientation of the nanoparticles. By performing a systematic study of the effect of concentration on the structure, we aim to eliminate the possibility that the observed orientation of the coated particles in the high M_w systems results from the structural characteristics of a solution when above the overlap concentration, c*. One might suggest that at concentrations higher than c*, the polymer is highly entangled in solution which could restrict the mobility of the platelets and facilitate orientation. If that is the case then

a high entangled system with Mw = 100 kg/mol is expected to show nanoscopic orientation.

5.4.1 Sample Preparation

In order to investigate the influence of concentration on the shear induced structures, samples with different polymer and clay concentrations were prepared. These samples were abbreviated as LRDa-PEOb-Mw, where a and b denote the weight fraction of Laponite and PEO, respectively. These samples were prepared as usual in a D_2O solution with a pH value ≈ 10 and a sodium chloride concentration of 10^{-3} mol/L. The preparation method was the same as described in section 3.1.1.

5.4.2 Results and Discussion

Figures 5.14 and 5.15 show the Herman parameter as a function of shear rate, for the samples with M_w = 100 kg/mol with varying polymer and clay concentrations, calculated at q values of 0.01 $Å^{-1}$ and 0.004 $Å^{-1}$. The high q data (q = 0.01 $Å^{-1}$) shows that neither increasing the polymer concentration nor decreasing the clay concentration, gives rise to any visible nanoscopic orientation in these hydrogels. This confirms that entanglement of the polymer chains has no influence on clay alignment. These results suggest that the connections between the clay platelets and the polymer chains are essential to align them and that simple entanglement between the adsorbed and the free polymer is not enough.

At low q (q = 0.004 $Å^{-1}$) the data in Figures 5.14 and 5.15 suggest that the degree of orientation of the large-scale structures does not change much either with polymer concentration. However, decreasing the number of Laponite platelets in the system

appears to decrease the degree of orientation. This suggests that the clay particles are in fact crucial to the mechanism of forming the large-scale structures.

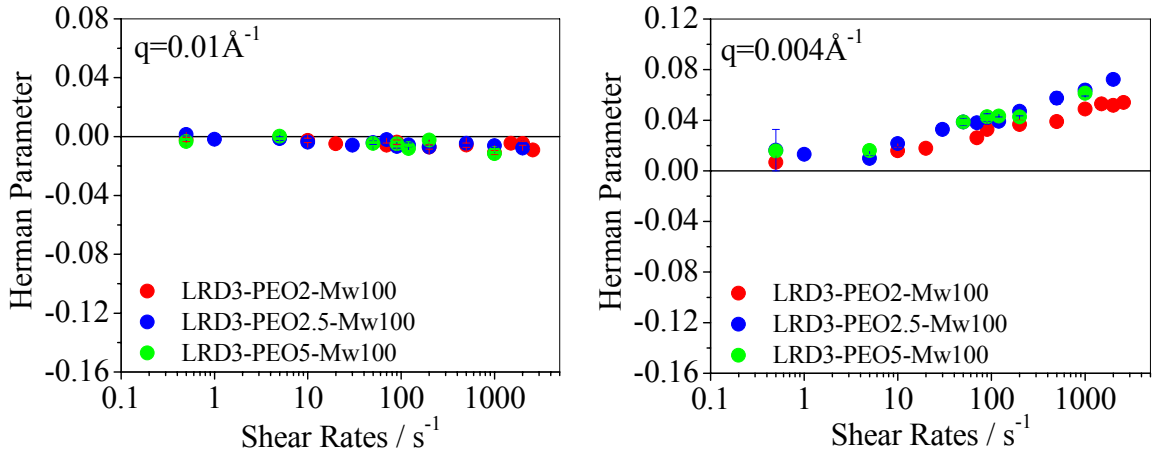

Figure 5.14: Herman parameter calculated at q values of 0.01 $Å^{-1}$ (left) and 0.004 $Å^{-1}$ (right) as a function of shear rate. The data are from samples with M_w = 100 kg/mol, with constant clay concentration and varied polymer concentration

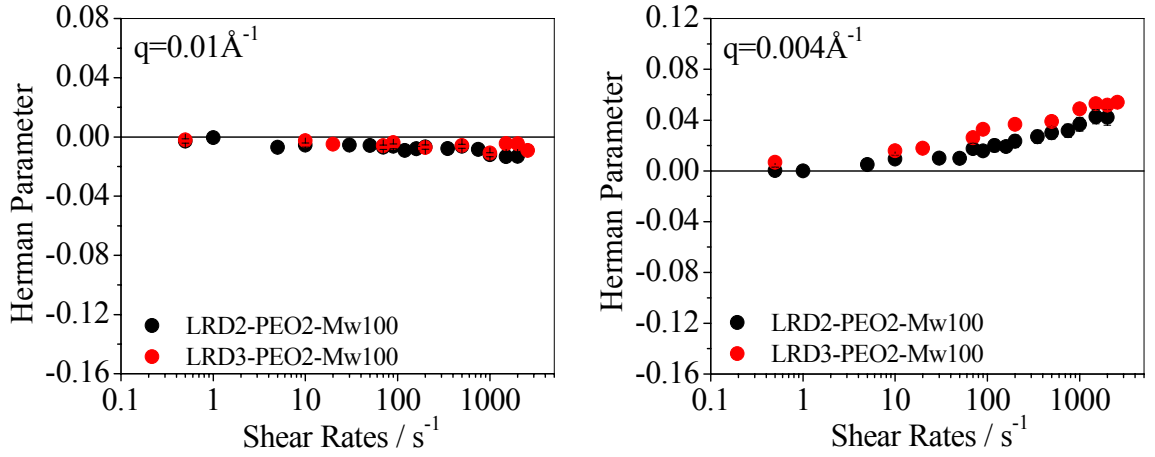

Figure 5.15: Herman parameter calculated at q values of 0.01 $Å^{-1}$ (left) and 0.004 $Å^{-1}$ (right) as a function of shear rate. The data are from samples with M_w = 100 kg/mol, with constant polymer concentration and varied clay concentration

Figures 5.16 and 5.17 show the calculated Herman parameter as a function of shear rate, for the samples with M_w of 300 kg/mol and 600 kg/mol, at q values of 0.01 $Å^{-1}$

and 0.004 $Å^{-1}$. For these systems the clay concentration was kept constant and only the polymer concentration was varied. The data averaged at high q (q = 0.01 $Å^{-1}$) shows that increasing the amount of polymer in the sample, decreases the degree of orientation. Given that the orientation of the clay platelets is due to their interaction with bridging polymer chains, one might suggest that increasing the polymer concentration must somehow decrease the amount of bridging. One way for this to happen would be to assume that all polymer chains compete for the available clay surface. In this scheme, increasing the amount of excess polymer in the sample would lead to an increase in competition between the polymer chains for the clay surface. Thus, when one polymer chain is adsorbed onto one platelet, the probability of finding an empty space on the surface of a neighboring platelet to adsorb onto will decrease with increasing relative polymer concentration. Consequently, the polymer chains will find it difficult to tether neighboring clay platelets and the system will have fewer interconnections, thus leading to the observed decrease in the degree of orientation.

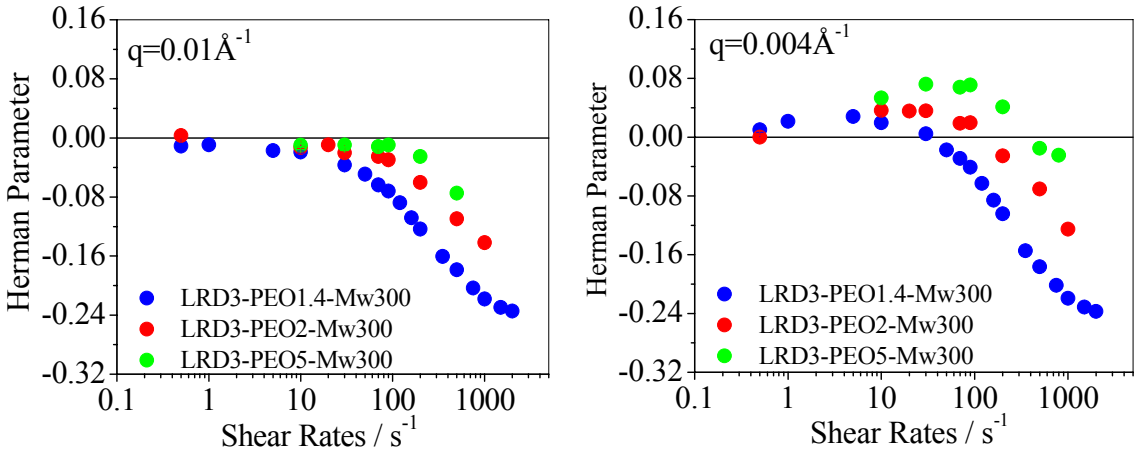

Figure 5.16: Herman parameter calculated at q values of 0.01 $Å^{-1}$ (left) and 0.004 $Å^{-1}$ (right) as a function of shear rate. The data are from samples with M_w = 300 kg/mol, with constant clay concentration and varied polymer concentration

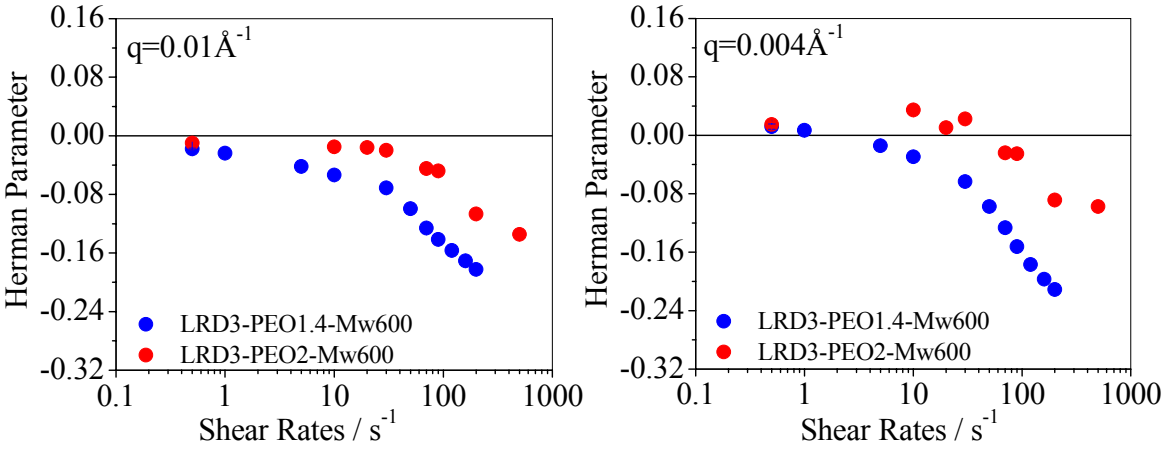

Figure 5.17: Herman parameter calculated at q values of 0.01 Å^{-1} (left) and 0.004 Å^{-1} (right) as a function of shear rate. The data are from samples with M_w = 600 kg/mol, with constant clay concentration and varied polymer concentration

From the data averaged at low q (q = 0.004 Å^{-1}) shown in Figures 5.16 and 5.17, it is clear that when the polymer concentration is high, the large-scale structures that orient along the neutral direction, are more noticeable. At higher shear this orientation appears to reverse. However, published work on the system with M_w = 1000 kg/mol using the shear-light scattering technique showed that the large-scale structure in that system retain their orientation along the neutral direction over the entire range of shear rates.[70, 71] Further, for the low M_w system which show no nanoscopic orientation, the signal from the large-scale structure continues to display its signature even to very high shears. Thus, it is probable that the large-scale structure exists at all shears in all samples, but that the relatively weak tail signal from the large-scale structure is simply obscured by the extremely strong signal from the nanoscopic alignment at high shear for the higher molecular weight samples. This data and the interpretation above would support the idea that as the nanoscopic orientation signal weakens (due to lack of interconnections) it does not obscure the signal of the large-scale structure as much.

Figure 5.18 shows the Herman parameter as a function of shear rate, for samples with a constant polymer concentration (2 wt % polymer of M_w = 600 kg/mol) and varying clay concentration. As usual, data is shown for both q values of 0.01 $Å^{-1}$ and 0.004 $Å^{-1}$. At both q values, the sample with less clay concentration shows a lower degree of orientation. This is consistent with the previous results, which indicate that lowering the clay concentration, increases the excess polymer leading to fewer interconnections. An additional reason is that with fewer particles in the system, the interparticle clay-clay distance increases, making bridging more difficult to occur, in a specific polymer molecular weight sample.

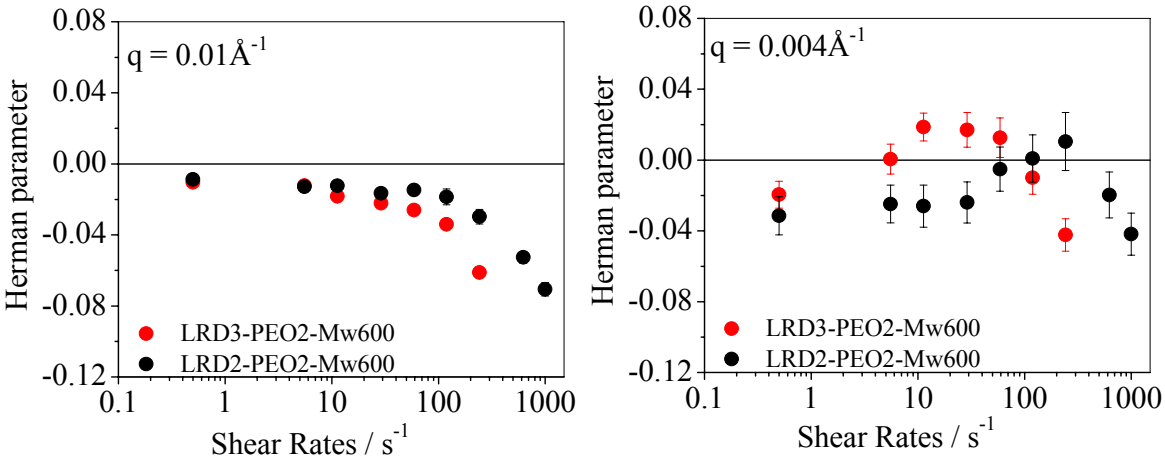

Figure 5.18: Herman parameter calculated at q values of 0.01 $Å^{-1}$ (left) and 0.004 $Å^{-1}$ (right) as a function of shear rate. The data are from samples with M_w = 600 kg/mol, with constant polymer concentration and varied clay concentration

5.5 Structural Dependence on the Preparation Method

In order to investigate the influence of sample's preparation method on the shear induced structures; two different preparation methods were tested. One obvious affect of different sample preparations would be the degree of clay exfoliation. If the clay is less

exfoliated in one preparation method than the other, the clay surface area available for polymer adsorption will decrease affecting the resulting bridging.

5.5.1 Sample Preparation

The samples used contained 3 wt % Laponite clay and 2 wt % PEO of M_w = 300 kg/mol, dissolved in D_2O. The samples as usual had a pH value ≈ 10 and a sodium chloride concentration of 10^{-3} mol/L. The first method (referred here as method A) used to prepare the hydrogels involved mixing the two powders together and then adding the solvent. At the start, large clumps of material form, but after extensive mixing and centrifuging (for a period of approximately 3 weeks), the polymer and Laponite clusters were completely dissolved to obtain hydrogels that looked transparent and homogeneous by visual inspection. In the second method (referred here as method B) the polymer powder was first dissolved in the D_2O solvent. After a period of 4-5 hours, the polymer dissolved and the clay powder was added to the polymer solution under continuous stirring. With this preparation method, macroscopically homogeneous transparent hydrogels (by visual inspection) could be produced within approximately 2-3 days. Even though with this method the samples could be ready sooner, in order to have comparable results, the two samples were prepared on the same day. In addition data from a sample which was prepared 2 days prior to measurements using method B is also presented for comparison.

5.5.2 Results and Discussion

First the influence on the preparation method on the structures at rest was investigated using static USANS, SANS and SAXS measurements for samples prepared using the two aforementioned methods. Results from all techniques show overlapping

data, indicating that at rest, the structure is not a function of the preparation method. Furthermore, from the SAXS data in Figure 5.19, which give us information at high q, the degree of exfoliation of the clay platelets can be detected. The lack of a peak up to q = 1 $Å^{-1}$ suggests that the clay platelets are exfoliated and do not form tactoids, as one would expected from a clay sample that is not well dissolved. Therefore, with both preparation methods well exfoliated samples can be achieved. (The SAXS data were obtained by Dr. Derek Ho at the NIST polymer division).

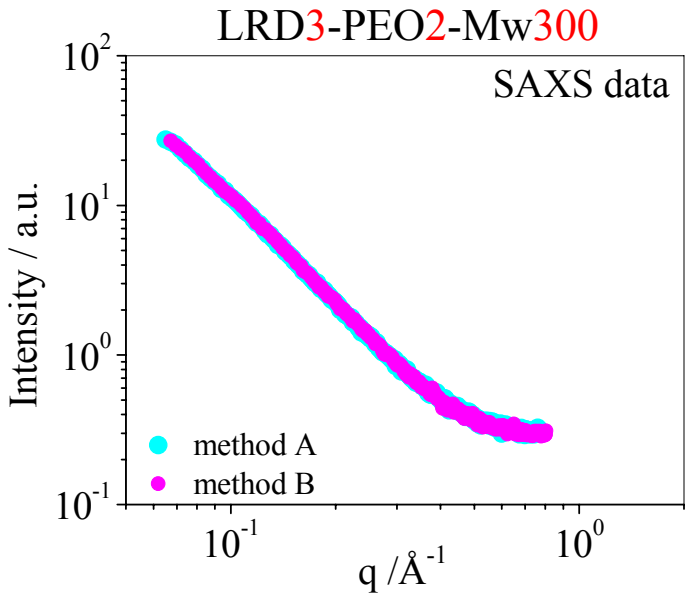

Figure 5.19: SAXS Intensity as a function of q for the LRD3-PEO2-Mw300 samples, which were prepared with two different methods. The preparation method A involved mixing the two powders together and then adding the solvent. The preparation method B involved dissolving the polymer powder into the solvent and then adding the clay powder to the polymer solution

Then the samples were examined under shear to investigate the influence of sample preparation method on the shear induced structures. Figure 5.20 shows the Herman parameter as a function of shear rate as was calculated for both q values of

0.01 Å^{-1} and 0.004 Å^{-1}. The data correspond to LRD3-PEO2-Mw300 samples which were prepared with the two aforementioned methods. The data at q = 0.01 Å^{-1} show that the preparation time and method of the sample do not significantly influence the shear response of the nanoscopic components in the hydrogels. There is a slight difference with the sample preparation method A at very high shear; however, given the small effect compared to the errors no real conclusions can be drawn.

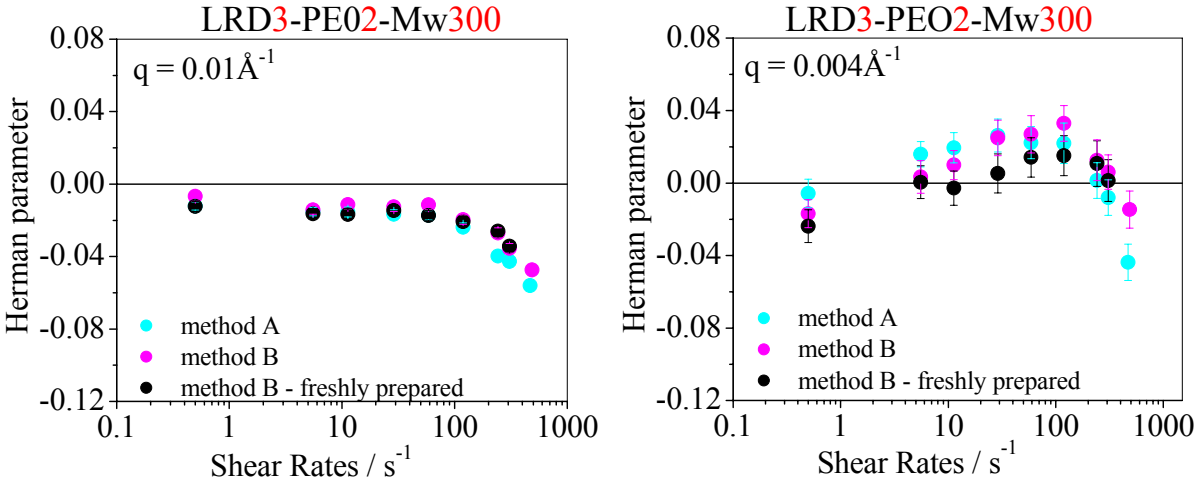

Figure 5.20: Herman parameter calculated at q values of 0.01 Å^{-1} (left) and 0.004 Å^{-1} (right) as a function of shear rate. The data are from the LRD3-PEO2-Mw300 sample prepared with two deferent methods. The preparation method A involved mixing the two powders together and then adding the solvent. The preparation method B involved dissolving the polymer powder into the solvent and then adding the clay powder to the polymer solution

The data averaged at q = 0.004 Å^{-1} (Figure 5.20) indicates that irrespective of the preparation method, large-scale structures develop which have a similar degree of orientation. Despite relative large errors, it does appear that there is a dependence on the preparation time, suggesting that the development of these large-scale structures is a function of time. The structure of the freshly prepared LRD-PEO sample, which is a viscous liquid when loaded into the Couette cell, may be more homogeneous. This is very

similar with the findings of Pignon *et al*.,[167] who studied pure Laponite systems. The authors suggested that the large length scales that govern the macroscopic behavior of Laponite systems are formed due a slow aggregation process that takes several weeks, the kinetics of which are dependent on the particle volume fraction. This could also be the case here. After the sample ages large-scale heterogeneities appear in the sample that can roll-up and orient under shear along the neutral direction. The aging behavior of Laponite systems has been observed by several authors, but its mechanism remains unclear.[94, 97, 102, 104, 106, 181]

5.6 Conclusions

As these polymer-clay gels are subjected to low shear, concentration fluctuations increase along the neutral direction. Those form large-scale structures that have contributions from both clay platelets and polymer chains. With increasing shear-flow the high M_w samples exhibit nanoscopic alignment which comes from coated clay platelets that orient along the flow direction (with their face normal parallel to the neutral direction, 'a'-orientation) and that are 'connected' by bridging stretched polymer chains. The alignment mechanism in these systems arises from the coupling between the clay and the polymer. Long polymer chains interconnect several platelets, acting as multifunctional cross-links, while very short polymer chains are not able to do so. Further, increasing the polymer concentration seems to decrease the degree of orientation exhibited under shear, which is postulated to be due to a competition effect. This would indicate that an optimal polymer to clay ratio exists where the gel is the strongest for a particular clay concentration and polymer molecular weight.

CHAPTER 6 CONCLUSIONS

The structure and interactions of poly(ethylene oxide)-Laponite nanocomposite hydrogels have been investigated by means of microscopy, rheology, and neutron scattering. The structures were examined as a function of polymer molecular weight, polymer and clay concentrations, and sample preparation method in order to better understand these complex systems. Further, selected shear-SANS measurements under conditions of contrast matching were undertaken to begin to elucidate the contributions to the shear induced structures from the individual components.

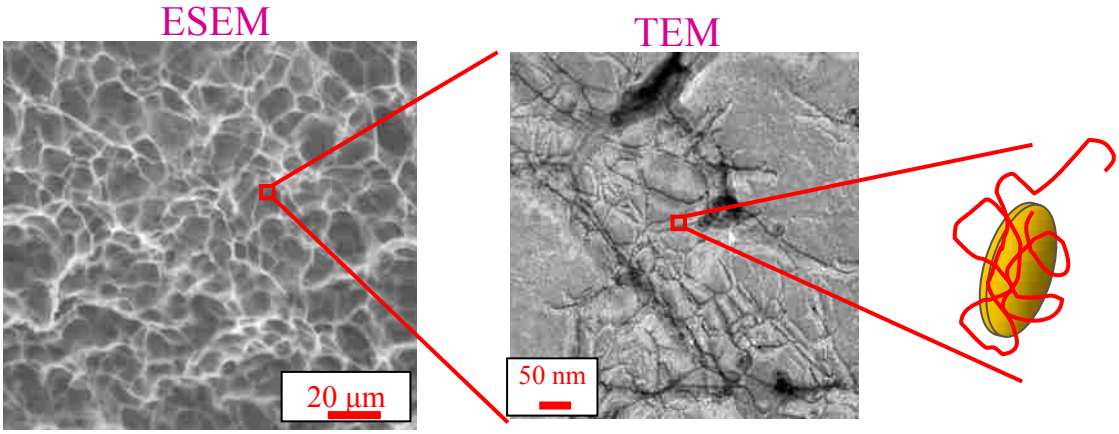

Figure 6.1: Fractal-like network structure from the nanometer to the micrometer, observed with environmental scanning and transmission electron microscopy

For a given concentration of components, static SANS and USANS measurements on the samples revealed that the averaged quiescent structure on all length scales is identical regardless of polymer M_w, or preparation method. The scattering at high q is dominated by the platelet form factor, whereas the low q signal indicates a fractal-like structure on larger length scales. This was confirmed by complimentary TEM and ESEM images (from a representative sample) which showed a network structure

ranging from the nano to the micro regime (Figure 6.1). Thus, the static picture that emerges for these gels is the one in which clay platelets covered by adsorbed PEO segments are woven together in fibrous bundles creating a network structure on multiple length scales. This fractal-like network consists of coated-clay-rich areas and pockets of solutions containing free polymer.

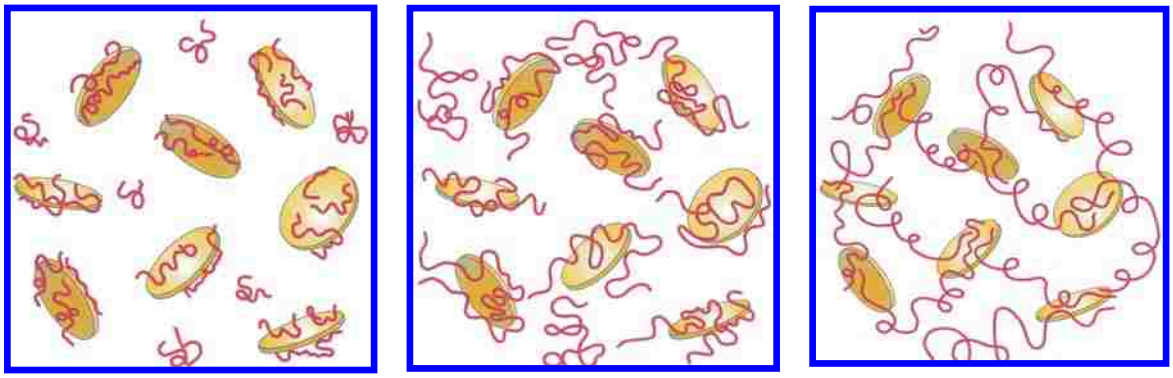

Figure 6.2: Schematic representation of the local structure in Laponite-PEO gels in the absence of shear, for different molecular weights of PEO. The red coils represent the polymer chains and the disk-shape particles the clay platelets. As the polymer chain length is increased, the chains are able to create more polymer-clay interconnections

While the "at rest structures" of these hydrogels appear to be identical, their macroscopic properties differ remarkably with polymer M_w. For example, low M_w hydrogels are relatively brittle and compliant whereas high M_w hydrogels, from which meter long fibers can be drawn, have a gum-like consistency. These differences highlight the importance of the clay-polymer interactions to the materials properties. The critical parameters, which govern these interactions, seem to be the ability of the polymer chains to interconnect two or more clay platelets creating a dynamically cross-linked gel. This is evident from the need for a minimum polymer length (related to the interparticle distance). For example, sufficiently large polymer chains, as in the case of the polymer

with M_w = 1000 kg/mol, can interconnect one or more clay platelets together, whereas shorter polymer chains, such as the M_w = 100 kg/mol are not long enough to do so (Figure 6.2). This idea is also supported by the existence of an optimal polymer concentration for a given clay concentration, above which the competition between polymer chains for the clay surface is high and the amount of bridging is reduced.

At low shear rates, the mechanical coupling between clay platelets and polymer chains has only marginal consequences on the flow properties and the local structure. However, even at these low shear rates, large-scale anisotropic structures appear, which include both polymer and clay density fluctuations, and orient themselves parallel to the neutral direction, as evidence by shear-SANS measurements. These large-scale structures likely exist even at high shear rates for all samples, as they do in the case of the sample with M_w = 100 kg/mol. However, the nanoscopic orientation that occurs at higher shear rates for the higher M_w samples overwhelms the tail of the signal arising from the large-scale structures, making it impossible to verify the existence of those large-scale structures. At higher shear rates, the polymer-clay interactions become increasingly important. This is reflected first in the steady state viscosities, which exhibit a lower amount of shear thinning as the interconnectedness increases, and second in the nanostructure orientation, which increases with increasing M_w. Moreover, this nanoscopic orientation occurs only for the higher M_w samples, suggesting that for a system containing 3 wt % Laponite and 2 wt % polymer, there exists a critical M_w between 100 kg/mol and 300 kg/mol below which the system behaves rheologically very similarly to the pure clay systems and does not exhibit shear-induced nanoscopic orientational ordering. Only once the polymer is long enough to interconnect several clay

platelets nanoscopic alignment becomes possible. While both clay and polymer contribute to this nanoscale alignment as revealed by the shear-SANS experiments in contrast matched solvents, there are slight difference in their respective scattering signals. A hypothesis consistent with the data is that the coated clay platelets align first along the flow direction (with their face normal parallel to the neutral direction, 'a'-orientation), followed by the stretching of the polymer chains that bridge the clay platelets (Figure 6.3).

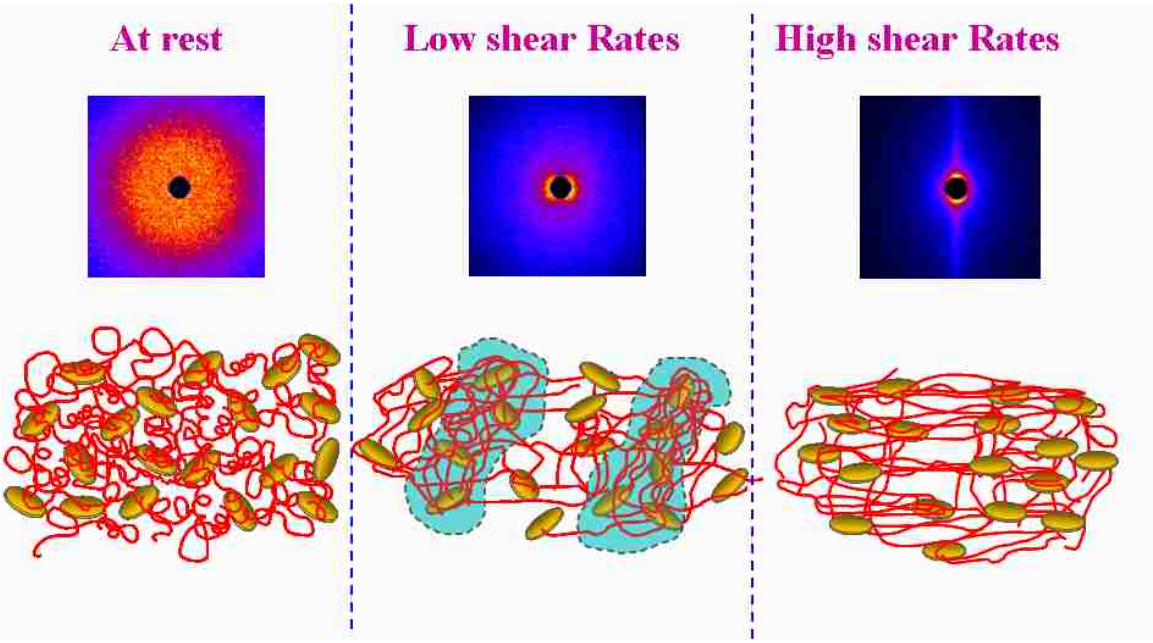

Figure 6.3: At rest, the isotropic scattering pattern suggests random orientation of the nanostructure. At low shear rates, the butterfly scattering pattern suggests that a large-scale structure orients along the neutral direction. At high shear rates, the anisotropic scattering pattern (which appears only within the high M_w samples) suggests that a nanoscopic structure aligns along the flow direction

An illustrative summary of the shear response of these systems is given in Figure 6.4, where a representative sample with M_w = 300 kg/mol is studied with the newly available "rheo-SANS" technique, in which a rheometer is placed on the neutron beam line and the viscosity and SANS patterns are collected simultaneously. Even though

shear-thinning behavior is observed over the entire range of shear rates, the structural responses are different at low and high shear rates. This combine with the fact that the lowest M_w sample (M_w = 100 kg/mol), shows no orientation of the nanoparticles, but exhibits shear thinning behavior, suggest that the shear thinning behavior in these gels does not arise from the alignment of the nanoparticles, but from disruption of the connectivity. The higher the effective cross-links in the system the more difficult the disruption.

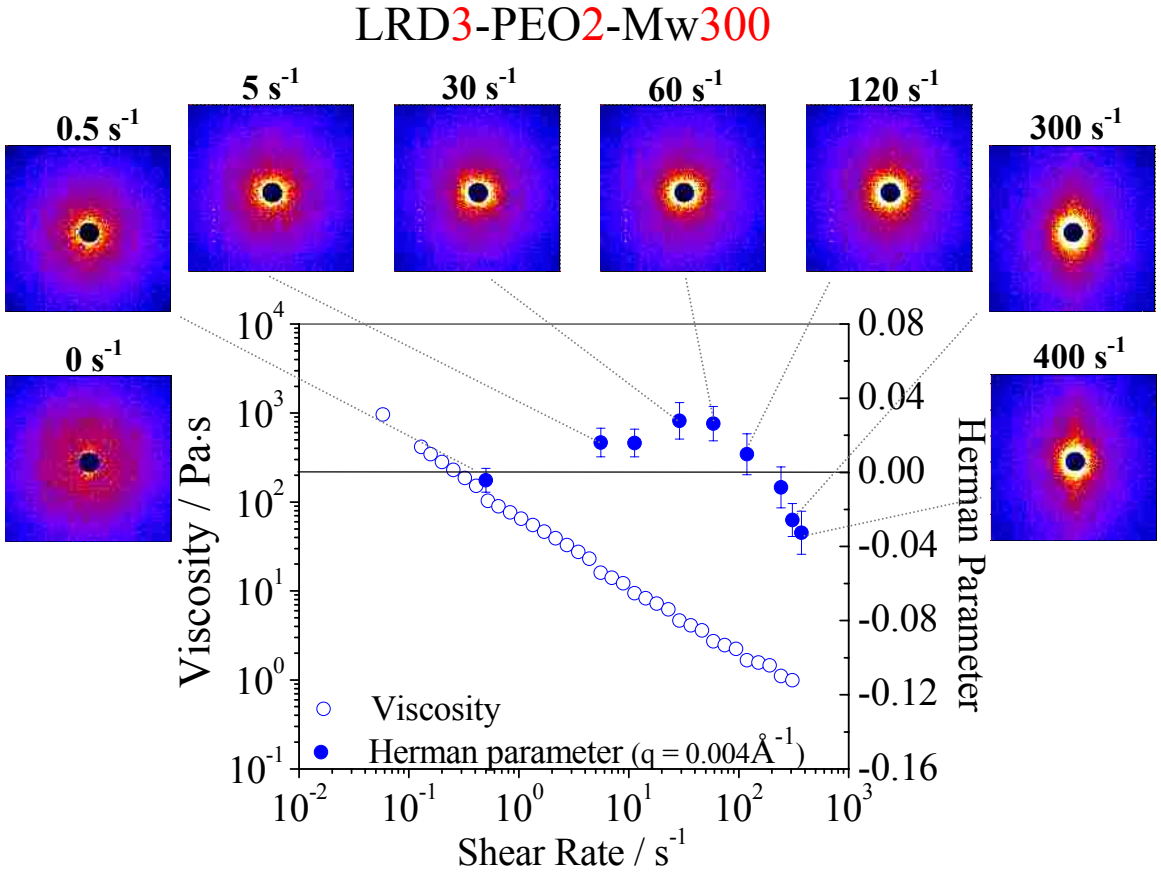

Figure 6.4: Rheo-SANS data from the LRD3-PEO2-Mw300 hydrogel. Even though shear-thinning behavior is observed over the entire range of shear rates, the structural responses are different at low and high shear rates. At low shear rates, large-scale structures orient along the neutral direction and produce butterfly scattering patterns (positive Herman parameter). With increasing shear rates, the nanoscopic components are forced to align along the flow direction and produce anisotropic scattering patterns (negative Herman parameter).

From the data presented here, it is clear that the quiescent structures that exist in these polymer-clay hydrogels depend only on the identity of the components. However, their response to flow, which is driven by the poly(ethylene oxide)-Laponite interactions is strongly influenced by the ability of the polymer to bridge two or more clay platelets. Something else that must affect the interactions within these systems and could be the direction for future studies is the adsorption energy of PEO segments onto Laponite. This could presumably be altered by changing the surface chemistry of Laponite, the pH, or the ionic strength of the samples. Furthermore, additional studies with a different type of clay (like Montmorillonite) or a different type of polymer (like poly(N-isopropylacrylamide)) could also contribute to a better understanding of the interactions within this class of systems and how they can be manipulated to optimize the material's performance for a desired application.

REFERENCES

1. Hussain, F.; Hojjati, M.; Okamoto, M.; Gorga, R. E., Review article: Polymer-matrix nanocomposites, processing, manufacturing, and application: An overview. *Journal of Composite Materials* **2006,** 40, (17), 1511-1575.

2. Krishnamoorti, R.; Vaia, R. A., *Polymer Nanocomposites – Synthesis, Characterization and Modeling*. ACS: Washington DC, 2001; Vol. 804.

3. Chapman, R.; Mulvaney, P., Electro-optical shifts in silver nanoparticle films. *Chemical Physics Letters* **2001,** 349, (5-6), 358-362.

4. Ma, D. L.; Hugener, T. A.; Siegel, R. W.; Christerson, A.; Martensson, E.; Onneby, C.; Schadler, L. S., Influence of nanoparticle surface modification on the electrical behaviour of polyethylene nanocomposites. *Nanotechnology* **2005,** 16, (6), 724-731.

5. Wilson, O.; Wilson, G. J.; Mulvaney, P., Laser writing in polarized silver nanorod films. *Advanced Materials* **2002,** 14, (13-14), 1000.

6. Yoon, P. J.; Fornes, T. D.; Paul, D. R., Thermal expansion behavior of nylon 6 nanocomposites. *Polymer* **2002,** 43, (25), 6727-6741.

7. Cooper, C. A.; Ravich, D.; Lips, D.; Mayer, J.; Wagner, H. D., Distribution and alignment of carbon nanotubes and nanofibrils in a polymer matrix. *Composites Science and Technology* **2002,** 62, (7-8), 1105-1112.

8. Bower, C.; Rosen, R.; Jin, L.; Han, J.; Zhou, O., Deformation of carbon nanotubes in nanotube-polymer composites. *Applied Physics Letters* **1999,** 74, (22), 3317-3319.

9. Safadi, B.; Andrews, R.; Grulke, E. A., Multiwalled carbon nanotube polymer composites: Synthesis and characterization of thin films. *Journal of Applied Polymer Science* **2002,** 84, (14), 2660-2669.

10. Zeng, J. J.; Saltysiak, B.; Johnson, W. S.; Schiraldi, D. A.; Kumar, S., Processing and properties of poly(methyl methacrylate)/carbon nano fiber composites. *Composites Part B-Engineering* **2004,** 35, (2), 173-178.

11. Gorga, R. E.; Cohen, R. E., Toughness enhancements in poly(methyl methacrylate) by addition of oriented multiwall carbon nanotubes. *Journal of Polymer Science Part B-Polymer Physics* **2004,** 42, (14), 2690-2702.

12. Jin, Z.; Pramoda, K. P.; Xu, G.; Goh, S. H., Dynamic mechanical behavior of melt-processed multi-walled carbon nanotube/poly(methyl methacrylate) composites. *Chemical Physics Letters* **2001,** 337, (1-3), 43-47.

13. Li, H. J.; Guan, L. H.; Shi, Z. J.; Gu, Z. N., Direct synthesis of high purity single-walled carbon nanotube fibers by arc discharge. *Journal of Physical Chemistry B* **2004,** 108, (15), 4573-4575.

14. Siochi, E. J.; Working, D. C.; Park, C.; Lillehei, P. T.; Rouse, J. H.; Topping, C. C.; Bhattacharyya, A. R.; Kumar, S., Melt processing of SWCNT-polyimide nanocomposite fibers. *Composites Part B-Engineering* **2004,** 35, (5), 439-446.

15. Lu, Y. F.; Yang, Y.; Sellinger, A.; Lu, M. C.; Huang, J. M.; Fan, H. Y.; Haddad, R.; Lopez, G.; Burns, A. R.; Sasaki, D. Y.; Shelnutt, J.; Brinker, C. J., Self-assembly of mesoscopically ordered chromatic polydiacetylene/silica nanocomposites. *Nature* **2001,** 410, (6831), 913-917.

16. Chen, J.; Hamon, M. A.; Hu, H.; Chen, Y. S.; Rao, A. M.; Eklund, P. C.; Haddon, R. C., Solution properties of single-walled carbon nanotubes. *Science* **1998,** 282, (5386), 95-98.

17. Mitchell, C. A.; Bahr, J. L.; Arepalli, S.; Tour, J. M.; Krishnamoorti, R., Dispersion of functionalized carbon nanotubes in polystyrene. *Macromolecules* **2002,** 35, (23), 8825-8830.

18. Qian, D.; Dickey, E. C.; Andrews, R.; Rantell, T., Load transfer and deformation mechanisms in carbon nanotube-polystyrene composites. *Applied Physics Letters* **2000,** 76, (20), 2868-2870.

19. Bhattacharyya, A. R.; Sreekumar, T. V.; Liu, T.; Kumar, S.; Ericson, L. M.; Hauge, R. H.; Smalley, R. E., Crystallization and orientation studies in polypropylene/single wall carbon nanotube composite. *Polymer* **2003,** 44, (8), 2373-2377.

20. Gong, X. Y.; Liu, J.; Baskaran, S.; Voise, R. D.; Young, J. S., Surfactant-assisted processing of carbon nanotube/polymer composites. *Chemistry of Materials* **2000,** 12, (4), 1049-1052.

21. Kimura, T.; Ago, H.; Tobita, M.; Ohshima, S.; Kyotani, M.; Yumura, M., Polymer composites of carbon nanotubes aligned by a magnetic field. *Advanced Materials* **2002,** 14, (19), 1380-1383.

22. Fan, Z. H.; Advani, S. G., Characterization of orientation state of carbon nanotubes in shear flow. *Polymer* **2005,** 46, (14), 5232-5240.

23. Ou, Y. C.; Yang, F.; Yu, Z. Z., New conception on the toughness of nylon 6/silica nanocomposite prepared via in situ polymerization. *Journal of Polymer Science Part B-Polymer Physics* **1998,** 36, (5), 789-795.

24. Zhang, M.; Singh, R. P., Mechanical reinforcement of unsaturated polyester by Al2O3 nanoparticles. *Materials Letters* **2004,** 58, (3-4), 408-412.

25. Ohno, K.; Koh, K.; Tsujii, Y.; Fukuda, T., Synthesis of gold nanoparticles coated with well-defined, high density polymer brushes by surface-initiated living radical polymerization. *Macromolecules* **2002,** 35, 8989-8993.

26. Yong, V.; Hahn, H. T., Processing and properties of SiC/vinyl ester nanocomposites. *Nanotechnology* **2004,** 15, (9), 1338-1343.

27. Pan, Y. X.; Yu, Z. Z.; Ou, Y. C.; Hu, G. H., A new process of fabricating electrically conducting nylon 6/graphite nanocomposites via intercalation polymerization. *Journal of Polymer Science Part B-Polymer Physics* **2000,** 38, (12), 1626-1633.

28. Chen, G. H.; Wu, D. J.; Weng, W. G.; Yan, W. L., Preparation of polymer/graphite conducting nanocomposite by intercalation polymerization. *Journal of Applied Polymer Science* **2001,** 82, (10), 2506-2513.

29. Ray, S. S.; Okamoto, M., Polymer/layered silicate nanocomposites: a review from preparation to processing. *Progress in Polymer Science* **2003,** 28, (11), 1539-1641.

30. Giannelis, E. P., Polymer-Layered Silicate Nanocomposites: Synthesis, Properties and Applications. *Applied Organometallic Chemistry* **1998,** 12, 675-680.

31. Giannelis, E. P.; Krishnamoorti, R.; Manias, E., Polymer-silicate nanocomposites: Model systems for confined polymers and polymer brushes. *Polymers in Confined Environments* **1999,** 138, 107-147.

32. Kojima, Y.; Usuki, A.; Kawasumi, M.; Okada, A.; Fukushima, Y.; Kurauchi, T.; Kamigaito, O., Mechanical-Properties of Nylon 6-Clay Hybrid. *Journal of Materials Research* **1993,** 8, (5), 1185-1189.

33. Ray, S. S.; Yamada, K.; Okamoto, M.; Ueda, K., Polylactide-layered silicate nanocomposite: A novel biodegradable material. *Nano Letters* **2002,** 2, (10), 1093-1096.

34. Yano, K.; Usuki, A.; Okada, A., Synthesis and properties of polyimide-clay hybrid films. *Journal of Polymer Science Part a-Polymer Chemistry* **1997,** 35, (11), 2289-2294.

35. Nanocomposites – Properties and Applications, 2005, www.azom.com/details.asp?ArticleID=921.

36. Kojima, Y.; Usuki, A.; Kawasumi, M.; Okada, A.; Kurauchi, T.; Kamigaito, O., One-Pot Synthesis of Nylon-6 Clay Hybrid. *Journal of Polymer Science Part A-Polymer Chemistry* **1993,** 31, (7), 1755-1758.

37. Usuki, A.; Kawasumi, M.; Kojima, Y.; Okada, A.; Kurauchi, T.; Kamigaito, O., Swelling Behavior of Montmorillonite Cation Exchanged for Omega-Amino Acids by Epsilon-Caprolactam. *Journal of Materials Research* **1993,** 8, (5), 1174-1178.

38. Gilman, J. W., Flammability and thermal stability studies of polymer layered-silicate (clay) nanocomposites. *Applied Clay Science* **1999,** 15, (1-2), 31-49.

39. Gilman, J. W.; Jackson, C. L.; Morgan, A. B.; Harris, R.; Manias, E.; Giannelis, E. P.; Wuthenow, M.; Hilton, D.; Phillips, S. H., Flammability properties of polymer - Layered-silicate nanocomposites. Polypropylene and polystyrene nanocomposites. *Chemistry of Materials* **2000,** 12, (7), 1866-1873.

40. Merkel, T. C.; Freeman, B. D.; Spontak, R. J.; He, Z.; Pinnau, I.; Meakin, P.; Hill, A. J., Ultrapermeable, reverse-selective nanocomposite membranes. *Science* **2002,** 296, (5567), 519-522.

41. Lal, J.; Auvray, L., Interaction of polymer with clays. *Journal of Applied Crystallography* **2000,** 33, (1), 673-676.

42. Lal, J.; Auvray, L., Interaction of polymer with discotic clay particles. *Molecular Crystals and Liquid Crystals* **2001,** 356, 503-515.

43. Schmidt, G.; Nakatani, A. I.; Butler, P. D.; Han, C. C., Small-angle neutron scattering from viscoelastic polymer-clay solutions. *Macromolecules* **2002,** 35, (12), 4725-4732.

44. Schmidt, G.; Nakatani, A. I.; Butler, P. D.; Karim, A.; Han, C. C., Shear orientation of viscoelastic polymer-clay solutions probed by flow birefringence and SANS. *Macromolecules* **2000,** 33, (20), 7219-7222.

45. Schmidt, G.; Nakatani, A. I.; Han, C. C., Rheology and flow-birefringence from viscoelastic polymer-clay solutions. *Rheologica Acta* **2002,** 41, (1-2), 45-54.

46. Nelson, A.; Cosgrove, T., A small-angle neutron scattering study of adsorbed poly(ethylene oxide) on laponite. *Langmuir* **2004,** 20, (6), 2298-2304.

47. Nelson, A.; Cosgrove, T., Dynamic light scattering studies of poly(ethylene oxide) adsorbed on laponite: Layer conformation and its effect on particle stability. *Langmuir* **2004,** 20, (24), 10382-10388.

48. Nelson, A.; Jack, K. S.; Cosgrove, T.; Kozak, D., NMR solvent relaxation in studies of multicomponent polymer adsorption. *Langmuir* **2002,** 18, (7), 2750-2755.

49. Swenson, J.; Smalley, M. V.; Hatharasinghe, H. L. M., Mechanism and strength of polymer bridging flocculation. *Physical Review Letters* **1998,** 81, (26), 5840-5843.

50. Swenson, J.; Smalley, M. V.; Hatharasinghe, H. L. M., Structure of bridging polymers. *Journal of Chemical Physics* **1999,** 110, (19), 9750-9756.

51. Swenson, J.; Smalley, M. V.; Hatharasinghe, H. L. M.; Fragneto, G., Interlayer structure of a clay polymer salt water system. *Langmuir* **2001,** 17, 3813-3818.

52. Swenson, J.; Smalley, M. V.; Thomas, R. K.; Crawford, R. J., Uniaxial stress and sol concentration dependence of the structure of a dressed macroion in a dilute electrolyte solution. *Journal of Physical Chemistry B* **1998,** 102, (30), 5823-5829.

53. Schmidt, G.; Malwitz, M. M., Properties of polymer-nanoparticle composites. *Current Opinion in Colloid & Interface Science* **2003,** 8, (1), 103-108.

54. Krishnamoorti, R.; Giannelis, E. P., Strain hardening in model polymer brushes under shear. *Langmuir* **2001,** 17, (5), 1448-1452.

55. Krishnamoorti, R.; Ren, J. X.; Silva, A. S., Shear response of layered silicate nanocomposites. *Journal of Chemical Physics* **2001,** 114, (11), 4968-4973.

56. Kojima, Y.; Usuki, A.; Kawasumi, M.; Okada, A.; Kurauchi, T.; Kamigaito, O.; Kaji, K., Novel Preferred Orientation in Injection-Molded Nylon 6-Clay Hybrid. *Journal of Polymer Science Part B-Polymer Physics* **1995,** 33, (7), 1039-1045.

57. Lele, A.; Mackley, M.; Galgali, G.; Ramesh, C., In-situ rheo-X-ray investigation of flow-induced orientation in layered silicate syndiotactic polypropylene nanocomposite melt. *Journal of Rheology* **2002,** 46, (5), 1091-1110.

58. Chen, G. M.; Qi, Z. N.; Shen, D. Y., Shear-induced ordered structure in polystyrene/clay nanocomposite. *Journal of Materials Research* **2000,** 15, (2), 351-356.

59. Malwitz, M. M.; Butler, P. D.; Porcar, L.; Angelette, D. P.; Schmidt, G., Orientation and relaxation of polymer-clay solutions studied by rheology and small-angle neutron scattering. *Journal of Polymer Science Part B-Polymer Physics* **2004,** 42, (17), 3102-3112.

60. Dundigalla, A.; Lin-Gibson, S.; Ferreiro, V.; Malwitz, M. M.; Schmidt, G., Unusual multilayered structures in poly(ethylene oxide)/laponite nanocomposite films. *Macromolecular Rapid Communications* **2005,** 26, (3), 143-149.

61. Malwitz, M. M.; Lin-Gibson, S.; Hobbie, E. K.; Butler, P. D.; Schmidt, G., Orientation of platelets in multilayered nanocomposite polymer films. *Journal of Polymer Science Part B-Polymer Physics* **2003,** 41, (24), 3237-3248.

62. Stefanescu, E. A.; Dundigalla, A.; Ferreiro, V.; Loizou, E.; Porcar, L.; Negulescu, I.; Garno, J.; Schmidt, G., Supramolecular structures in nanocomposite multilayered films. *Physical Chemistry Chemical Physics* **2006,** 8, (14), 1739-1746.

63. Malwitz, M. M.; Dundigalla, A.; Ferreiro, V.; Butler, P. D.; Henk, M. C.; Schmidt, G., Layered structures of shear-oriented and multilayered PEO/silicate nanocomposite films. *Physical Chemistry Chemical Physics* **2004,** 6, (11), 2977-2982.

64. Ramsay, J. D. F.; Lindner, P., Small-Angle Neutron-Scattering Investigations of the Structure of Thixotropic Dispersions of Smectite Clay Colloids. *Journal of the Chemical Society-Faraday Transactions* **1993,** 89, (23), 4207-4214.

65. Okamoto, M.; Nam, P. H.; Maiti, P.; Kotaka, T.; Hasegawa, N.; Usuki, A., A house of cards structure in polypropylene/clay nanocompocites under elongational flow. *Nano Letters* **2001,** 1, (6), 295-298.

66. Shibayama, M.; Karino, T.; Miyazaki, S.; Okabe, S.; Takehisa, T.; Haraguchi, K., Small-angle neutron scattering study on uniaxially stretched poly(N-isopropylacrylamide)-clay nanocomposite gels. *Macromolecules* **2005,** 38, (26), 10772-10781.

67. Miyazaki, S.; Karino, T.; Endo, H.; Haraguchi, K.; Shibayama, M., Clay concentration dependence of microstructure in deformed poly(N-isopropylacrylamide)-clay nanocomposite gels. *Macromolecules* **2006,** 39, (23), 8112-8120.

68. Brown, A. B. D.; Rennie, A. R., Images of shear-induced phase separation in a dispersion of hard nanoscale discs. *Chemical Engineering Science* **2001,** 56, (9), 2999-3004.

69. Medellin-Rodriguez, F. J.; Burger, C.; Hsiao, B. S.; Chu, B.; Vaia, R.; Phillips, S., Time-resolved shear behavior of end-tethered Nylon 6-clay nanocomposites followed by non-isothermal crystallization. *Polymer* **2001,** 42, (21), 9015-9023.

70. Lin-Gibson, S.; Kim, H.; Schmidt, G.; Han, C. C.; Hobbie, E. K., Shear-induced structure in polymer-clay nanocomposite solutions. *Journal of Colloid and Interface Science* **2004,** 274, (2), 515-525.

71. Lin-Gibson, S.; Schmidt, G.; Kim, H.; Han, C. C.; Hobbie, E. K., Shear-induced mesostructure in nanoplatelet-polymer networks. *Journal of Chemical Physics* **2003,** 119, (15), 8080-8083.

72. Haraguchi, K.; Takehisa, T., Nanocomposite hydrogels: A unique organic-inorganic network structure with extraordinary mechanical, optical, and swelling/de-swelling properties. *Advanced Materials* **2002,** 14, (16), 1120-1124.

73. Zebrowski, J.; Prasad, V.; Zhang, W.; Walker, L. M.; Weitz, D. A., Shake-gels: shear-induced gelation of laponite-PEO mixtures. *Colloids and Surfaces a-Physicochemical and Engineering Aspects* **2003,** 213, (2-3), 189-197.

74. Pozzo, D. C.; Walker, L. M., Reversible shear gelation of polymer-clay dispersions. *Colloids and Surfaces a-Physicochemical and Engineering Aspects* **2004,** 240, (1-3), 187-198.

75. http://www.Laponite.com.

76. Avery, R. G.; Ramsay, J. D. F., Colloidal Properties of Synthetic Hectorite Clay Dispersions .2. Light and Small-Angle Neutron-Scattering. *Journal of Colloid and Interface Science* **1986,** 109, (2), 448-454.

77. Mori, Y.; Togashi, K.; Nakamura, K., Colloidal properties of synthetic hectorite clay dispersion measured by dynamic light scattering and small angle X-ray scattering. *Advanced Powder Technology* **2001,** 12, (1), 45-59.

78. Mourchid, A.; Delville, A.; Lambard, J.; Lecolier, E.; Levitz, P., Phase-Diagram of Colloidal Dispersions of Anisotropic Charged-Particles - Equilibrium Properties, Structure, and Rheology of Laponite Suspensions. *Langmuir* **1995,** 11, (6), 1942-1950.

79. Herrera, N. N.; Letoffe, J. M.; Putaux, J. L.; David, L.; Bourgeat-Lami, E., Aqueous dispersions of silane-functionalized laponite clay platelets. A first step toward the elaboration of water-based polymer/clay nanocomposites. *Langmuir* **2004,** 20, (5), 1564-1571.

80. Kroon, M.; Vos, W. L.; Wegdam, G. H., Structure and formation of a gel of colloidal disks. *Physical Review E* **1998,** 57, (2), 1962-1970.

81. Gabriel, J. C. P.; Davidson, P., New trends in colloidal liquid crystals based on mineral moieties. *Advanced Materials* **2000,** 12, (1), 9-20.

82. Baghdadi, H. A.; Sardinha, H.; Bhatia, S. R., Rheology and gelation kinetics in laponite dispersions containing poly(ethylene oxide). *Journal of Polymer Science Part B-Polymer Physics* **2005,** 43, (2), 233-240.

83. Thompson, D. W.; Butterworth, J. T., The Nature of Laponite and Its Aqueous Dispersions. *Journal of Colloid and Interface Science* **1992,** 151, (1), 236-243.

84. Mourchid, A.; Lecolier, E.; Van Damme, H.; Levitz, P., On viscoelastic, birefringent, and swelling properties of Laponite clay suspensions: Revisited phase diagram. *Langmuir* **1998,** 14, (17), 4718-4723.

85. Gabriel, J. C. P.; Sanchez, C.; Davidson, P., Observation of nematic liquid-crystal textures in aqueous gels of smectite clays. *Journal of Physical Chemistry* **1996,** 100, (26), 11139-11143.

86. Ruzicka, B.; Zulian, L.; Ruocco, G., More on the phase diagram of laponite. *Langmuir* **2006,** 22, (3), 1106-1111.

87. Lemaire, B. J.; Panine, P.; Gabriel, J. C. P.; Davidson, P., The measurement by SAXS of the nematic order parameter of laponite gels. *Europhysics Letters* **2002,** 59, (1), 55-61.

88. Nicolai, T.; Cocard, S., Light scattering study of the dispersion of laponite. *Langmuir* **2000,** 16, (21), 8189-8193.

89. Rosta, L.; Vongunten, H. R., Light-Scattering Characterization of Laponite Sols. *Journal of Colloid and Interface Science* **1990,** 134, (2), 397-406.

90. Kroon, M.; Vos, W. L.; Wegdam, G. H., Structure and formation of a gel of colloidal disks. *International Journal of Thermophysics* **1998,** 19, (3), 887-894.

91. Kroon, M.; Wegdam, G. H.; Sprik, R., Dynamic light scattering studies on the sol-gel transition of a suspension of anisotropic colloidal particles. *Physical Review E* **1996,** 54, (6), 6541-6550.

92. Pignon, F.; Magnin, A.; Piau, J. M.; Cabane, B.; Lindner, P.; Diat, O., Yield stress thixotropic clay suspension: Investigation of structure by light, neutron, and x-ray scattering. *Physical Review E* **1997,** 56, (3), 3281-3289.

93. Pignon, F.; Piau, J. M.; Magnin, A., Structure and pertinent length scale of a discotic clay gel. *Physical Review Letters* **1996,** 76, (25), 4857-4860.

94. Bonn, D.; Kellay, H.; Tanaka, H.; Wegdam, G.; Meunier, J., Laponite: What is the difference between a gel and a glass? *Langmuir* **1999,** 15, (22), 7534-7536.

95. Bhatia, S.; Barker, J.; Mourchid, A., Scattering of disklike particle suspensions: Evidence for repulsive interactions and large length scale structure from static light scattering and ultra-small-angle neutron scattering. *Langmuir* **2003,** 19, (3), 532-535.

96. Levitz, P.; Lecolier, E.; Mourchid, A.; Delville, A.; Lyonnard, S., Liquid-solid transition of Laponite suspensions at very low ionic strength: Long-range electrostatic stabilisation of anisotropic colloids. *Europhysics Letters* **2000,** 49, (5), 672-677.

97. Bonn, D.; Tanaka, J.; Wegdam, G.; Kellay, H.; Meunier, J., Aging of a colloidal "Wigner" glass. *Europhysics Letters* **1999,** 45, (1), 52-57.

98. Dijkstra, M.; Hansen, J. P.; Madden, P. A., Statistical model for the structure and gelation of smectite clay suspensions. *Physical Review E* **1997,** 55, (3), 3044-3053.

99. Van Olphen, H., *An Introduction to Clay Colloid Chemistry*. 2 ed.; John Wiley and Sons: New York, 1977.

100. Saunders, J. M.; Goodwin, J. W.; Richardson, R. M.; Vincent, B., A small-angle X-ray scattering study of the structure of aqueous laponite dispersions. *Journal of Physical Chemistry B* **1999,** 103, (43), 9211-9218.

101. Tanaka, H.; Meunier, J.; Bonn, D., Nonergodic states of charged colloidal suspensions: Repulsive and attractive glasses and gels. *Physical Review E* **2004,** 69, 031404.

102. Bellour, M.; Knaebel, A.; Harden, J. L.; Lequeux, F.; Munch, J. P., Aging processes and scale dependence in soft glassy colloidal suspensions. *Physical Review E* **2003,** 67, (3).

103. Tanaka, H.; Jabbari-Farouji, S.; Meunier, J.; Bonn, D., Kinetics of ergodic-to-nonergodic transitions in charged colloidal suspensions: Aging and gelation. *Physical Review E* **2005,** 71, (2).

104. Bonn, D.; Tanase, S.; Abou, B.; Tanaka, H.; Meunier, J., Laponite: Aging and shear rejuvenation of a colloidal glass. *Physical Review Letters* **2002,** 89, (1).

105. Abou, B.; Bonn, D.; Meunier, J., Aging dynamics in a colloidal glass. *Physical Review E* **2001,** 6402, (2).

106. Knaebel, A.; Bellour, M.; Munch, J. P.; Viasnoff, V.; Lequeux, F.; Harden, J. L., Aging behavior of Laponite clay particle suspensions. *Europhysics Letters* **2000,** 52, (1), 73-79.

107. Hammouda, B.; Ho, D.; Kline, S., SANS from poly(ethylene oxide)/water systems. *Macromolecules* **2002,** 35, (22), 8578-8585.

108. Hammouda, B.; Ho, D. L.; Kline, S., Insight into clustering in poly(ethylene oxide) solutions. *Macromolecules* **2004,** 37, (18), 6932-6937.

109. Zhou, P.; Brown, W., Static and Dynamic Properties of Poly(Ethylene Oxide) in Methanol. *Macromolecules* **1990,** 23, (4), 1131-1139.

110. Dormidontova, E. E., Role of competitive PEO-water and water-water hydrogen bonding in aqueous solution PEO behavior. *Macromolecules* **2002,** 35, (3), 987-1001.

111. Dormidontova, E. E., Influence of end groups on phase behavior and properties of PEO in aqueous solutions. *Macromolecules* **2004,** 37, (20), 7747-7761.

112. Ho, D. L.; Hammouda, B.; Kline, S. R., Clustering of poly(ethylene oxide) in water revisited. *Journal of Polymer Science Part B-Polymer Physics* **2003,** 41, (1), 135-138.

113. Ho, D. L.; Hammouda, B.; Kline, S. R.; Chen, W. R., Unusual phase behavior in mixtures of poly(ethylene oxide) and ethyl alcohol. *Journal of Polymer Science Part B-Polymer Physics* **2006,** 44, (3), 557-564.

114. Devanand, K.; Selser, J. C., Polyethylene Oxide Does Not Necessarily Aggregate in Water. *Nature* **1990,** 343, (6260), 739-741.

115. Devanand, K.; Selser, J. C., Asymptotic Behavior and Long Range Interactions in Aqueous Solutions of Poly(ethylene oxide). *Macromolecules* **1991,** 24, 5943-5947.

116. Kjellander, R.; Florin, E., Water-Structure and Changes in Thermal-Stability of the System Poly(Ethylene Oxide)-Water. *Journal of the Chemical Society-Faraday Transactions I* **1981,** 77, 2053-&.

117. Lusse, S.; Arnold, K., The interaction of poly(ethylene glycol) with water studied by H-1 and H-2 NMR relaxation time measurements. *Macromolecules* **1996,** 29, (12), 4251-4257.

118. Bekiranov, S.; Bruinsma, R.; Pincus, P., Solution behavior of polyethylene oxide in water as a function of temperature and pressure. *Physical Review E* **1997,** 55, (1), 577-585.

119. Smith, G. D.; Bedrov, D.; Borodin, O., Molecular dynamics simulation study of hydrogen bonding in aqueous poly(ethylene oxide) solutions. *Physical Review Letters* **2000,** 85, (26), 5583-5586.

120. Karlstrom, G., A New Model for Upper and Lower Critical Solution Temperatures in Poly(Ethylene Oxide) Solutions. *Journal of Physical Chemistry* **1985,** 89, (23), 4962-4964.

121. Sun, T.; King, H. E., Discovery and modeling of upper critical solution behavior in the poly(ethylene oxide) water system at elevated pressure. *Macromolecules* **1998,** 31, (18), 6383-6386.

122. Bae, Y. C.; Lambert, S. M.; Soane, D. S.; Prausnitz, J. M., Cloud-Point Curves of Polymer-Solutions from Thermooptic Measurements. *Macromolecules* **1991,** 24, (15), 4403-4407.

123. Bae, Y. C.; Shim, J. J.; Soane, D. S.; Prausnitz, J. M., Representation of Vapor Liquid and Liquid Liquid Equilibria for Binary-Systems Containing Polymers - Applicability of an Extended Flory Huggins Equation. *Journal of Applied Polymer Science* **1993,** 47, (7), 1193-1206.

124. Branca, C.; Faraone, A.; Maisano, G.; Magazu, S.; Migliardo, P.; Triolo, A.; Triolo, R.; Villari, V., Can the isotopic H <-> D substitution affect the conformational properties of polymeric aqueous solutions? The poly(ethylene oxide)-water case. *Journal of Physics-Condensed Matter* **1999,** 11, (32), 6079-6098.

125. Matsuyama, A.; Tanaka, F., Theory of Solvation-Induced Reentrant Phase-Separation in Polymer-Solutions. *Physical Review Letters* **1990,** 65, (3), 341-344.

126. Saeki, S.; Kuwahara, N.; Nakata, M.; Kaneko, M., Upper and Lower Critical Solution Temperatures in Poly (Ethyleneglycol) Solutions. *Polymer* **1976,** 17, (8), 685-689.

127. Faraone, A.; Magazu, S.; Maisano, G.; Migliardo, P.; Tettamanti, E.; Villari, V., The puzzle of poly(ethylene oxide) aggregation in water: Experimental findings. *Journal of Chemical Physics* **1999,** 110, (3), 1801-1806.

128. Kinugasa, S.; Nakahara, H.; Fudagawa, N.; Koga, Y., Aggregative Behavior of Poly(Ethylene Oxide) in Water and Methanol. *Macromolecules* **1994,** 27, (23), 6889-6892.

129. Polverari, M.; vandeVen, T. G. M., Dilute aqueous poly(ethylene oxide) solutions: Clusters and single molecules in thermodynamic equilibrium. *Journal of Physical Chemistry* **1996,** 100, (32), 13687-13695.

130. Cowell, C.; Vincent, B., Flocculation Kinetics and Equilibria in Sterically Stabilized Dispersions. *Journal of Colloid and Interface Science* **1983,** 95, (2), 573-582.

131. Mathur, S.; Moudgil, B. M., Adsorption mechanism(s) of poly(ethylene oxide) on oxide surfaces. *Journal of Colloid and Interface Science* **1997,** 196, (1), 92-98.

132. Bjelopavlic, M.; Singh, P. K.; El-Shall, H.; Moudgil, B. M., Role of surface molecular architecture and energetics of hydrogen bonding sites in adsorption of polymers and surfactants. *Journal of Colloid and Interface Science* **2000,** 226, (1), 159-165.

133. Aray, Y.; Marquez, M.; Rodriguez, J.; Coll, S.; Simon-Manso, Y.; Gonzalez, C.; Weitz, D. A., Electrostatics for exploring the nature of water adsorption on the laponite sheets' surface. *Journal of Physical Chemistry B* **2003,** 107, (34), 8946-8952.

134. Nelson, A. R. J. Neutron and Light Scattering Studies of Polymer Adsorbed on Laponite. University of Pristol, Bristol, 2002.

135. Can, V.; Okay, O., Shake gels based on Laponite-PEO mixtures: effect of polymer molecular weight. *Designed Monomers and Polymers* **2005,** 8, (5), 453-462.

136. Daga, V. K.; Wagner, N. J., Linear viscoelastic master curves of neat and laponite-filled poly(ethylene oxide)-water solutions. *Rheologica Acta* **2006,** 45, (6), 813-824.

137. Macosko, C. W., *Rheology : Principles, Measurements, and Applications*. 1 ed.; John Wiley & Sons: 1994; p 109-133.

138. *ARES instrument manual*. Rheometric Scientific: September 2001; p 69-74.

139. Larson, R. G., *The Structure and Rheology of Complex Fluids*. Oxford University Press: New York, Oxford, 1999.

140. Fried, J. R., Polymer Science and Technology. In Prentice Hall PTR, Englewood Cliffs: New Jersey, 1995.

141. Glinka, C., What can be measured by SANS and Reflectometry? In *NIST summer school on SANS and Reflectometry from submicron structures*, Gaithersburg, Maryland, 2002.

142. Wignall, G. D.; Melnichenko, Y. B., Recent applications of small-angle neutron scattering in strongly interacting soft condensed matter. *Reports on Progress in Physics* **2005,** 68, (8), 1761-1810.

143. Kline, S., Fundamentals of Small-Angle Neutron Scattering. In *NCNR Summer School*, Maryland, 2000.

144. Roe, R. J., *Methods of X-Ray and Neutron Scattering in Polymer Science*. Oxford University Press: New York, 2000.

145. Zipfel, J. "Shear Induced structures in lamellar surfactant mesophases with different membrane properties". Albert-Ludwings-Universitat, Freiburg - Germany, 2000.

146. Pynn, R., Neutron Scattering - A PRIMER. In Los Alamos Neutron Science Center (LANSCE), 1990.

147. Higgins, J. S.; Benoit, H. C., *Polymers and Neutron Scattering*. Clarendon Press: Oxford, 1996.

148. Chen, S. H., Small-Angle Neutron-Scattering Studies of the Structure and Interaction in Micellar and Microemulsion Systems. *Annual Review of Physical Chemistry* **1986,** 37, 351-399.

149. Straty, G. C.; Hanley, H. J. M.; Glinka, C. J., Shearing Apparatus for Neutron-Scattering Studies on Fluids - Preliminary-Results for Colloidal Suspensions. *Journal of Statistical Physics* **1991,** 62, (5-6), 1015-1023.

150. Drews, A. R.; Barker, J. G.; Glinka, C. J.; Agamalian, M., Development of a thermal-neutron double-crystal diffractometer for USANS at NIST. *Physica B* **1997,** 241, 189-191.

151. Barker, J. G.; Glinka, C. J.; Moyer, J. J.; Kim, M. H.; Drews, A. R.; Agamalian, M., Design and performance of a thermal-neutron double-crystal diffractometer for USANS at NIST. *Journal of Applied Crystallography* **2005,** 38, 1004-1011.

152. http://www.ati.ac.at/~neutropt/experiments/USANS/usans.html.

153. Bhatia, S. R., Ultra-small-angle scattering studies of complex fluids. *Current Opinion in Colloid & Interface Science* **2005,** 9, (6), 404-411.

154. Chescoe, D.; Goodhew, P. J., *The Operation of Transmission and Scanning Electron Microscopes*. Royal Microscopy Society Handbooks, Oxford University Press: Oxford, UK, 1990.

155. Kalab, M. Microscopy in Food Science, 2004, http://anka.livstek.lth.se:2080/microscopy/foodmicr.htm.

156. Doi, M., *Introduction to Polymer Physics*. Clarendon Press: Oxford, 1996.

157. Doi, M.; Edwards, S. F., *The Theory of Polymer Dynamics*. Clarendon Press: Oxford, 1986.

158. Russo, P., *Polymer Dimensions*. Macromolecular Systems Class Notes: Baton Rouge, LA, Fall 2004.

159. Flory, P. J., *Principles of Polymer Chemistry* Cornell University Press: Ithaca, 1953

160. de Gennes, G. P., *Scaling Concepts in Polymer Physics*. Cornell University Press: Ithaca, NY, 1979.

161. Russo, P., *Dynamic Light Scattering of Dilute Polymer Solutions*. Macromolecular Systems Class Notes: Baton Rouge, LA, Spring 2004.

162. Russo, P., *Polymer Dimensions*. Macromolecular Systems Class Notes: Baton Rouge, LA, Fall 2003.

163. Glinka, C. J.; Barker, J. G.; Hammouda, B.; Krueger, S.; Moyer, J. J.; Orts, W. J., The 30 m small-angle neutron scattering instruments at the National Institute of Standards and Technology. *Journal of Applied Crystallography* **1998,** 31, 430-445.

164. Kline, S. R., Reduction and analysis of SANS and USANS data using IGOR Pro. *Journal of Applied Crystallography* **2006,** 39, 895-900.

165. Herrera, N.; Letoffe, J.; Putaux, J.; David, L.; Bourgeat-Lami, E., Aqueous dispersions of silane-functionalized laponite clay platelets. A first step toward the elaboration of water-based polymer/clay nanocomposites. *LANGMUIR* **2004,** 20, (5), 1564-1571.

166. Callaghan, I. C.; Ottewill, R. H., *Faraday Discussions* **1974,** 57, 110.

167. Pignon, F.; Magnin, A.; Piau, J. M., Butterfly light scattering pattern and rheology of a sheared thixotropic clay gel. *Physical Review Letters* **1997,** 79, (23), 4689-4692.

168. Schulz, H.; Wissen, M.; Bogdanski, N.; Scheer, H. C.; Mattes, K.; Friedrich, C., Impact of molecular weight of polymers and shear rate effects for nanoimprint lithography. *Microelectronic Engineering* **2006,** 83, (2), 259-280.

169. Mason, T. G.; Bibette, J.; Weitz, D. A., Elasticity of Compressed Emulsions. *Physical Review Letters* **1995,** 75, (10), 2051-2054.

170. Somani, R. H.; Yang, L.; Hsiao, B. S.; Sun, T.; Pogodina, N. V.; Lustiger, A., Shear-induced molecular orientation and crystallization in isotactic

polypropylene: Effects of the deformation rate and strain. *Macromolecules* **2005,** 38, (4), 1244-1255.

171. Ramzi, A.; Zielinski, F.; Bastide, J.; Boue, F., Butterfly Patterns - Small-Angle Neutron-Scattering from Deuterated Mobile Chains in a Randomly Cross-Linked Polystyrene Network. *Macromolecules* **1995,** 28, (10), 3570-3587.

172. Hayes, C.; Bokobza, L.; Boue, F.; Mendes, E.; Monnerie, L., Relaxation dynamics in bimodal polystyrene melts: A Fourier-transform infrared dichroism and small-angle neutron scattering study. *Macromolecules* **1996,** 29, (14), 5036-5041.

173. Mendes, E.; Oeser, R.; Hayes, C.; Boue, F.; Bastide, J., Small-angle neutron scattering study of swollen elongated gels: Butterfly patterns. *Macromolecules* **1996,** 29, (17), 5574-5584.

174. Bastide, J.; Leibler, L., Large-Scale Heterogeneities in Randomly Cross-Linked Networks. *Macromolecules* **1988,** 21, (8), 2647-2649.

175. Wheeler, E. K.; Izu, P.; Fuller, G. G., Structure and rheology of wormlike micelles. *Rheologica Acta* **1996,** 35, (2), 139-149.

176. Kadoma, I. A.; vanEgmond, J. W., "Tuliplike" scattering patterns in wormlike micelles under shear flow. *Physical Review Letters* **1996,** 76, (23), 4432-4435.

177. Belzung, B.; Lequeux, F.; Vermant, J.; Mewis, J., Flow-induced anisotropy in mixtures of associative polymers and latex particles. *Journal of Colloid and Interface Science* **2000,** 224, (1), 179-187.

178. Degroot, J. V.; Macosko, C. W.; Kume, T.; Hashimoto, T., Flow-Induced Anisotropic Sals in Silica-Filled Pdms Liquids. *Journal of Colloid and Interface Science* **1994,** 166, (2), 404-413.

179. Bastide, J.; Leibler, L.; Prost, J., Scattering by Deformed Swollen Gels - Butterfly Isointensity Patterns. *Macromolecules* **1990,** 23, (6), 1821-1825.

180. Vermant, J., Large-scale structures in sheared colloidal dispersions. *Current Opinion in Colloid & Interface Science* **2001,** 6, (5-6), 489-495.

181. Nicolai, T.; Cocard, S., Structure of gels and aggregates of disk-like colloids. *European Physical Journal E* **2001,** 5, (2), 221-227.

APPENDIX: COPYRIGHT PERMISSIONS

American Chemical Society's Policy on Theses and Dissertations

If your university requires a signed copy of this letter see contact information below.

Thank you for your request for permission to include **your** paper(s) or portions of text from **your** paper(s) in your thesis. Permission is now automatically granted; please pay special attention to the implications paragraph below. The Copyright Subcommittee of the Joint Board/Council Committees on Publications approved the following:

Copyright permission for published and submitted material from theses and dissertations
ACS extends blanket permission to students to include in their theses and dissertations their own articles, or portions thereof, that have been published in ACS journals or submitted to ACS journals for publication, provided that the ACS copyright credit line is noted on the appropriate page(s).

Publishing implications of electronic publication of theses and dissertation material
Students and their mentors should be aware that posting of theses and dissertation material on the Web prior to submission of material from that thesis or dissertation to an ACS journal may affect publication in that journal. Whether Web posting is considered prior publication may be evaluated on a case-by-case basis by the journal's editor. If an ACS journal editor considers Web posting to be "prior publication", the paper will not be accepted for publication in that journal. If you intend to submit your unpublished paper to ACS for publication, check with the appropriate editor prior to posting your manuscript electronically.

If your paper has **not** yet been published by ACS, we have no objection to your including the text or portions of the text in your thesis/dissertation in **print and microfilm formats**; please note, however, that electronic distribution or Web posting of the unpublished paper as part of your thesis in electronic formats might jeopardize publication of your paper by ACS. Please print the following credit line on the first page of your article: "Reproduced (or 'Reproduced in part') with permission from [JOURNAL NAME], in press (or 'submitted for publication'). Unpublished work copyright [CURRENT YEAR] American Chemical Society." Include appropriate information.

If your paper has already been published by ACS and you want to include the text or portions of the text in your thesis/dissertation in **print or microfilm formats**, please print the ACS copyright credit line on the first page of your article: "Reproduced (or 'Reproduced in part') with permission from [FULL REFERENCE CITATION.] Copyright [YEAR] American Chemical Society." Include appropriate information.

Submission to a Dissertation Distributor: If you plan to submit your thesis to UMI or to another dissertation distributor, you should not include the unpublished ACS paper in

your thesis if the thesis will be disseminated electronically, until ACS has published your paper. After publication of the paper by ACS, you may release the entire thesis (**not the individual ACS article by itself**) for electronic dissemination through the distributor; ACS's copyright credit line should be printed on the first page of the ACS paper.

Use on an Intranet: The inclusion of your ACS unpublished or published manuscript is permitted in your thesis in print and microfilm formats. If ACS has published your paper you may include the manuscript in your thesis on an intranet that is not publicly available. Your ACS article cannot be posted electronically on a publicly available medium (i.e. one that is not password protected), such as but not limited to, electronic archives, Internet, library server, etc. The only material from your paper that can be posted on a public electronic medium is the article abstract, figures, and tables, and you may link to the article's DOI or post the article's author-directed URL link provided by ACS. This paragraph does not pertain to the dissertation distributor paragraph above.

Questions? Call +1 202/872-4368/4367. Send e-mail to copyright@acs.org or fax to +1 202-776-8112. 10/10/03, 01/15/04, 06/07/06

12 January 2007 Our ref: CT/ND/Jan07/j008

Elena Loizou
Louisiana State University
Department of Chemistry
232 Choppin Hall
Baton Rouge 70802
USA

Dear Ms Loizou,

CURRENT OPINION IN COLLOID & INTERFACE SCIENCE, Vol 8, Issue 1,

2003, pp103-108, Schmidt et al, "Properties of polymer-nanoparticle……"

As per your letter dated 10 January 2007, we hereby grant you permission to reprint the aforementioned material at no charge **in your dissertation** subject to the following conditions:

1. If any part of the material to be used (for example, figures) has appeared in our publication with credit or acknowledgement to another source, permission must also be sought from that source. If such permission is not obtained then that material may not be included in your publication/copies.

2. Suitable acknowledgment to the source must be made, either as a footnote or in a reference list at the end of your publication, as follows:

   "Reprinted from Publication title, Vol number, Author(s), Title of article, Pages No., Copyright (Year), with permission from Elsevier".

3. Your thesis may be submitted to your institution in either print or electronic form.

4. Reproduction of this material is confined to the purpose for which permission is hereby given.

5. This permission is granted for non-exclusive world **English** rights only. For other languages please reapply separately for each one required. Permission excludes use in an electronic form other than submission. Should you have a specific electronic project in mind please reapply for permission.

6. This includes permission for UMI to supply single copies, on demand, of the complete dissertation. Should your dissertation be published commercially, please reapply for permission.

Yours sincerely

Clare Truter
Rights Manager, S&T

Your future requests will be handled more quickly if you complete the online form at www.elsevier.com/permissions

VITA

Elena Loizou is from Nicosia, Cyprus. After she graduated from a public high school, she enrolled at the University of Cyprus. During the last year of her undergraduate studies, she did her thesis work with the help and guidance of Dr. Costas Patrickios. Her thesis title was "Cationic Double-Hydrophilic Model Networks: Synthesis, Characterization, and Protein Adsorption Studies". In 2002, she obtained a Bachelor of Science from the Chemistry Department of the University of Cyprus, graduating with the highest GPA in the 4th year of studies. A few months later, she moved to the United States to pursue a Doctor of Philosophy in the Chemistry Department of the Louisiana State University. She joined Dr. Gudrun Schmidt's research group in January 2003. Since her research involved a significant number of neutron scattering experiments, which she performed at the NIST Center for Neutron Research in Maryland, in September 2005 she moved to this facility to finish her doctoral program under the close guidance of Dr. Paul Butler and Dr. Lionel Porcar. Her dissertation focuses on understanding the dynamic responses of polymer-clay hydrogels using microscopic, rheological and scattering techniques.

The articles she published so far are listed below:

- E. Loizou, J.T. Weisser, A. Dundigalla, L. Porcar, G. Schmidt, J.J. Wilker. "Structural effects of cross-linking a biopolymer hydrogel derived from marine mussel adhesive protein," *Macromolecular Bioscience*, **2006**, *6*, 711-718, **(Cover Article)**
- E. Loizou, P.D. Butler, L. Porcar, G. Schmidt. "Dynamic Responses in Nanocomposite Hydrogels," *Macromolecules*, **2006**, *39* (4), 1614-1619

- E. A. Stefanescu, A. Dundigalla, V. Ferreiro, E. Loizou, L. Porcar, I. Negulescu, J. Garno, G. Schmidt. "Supramolecular Structures in Nanocomposite Multilayered Films," *Phys. Chem. Chem. Phys.*, **2006**, *8*, (14), 1739-1746, **(Cover Article)**

- E. Loizou, P.D. Butler, L. Porcar, Y. Talmon, E. Kesselman, A. Dundigalla, G. Schmidt. "Large-scale Structures Nanocomposite Hydrogels," *Macromolecules*, **2005**, *38* (6), 2047-2049

- E. Loizou, P.D. Butler, M. Malwitz, G. Schmidt. "Dynamic Responses in Polymer-Clay Gels" *Mater. Res. Soc. Symp. Proc*., 840, Warrendale, PA , **2005**, Q2.7

- E. Loizou, A. I. Triftaridou, T. K. Georgiou, M. Vamvakaki, C. S. Patrickios. "Cationic double-hydrophilic model networks: synthesis, characterization, modeling and protein adsorption studies," *Biomacromolecules*, **2003**, *4* (5), 1150-1160

During her years in graduate school, she gave the following scientific presentations:

- E. Loizou, P. D. Butler, L. Porcar, G. Schmidt. Dynamic Responses in Nanocomposite Hydrogels, *American Crystallographic Association Annual Meeting,* Honolulu, Hawaii, July 22-27, **2006 (Invited talk)**

- E. Loizou, P. D. Butler, L. Porcar, G. Schmidt. Dynamic Responses in Nanocomposite Hydrogels, *American Conference on Neutron Scattering,* St. Charles, Illinois, June 18-22, **2006**

- E. Loizou, M.M. Malwitz, P. D. Butler, L. Porcar, E. Kesselman, I. Talmon, G. Schmidt, Polymer-Clay Hydrogels Studied by Scattering and Microscopy, *ECIS 18th European Conference of Colloid and Interface Society*, Almeria, Spain, September 19-24, **2004**

- E. Loizou, M.M. Malwitz, P. D. Butler, L. Porcar, E. Kesselman, I. Talmon, G. Schmidt, Structure and Properties of Polymer-Clay Networks, *Polymer Networks Conference*, NIH-Bethesda, MD, August 22-26, **2004**

- E. Loizou, M.M. Malwitz, P.D. Butler, L. Porcar, S. Lin-Gibson, G. Schmidt, Orientation and Relaxation of Polymer-Clay Solutions, *American Conference on Neutron Scattering*, College Park, MD, June 6-10, **2004**

- E. Loizou, M.M. Malwitz, P.D. Butler, M. Randazzo, G. Schmidt, A Rheological and Shear SANS Study of Laponite and Montmorillonite in Polymer Solutions, *7th International Symposium on Polymers for Advanced Technologies (PAT),* Fort Lauderdale*, Sept* **2003**